To the Graduate Council:

I am submitting herewith a thesis written by Lawrence S. Hood entitled "Quiescent and Oriented Crystallization Behavior of Linear Low Density Polyethylenes." I have examined the final copy of this thesis for form and content and recommend that it be accepted in partial fulfillment of the requirements for the degree of Master of Science, with a major in Polymer Engineering.

Joseph E. Spruiell,
Major Professor

We have read this thesis
and recommend its acceptance:

Accepted for the Council:

Vice Provost and
Dean of The Graduate School

QUIESCENT AND ORIENTED CRYSTALLIZATION BEHAVIOR OF LINEAR LOW DENSITY POLYETHYLENES

A Thesis

Presented for the

Master of Science

Degree

The University of Tennessee, Knoxville

Lawrence S. Hood

May 1990

ACKNOWLEDGEMENTS

I would like to express sincere appreciation to my advisor, Professor J.E. Spruiell, for his guidance, support, and patient encouragement throughout this work.

Appreciation is also extended to Professors D.C. Bogue and R.A. Benson for their interest in this research and for serving on the author's committee.

I am indebted to Dow Chemical Company for funding this project and supplying the resins and resin characteristics.

The aid and insight provided by the other faculty members and students is greatly appreciated. Special thanks are extended to Messrs. R. Patel and J. Zhou for their friendship and help these past two years. The skill and timely response of the electronics and machine shops is also greatly appreciated.

Finally, I would like to thank my Savior Jesus Christ and my family for the help and support that they have given me.

ABSTRACT

A series of isothermal and non-isothermal crystallization experiments were performed on nine linear low density polyethylenes and one high density polyethylene. In addition, melt spinning experiments were performed on three linear low density polyethylenes in order to gain a better understanding of their spinline behavior and the effect of stress on their crystallization behavior.

Isothermal experiments showed that crystallization rates were dependent on branching of the polymer molecules. Resins with extensive branching had crystallization rates which were much lower than linear polyethylene. This behavior was also observed in non-isothermal crystallization experiments.

Half time analysis was performed on the isothermal data to obtain coefficients which were used to model non-isothermal crystallization kinetics. Predicted behavior was in reasonably good agreement with experimental results at lower levels of crystallinity when crystallization isotherms were superposable. Non-linear regression was also used to obtain crystallization coefficients.

On-line diameter, temperature, birefringence, and tension data were collected for three LLDPE's at different spinning conditions. These resins had similar melt indices but quite different spinline behavior. The spinline data was analyzed using

the Continuous Cooling Transformation approach. These resins exhibited crystallization rates which were higher than could be obtained from cooling effects alone. A comparison of stress-enhanced crystallization rates as influenced by branching was inconclusive due to the presence of both a changing cooling rate and stress. Modeling of the spinline was somewhat successful in that general behavior could be predicted; however, high accuracy could not be obtained due to uncertainties in certain parameters.

TABLE OF CONTENTS

CHAPTER PAGE

CHAPTER PAGE

LIST OF FIGURES

FIGURE PAGE

FIGURE PAGE

FIGURE PAGE

FIGURE PAGE

FIGURE PAGE

FIGURE PAGE

FIGURE PAGE

LIST OF TABLES

CHAPTER 1

INTRODUCTION

The polyethylene (PE) family of resins constitute the largest volume of plastic sold in the United States. The uses of polyethylene are innumerable. The packaging industry is the chief user of polyethylene. Blow molding, injection molding, blown film, and cast film processes are used to produce polyethylene packaging structures. In fact, the blown film process consumes over 60% of the polyethylene produced [1].

Historically, two principal grades of polyethylene were available, low density polyethylene (LDPE) and high density polyethylene (HDPE). Each of these resins developed their own niches in the plastics industry due to their differing properties. HDPE resins have higher crystallinity, stiffness, tensile strength, hardness, abrasion resistance, chemical resistance and barrier properties than LDPE [2]. On the other hand, LDPE resins offer the advantage of higher levels of impact resistance, tear strength, clarity, permeability, and environmental stress-crack resistance. During the last ten years, a new class of polyethylenes has evolved into a major commodity in the U.S. market, linear low density polyethylene (LLDPE).

LLDPE is a comonomer of ethylene and an α-olefin. Linear

low density polyethylenes possess properties which are intermediate to or in some cases, superior to those of LDPE and HDPE. LLDPE resin can be processed at lower temperatures and higher rates than LDPE. Films made from LLDPE exhibit better puncture resistance, higher elongation, and improved tensile properties than those made from LDPE [2].

Common to the processes used to produce items from PE and other plastics is the presence of a stress field during solidification. The presence of stress has important effects on the mechanical properties of the final product. In fiber spinning and drawing processes, the presence of uniaxial stress causes elongation of polymer chains and increases in tensile strength. In the blown film process, the presence of tensile and hoop stresses results in a structure with good tear strength in both the longitudinal and circumferential directions.

An important goal in the blown film industry is the reduction of film thickness without loss of mechanical properties. This requires understanding of the effects of resin properties and processing conditions on the resulting structures obtained. The kinetics of crystallization is one of the most important factors which influences the development of structure. In particular, an understanding of the influence of stress on crystallization kinetics is necessary if accurate predictions of the structures and properties developed through processing are to be made.

The study of isothermal crystallization and the structures

which result has been an area of interest for many years and a considerable body of literature exists. However industrial processes typically involve non-isothermal crystallization under stress. Far less fundamental information exists about the structures which are produced under non-isothermal stress-enhanced crystallization. Here at the University of Tennessee-Knoxville, considerable effort has been expended in order to understand the structures which are developed under industrial processing conditions. In particular, the melt spinning and film blowing processes have been an active field of study over the past two decades [3-20]. One of the principal goals of these studies is to understand how processing variables and material characteristics influence the structure and mechanical properties of melt spun fibers and films. An understanding of the structures developed during melt processing requires knowledge about the molecular orientation in the melt, crystallization kinetics, and morphology of the crystalline regions.

During the last five years, efforts have concentrated on the use of a mathematical model for fiber melt spinning developed by Zieminski [15] which describes spinline dynamics including effects of structure development. This model requires various material constants which are dependent on the resin studied. The model predictions can be compared to experimental measurements of fiber diameter, temperature, birefringence and tension. The model may also be "inverted" and used with experimental data to obtain

non-isothermal elongational viscosity and heat transfer coefficients [4].

In the present research, a series of isothermal and non-isothermal crystallization experiments were conducted on nine LLDPE resins and one HDPE resin. In addition, melt spinning experiments were conducted on three LLDPE resins. The purpose of these experiments was fourfold:

1. to obtain comparative crystallization kinetics data for both isothermal and non-isothermal modes,

2. to establish whether non-isothermal crystallization kinetics can be predicted from isothermal crystallization data,

3. to compare spinline behavior of LLDPE resins having similar melt indices and molecular weights but varying degrees of branching, and

4. to use experimental spinline data to generate rheological and heat transfer information, and also for comparison to model predictions.

This research effort is part of a continuing series of projects involving the processing of polyolefins. The end result of these

projects will be a fundamental understanding of the effect of resin characteristics and processing variables on the structure and physical properties of polyolefins non-isothermally crystallized under stress. Although the present study relates directly to melt spinning of fibers, the knowledge and experimental experience accumulated should also eventually allow us to model complex processes such as blown film and blow molding.

CHAPTER 2

BACKGROUND AND LITERATURE REVIEW

2.1. Characteristics of Polyethylenes

Generally polyethylenes are divided into three classes, high density polyethylene HDPE, linear low density polyethylene LLDPE, and low density polyethylene LDPE. The differing properties of these materials are due to the length of chain branches and the distribution and frequency of branch points. HDPE (also called linear polyethylene) typically has less than five branches per thousand carbon atoms. LDPE has between eight and forty branches per thousand carbon atoms, where some of these branches will be long branches having branches themselves. Whereas HDPE and LDPE are homopolymers, LLDPE is a copolymer produced from ethylene and an α-olefin. LLDPE resins are characterized as having a large number of short chain branches.

LDPE is produced in high pressure processes. Polymerization occurs by a free radical mechanism at pressures exceeding 100 MPa and at temperatures which range from 170 to 200 °C. The amount of branching can be controlled by careful choice of operating conditions.

HDPE is produced at low pressures and moderate

temperatures using a catalyst. Two distinct catalytic processes are currently in use. The Phillips Petroleum process uses a chromium oxide-silica promoted catalyst in a suspension polymerization process. Typical operating conditions are 90 to 110 °C and 3 to 5 MPa [21]. The Ziegler process utilizes a titanium halide-aluminum alkyl catalyst. Currently three different polymerization processes are used with Ziegler catalysts [21].

Suspension polymerization is most commonly used for Ziegler HDPE. In this process, catalyst and ethylene are suspended in low molecular weight hydrocarbon diluents. The resulting slurry is agitated for better heat transfer in either a loop or stirred reaction vessel. Operating conditions for loop reactors are: pressure < 1 MPa and temperature between 80 and 90 °C. Stirred reactors operate at pressures around 3 MPa and temperatures between 65 and 110 °C. Residence time in both cases ranges from 1 to 4 hours.

In the solution polymerization process ethylene and any comonomers are dissolved in a solvent and fed into a reactor. Catalyst is added separately. Pressure is maintained between 2 and 4 MPa and temperature between 150 and 250 °C. Residence time may be as low as a few minutes. HDPE resins produced via the solution polymerization process typically have low molecular weight and a narrow molecular weight distribution.

The gas-phase polymerization process has the advantage of producing LLDPE or HDPE in the same reactor. This process takes place in a fluidized bed. The ethylene feed is also used for

fluidizing the bed and cooling the reaction mixture. Operating pressures range from 2 to 4 MPa and temperature from 70 to 110 °C. Polyethylenes having densities from 0.915 to 0.970 g/cm^3 may be produced. This process has an additional advantage in that no hydrocarbon diluents or solvents are used. However in the case of LLDPE copolymerization, both ethylene and an α-olefin are feed components. The addition of the α-olefin results in a polyethylene having short chain branches of a controlled length with essentially no long chain branching.

2.2 Kinetics of Crystallization

Crystallization is not an instantaneous process, and rate equations have been developed which attempt to describe the transformation from amorphous liquid to crystalline solid. These kinetic equations are based on a series of steps which are assumed to occur.

Random nucleation is the first step. All nuclei may form instantaneously when the melt reaches crystallization temperature (heterogeneous nucleation). In this case, the nucleation step has a zeorth order time dependence. Alternately, the nuclei may appear at a constant rate (homogeneous nucleation). In this case the nucleation step has a first order time dependence

$$n = Nt \qquad (2\text{-}1)$$

where n is the number of nuclei per volume, N is the nucleation rate constant, and t is time. Once the nuclei have formed, growth occurs in one, two, or three dimensions in the form of rods, disks, or spheres. The growth units resulting from the nuclei expand until the units impinge on one another. A growth unit's dimensions can be expressed in the following form:

$$r = Gt \qquad (2\text{-}2)$$

where r is the growth dimension, G is the growth rate and t is time. A proper rate equation must consider both nucleation and growth processes.

Nucleation and Growth

Crystallization of a substance involves both nucleation and growth processes. However the growth process can be considered as a secondary nucleation process occurring on the primary nucleation site. Consequently, the nucleation and growth rate equations have a similar form.

The basic concepts of nucleation theory were developed to model condensation from the vapor phase. This development is based on the change in free energy which results when transforming from one phase of another. For the case of

homogeneous nucleation, Frenkel [22] presented a theory of isothermal heterophase fluctuations which dealt with condensation from vapor, premelting and crystallization phenomena. For the case of solid nucleating from a liquid, Turnbull and Fisher [23] derived an expression for the steady state nucleation rate

$$N = N_o \exp\left[\frac{-E_D}{kT} + \frac{-\Delta G^*}{kT}\right] \qquad (2\text{-}3)$$

where N_o is a constant related to the geometry and interfacial energy of the critical nucleus. E_D is the activation energy of transport for a molecule across the crystal-liquid interface, and ΔG^* is the free energy required to form the critically sized nucleus. The two exponential terms have opposite temperature dependencies. This results in a maximum nucleation rate at a temperature between the equilibrium melting temperature T_m^o (where rate of formation of nuclei is zero) and the glass transition temperature T_g (where rate of molecular transport is zero) [24]. ΔG^* is generally expressed as [23,25-27]

$$\Delta G^* = \frac{m\sigma^2\sigma_e}{(\Delta G_v)^2} \qquad (2\text{-}4)$$

where m is a constant that depends on the critical nucleus geometry, σ and σ_e are the interfacial free energies of the side

surfaces and ends, $\Delta G_v = \Delta H \Delta T / T_m^o$ is the free energy difference per volume of crystal, ΔH is the heat of fusion, ΔT is $T_m^o - T$.

Cormia, Price and Turnbull [28] assumed that polymer systems would have a cylindrically shaped critical nucleus. For this geometry they obtained

$$\Delta G^* = \frac{8\pi\sigma^2\sigma_e}{(\Delta G_v)^2} \qquad (2\text{-}5)$$

Combination of equations (2-3) and (2-4) yields the following expression for the nucleation rate constant

$$N = N_o \exp\left[\frac{-E_D}{kT}\right] \exp\left[\frac{-8\pi\sigma^2\sigma_e}{kT(\Delta G_v)^2}\right] \qquad (2\text{-}6)$$

The heterogeneous nucleation process occurs at the interface of a second phase. The second phase may be impurities or nucleating agents. Price [26] and Turnbull [29] developed an expression for the heterogeneous nucleation rate constant by introducing interfacial free energies of the heterogeneity in contact with the melt and crystal. Their expression can be written as

$$N = C \exp\left[\frac{-E_D}{kT}\right] \exp\left[\frac{-16\sigma^2\sigma_c\Delta\sigma T_m^{o\,2}}{kT(\Delta H \Delta T)^2}\right] \qquad (2\text{-}7)$$

where C is a constant proportional to the critical cluster area, $\Delta\sigma = \sigma_{os} - \sigma_s$, σ_{os} and σ_s are the interfacial energies of the heterogeneity in contact with the crystal and the melt respectively.

According to Hoffman and Lauritzen's theory of polymer crystallization [25], polymer growth processes can be described as two-dimensional (secondary) nucleation. Hoffman and Lauritzen propose that the growth rate for a regular chain folding-smooth chain folded surface can be described as

$$G = G_o \exp\left[\frac{-E_D}{RT}\right] \exp\left[\frac{-4b_o\sigma^2\sigma_e\Delta\sigma T_m^o}{kT\Delta H\Delta T}\right] \qquad (2\text{-}8)$$

where b_o is the thickness of the chain molecules and R is the ideal gas constant. Hoffman and Weeks [30] have suggested that E_D is related to the segmental mobility of polymer chains, therefore the dependence of temperature on E_D can be expressed by the Williams-Landel-Ferry equation [31]:

$$E_D = \frac{C_1}{C_2 + T - T_g} \qquad (2\text{-}9)$$

where C_1 and C_2 are constants expected to be 17.4 KJ/mol and 51.6 K respectively. E_D may also be expressed in the following form [32]:

$$E_D = \frac{U^*}{T-T_\infty} \qquad (2\text{-}10)$$

where $U^* \approx 1500$ cal/mol and $T_\infty = T_g - 30$ K.

Regimes of Crystallization

Many investigators have observed changes in growth rates and morphology as a function of temperature for linear polyethylene. The growth rate has been observed to change by a factor of two when isothermal crystallization temperatures are within certain ranges [33]. Crystallization above and below this set of temperatures has been defined regime I and regime II.

In regime I crystallization, the lateral growth rate (g) is faster than the nucleation rate per unit area (i) [33,34]. The large relative differences in rates results in each growth layer being filled by a single nucleation step. Thus the growth rate perpendicular to the crystal face (G) will be proportional to (i). Regime I crystallization is favored at high crystallization temperatures. At these temperatures and for low molecular weights, crystallographically controlled growth can be approached, leading to rod or sheetlike habits [35]. Rod-like structures are reported in regime I.

In regime II crystallization, new growth steps nucleate before a layer is completely filled [33,34,36]. For this regime, the growth rate (G) is dependent on both (g) and (i). Spherulitic

morphology is found in regime II and is thought to be due to multiple nucleation steps inducing some form of non-crystallographic growth [37].

These growth regimes are not present in higher molecular weight polyethylenes ($M > 2\times10^5$). This is thought to be due to diffusion controlled growth as no organized supermolecular structures are found and only randomly oriented lamellae are observed [37].

Overall Transformation Analysis

Avrami [38-40] proposed an equation in 1939 which described the fractional crystallization of metals with time. Mandelkern [41] modified Avrami's theory to provide for incomplete crystallization, the resulting equation is used to describe polymer crystallization:

$$\frac{\Theta(t)}{\Theta(\infty)} = 1 - \exp(-kt^n) \qquad (2\text{-}11)$$

where $\Theta(t)$ is the crystallinity at time t, $\Theta(\infty)$ is the ultimate crystallinity, k is a rate constant containing both nucleation and growth mechanisms, and n is the Avrami index.

The Avrami index depends on the number of growth dimensions and the dominant type of primary nucleation process and is based on the following assumptions:

1. Nuclei are formed randomly throughout the melt and may appear either sporadically in time (homogeneously) or instantaneously (heterogeneously).

2. Growth occurs in a radial direction at a constant rate.

3. The density of the crystalline phase is constant.

The rate controlling step in an Avrami analysis can either be the rate of diffusion of molecules to the growth surface (diffusion control) or the rate of attachment of the molecules to the growth surface (interface control). Table 1 presents the value of the Avrami index for various types of nucleation and growth processes [42]. Typically, experimentally determined values of the Avrami index do not coincide exactly with those shown in Table 1 [43]. The Avrami index has also been observed to change during crystallization [44]. Generally the Avrami index decreases from an initial value of 3 or 4 during the latter stages of crystallization. This phenomenon is usually attributed to secondary crystallization.

Secondary crystallization is a general term which encompasses any phenomena which causes a slow increase in crystallinity which is nearly linear for a time on a log time plot. This phenomenon is usually attributed to crystallization occurring within the spherulitic boundaries after the spherulites have

Table 1. Avrami Indices

Avrami Index n	Nucleation	Growth Geometry	Growth Control
1/2	Instantaneous	Rod	Diffusion
1	Instantaneous	Rod	Interface
1	Instantaneous	Disc	Diffusion
3/2	Instantaneous	Sphere	Diffusion
3/2	Homogeneous	Rod	Diffusion
2	Instantaneous	Disc	Interface
2	Homogeneous	Disc	Diffusion
2	Homogeneous	Rod	Interface
5/2	Homogeneous	Sphere	Diffusion
3	Instantaneous	Sphere	Interface
3	Homogeneous	Disc	Interface
4	Homogeneous	Sphere	Interface

impinged on one another. Lamellar thickening would also be included in this definition. Secondary crystallization has a positive temperature coefficient and is thought to involve a slow diffusion mechanism [30].

Another limitation of the Avrami analysis is its assumption that the density of the transformed region is constant. It is likely that in spherulitic growth the degree of packing will be different from the central nucleus outwards [24]. Mandelkern [41] modified the Avrami equation to include a time dependent density function.

$$\frac{\Theta(t)}{\Theta(\infty)} = 1 - \exp(-kt^{n}At^{-m}) \qquad (2\text{-}12)$$

However when $m > 0$ it is not possible to separate n from m. This makes it difficult to extract detailed information on the growth and nucleation processes. The form of the rate constant k in equations (2-11) and (2-12) depends on the type of nucleation and growth processes that are active. For homogeneous nucleation with spherical growth, k is given by [24]:

$$k = \frac{\pi N G^{3} \rho_{c}}{3\rho_{a}} \qquad \text{and } n = 4 \qquad (2\text{-}13)$$

where N and G are the nucleation and growth rates, and ρ_c and ρ_a are the densities of the crystalline and amorphous phases. For heterogeneous nucleation with spherical growth k is given by [24]:

$$k = \frac{4\pi n_o G^3 \rho_c}{3\rho_a} \qquad \text{and } n = 3 \qquad (2\text{-}14)$$

where n_o is the fixed nucleation density.

If the rate of crystallization is assumed to have the same form as the growth rate then the overall crystallization rate may be written as [14]

$$k = k_o \exp\left[\frac{-E_D}{RT}\right] \exp\left[\frac{-C_3}{T\Delta T}\right] \qquad (2\text{-}15)$$

where

$$C_3 = \frac{\gamma b_o \sigma^2 \sigma_c \Delta\sigma T_m^o}{k\Delta H} \qquad (2\text{-}16)$$

and $\gamma = 4$ for regime I crystallization and $\gamma = 2$ for regime II crystallization.

The aforementioned problem of secondary crystallization has led some workers to use two Avrami equations. Banks et al. [45] applied two Avrami equations in parallel and series to describe consecutive and concurrent primary and secondary crystallization processes respectively. Hillier [46] proposed a modified Avrami equation consisting of two consecutive process, with the second process varying linearly with log time. Velisaris and Seferis [47] considered that bulk crystallization should involve two competing nucleation and growth processes. They proposed a linear combination of Avrami equations:

$$\frac{\Theta(t)}{\Theta(\infty)} = w_1\left[1-\exp(-k_1(T)t^{n1})\right] + w_2\left[1-\exp(-k_2(T)t^{n2})\right] \quad (2-17)$$

where for the ith process, k_i is the temperature dependent crystallization rate constant, n_i is the Avrami index and w_i is the weight fraction. The sum of the weight fractions $w_1 + w_2 = 1$. Price [48] suggested that an integral form of the Avrami equation would describe secondary crystallization in intra-spherulitic material.

Non-isothermal Crystallization Kinetics

Ozawa [49] derived an equation describing non-isothermal kinetics based on Evans [50] derivation of the Avrami equation. According to Ozawa, for a constant cooling rate, the degree of transformation will be given by

$$\frac{\Theta(T)}{\Theta(\infty)} = 1 - \exp\left[\frac{k(T)}{R^n}\right] \quad (2-18)$$

where $\Theta(T)$ is the crystallinity at temperature T, k(T) is a temperature dependent rate function, R is the cooling rate, and n is an integer whose value ranges from 1 to 4. Ozawa [49] showed that his approach was successful for PET. Eder and Wlochowicz [51] treated data from non-isothermal crystallization of isotactic polypropylene and high density polyethylene using the Ozawa approach. They showed that polypropylene was well represented

by Ozawa's equation whereas high density polyethylene was not. Eder and Wlochowicz [51] attributed this deviation to secondary crystallization and other factors not considered in Ozawa's theory.

Other workers have proposed various assumptions in an attempt to simplify the crystallization process. Nakamura et al. [52,53] proposed the "isokinetic" assumption. This assumption states that the time dependencies of the growth rates (G_i) and nucleation rate (N) are equal.

$$N(t) = aU(t) \qquad (2\text{-}19)$$

and

$$G_i(t) = b_iU(t) \qquad \text{for all } i$$

where U(t) is an arbitrary function of time and a and b_i are constants. These assumptions led to the following equation:

$$\frac{\Theta(T)}{\Theta(\infty)} = 1 - \exp\left[-\left(\int_0^t K(T)dt\right)^n\right] \qquad (2\text{-}20)$$

where n is the Avrami index based on isothermal experiments and K(T) is connected to the isothermal crystallization rate through the relation $K(T) = k(T)^{1/n}$.

Velisaris and Seferis [47] used an integral Avrami expression [54]:

$$\frac{\Theta(T)}{\Theta(\infty)} = 1 - \exp\left[- \int_0^t K(T) n t^{n-1} dt \right] \qquad (2\text{-}21)$$

to describe non-isothermal crystallization conditions. Velisaris and Seferis extend equation (2-21) to account for dual crystallization mechanisms

$$\frac{\Theta(T)}{\Theta(\infty)} = w_1 F_1 + w_2 F_2 \qquad (2\text{-}22)$$

where, for the ith process (i=1, 2) w_i is the weight fraction and

$$F_i = 1 - \exp\left[- \int_0^t k_i(T) n_i t^{(n_i - 1)} dt \right] \qquad (2\text{-}23)$$

The sum of the weight fractions $w_1 + w_2 = 1$. This dual mechanism approach was used to model the non-isothermal crystallization of PEEK matrices. Equations (2-20) or (2-21) can be used to model the non-isothermal crystallization behavior once the temperature dependence on the quiescent crystallization constant is known.

Prediction of Non-isothermal Crystallization Kinetics From Isothermal Data

For many polymers, quiescent isothermal crystallization behavior may be studied only over a narrow range of temperature and at low supercoolings. At larger supercoolings, the crystallization rates are too rapid to follow with presently available equipment. At high cooling rates typically found in polymer processing operations, crystallization occurs at lower temperature. The lack of available isothermal data at these low temperatures requires extrapolation of crystallization rates from low to high supercoolings.

Ziabicki [55] proposed an empirical equation relating the reciprocal of the experimentally observed crystallization half times K(T) to other experimental parameters:

$$K(T) = k_{max}\exp\left[\frac{-4\ln(2)(T-T_{max})^2}{D^2}\right] \qquad (2\text{-}24)$$

where k_{max} is the maximum in the rate-temperature curve, T_{max} is the temperature at which k_{max} occurs, and D is defined as the width at the half-height of the Gaussian distribution centered at K_{max}.

Cebe [56] formulated a crystallization rate equation based on growth theory. She assumed that the number of heterogeneous nuclei does not vary strongly with temperature and that all sites become active simultaneously:

$$k(T) = C_1 \exp\left[\frac{-C_2}{T-T_g+51.6}\right]\exp\left[\frac{-C_3}{T\Delta Tf}\right] \qquad (2\text{-}25)$$

where C_1 is a constant containing all prefactors, C_2 is a parameter associated with the temperature dependence of the viscosity, and C_3 is a parameter associated with the free energy of nucleation, and $f = 2T/(T_m^o+T)$ is a correction factor to compensate for the error in ΔH at large supercoolings [30].

The Hoffman-Lauritzen theory [57] describes linear spherulitic growth rate as a function of temperature. The Hoffman-Lauritzen theory can also be used to describe bulk crystallization kinetics [30,58]. In particular, the growth rate G can be shown to be proportional to $1/t_{1/2}$ (a measure of crystallization rate) if the following assumptions hold:

1. the nuclei form instantaneously and their number is relatively independent of temperature,

2. the density of the crystalline phase is constant, and

3. radial growth occurs at a constant rate

then the temperature variation of $1/t_{1/2}$ can be written as,

$$\frac{1}{t_{1/2}} = \left(\frac{1}{t_{1/2}}\right)_0 \exp\left[\frac{-U^*}{R(T-T_\infty)}\right]\exp\left[\frac{-C_3}{T\Delta T}\right] \qquad (2\text{-}26)$$

If the nucleation density is not independent of temperature, equation (2-26) represents a combination of both nucleation and growth rates. By plotting $\ln(1/t_{1/2}) + U^*/R(T-T_\infty)$ versus $-1/T\Delta T$ one can obtain C_3 and $(1/t_{1/2})_0$ [58,59]. Once $(1/t_{1/2})_0$ and C_3 are known, the Avrami rate constant k can be extrapolated to lower temperatures using

$$k = \frac{\ln(2)}{t^n} \qquad (2\text{-}27)$$

Important work by Hammami [60] has shown that the assumption of a fixed number of nuclei independent of temperature is not correct for polypropylene. Hammami measured the nucleation density of several pure polypropylenes using light microscopy and observed an exponential increase in the number of nuclei as the isothermal crystallization temperature decreased. By considering nucleation and growth rates separately, he was able to model the non-isothermal crystallization behavior of pure polypropylene using isothermally obtained data and the Nakamura et al. equation. His predictions were shown to be in fairly good agreement with experimental data.

2.3 Stress Induced Crystallization

The crystallization kinetics during melt spinning involve crystallization under stress and non-isothermal conditions. The majority of theoretical stress induced crystallization studies have involved cross-linked samples. In 1947 Flory [61] derived an equation for the equilibrium melting temperature of a cross-linked polymer network subjected to uniaxial elongation. Flory assumed that the network was stretched to a fixed elongation ratio α before any crystallization occurs. Additional assumptions were that chain segments between junctions obey Gaussian statistics, crystallization occurs under equilibrium conditions, and that the crystallites are perfectly oriented in the stretch direction. Flory's equation is

$$\frac{1}{T_m^o} - \frac{1}{T_m} = \frac{kN}{2\Delta H}\left[\left(\frac{2}{\pi}\right)^{\frac{1}{2}}\alpha - \left(\alpha^2 + \frac{2}{\alpha}\right)\right] \qquad (2\text{-}28)$$

where T_m^o is the equilibrium melting temperature of an unoriented system, m is the number of statistically independent segments between crosslinks, ΔH is the heat of fusion per statistical segment, and N is the number of network chains/cm^3.

A different equation relating the shift in the equilibrium melting temperature with uniaxial elongation ratio was proposed

by Krigbaum and Roe [62]. Their thermodynamic treatment considered that crystallization occurred after the network obtained a final level of strain. They assumed affine deformation, that Gaussian statistics applied, and that the free energy change associated with the orientation of the crystallites was negligible. Their equation is

$$\frac{1}{T_m^o} - \frac{1}{T_m} = \frac{kN}{2\Delta H}\left[\alpha^2 + \frac{2}{\alpha} - 3\right] \qquad (2\text{-}29)$$

The effect of stress on crystallization kinetics has been studied by Kobayashi and Nagasawa [63]. They assumed that the main effect of stress was on the free energy term ΔG_v due to the change in configurational entropy of Gaussian chains in the amorphous phase. Additional assumptions were that there existed similar nucleus geometries, mass transport terms and pre-exponential constants in both the stress induced and quiescent cases. They propose that the nucleation rate for the stress induced crystallization case be described by

$$N(\text{Stressed}) = N_o \exp\left[\frac{-\Delta F^*}{kT}\right] \exp\left[\frac{-m\sigma^2\sigma_e}{kT(\Delta G_v + \Delta G_{def})^2}\right] \qquad (2\text{-}30)$$

where ΔG_{def} is the elastically stored free energy resulting from the deformation of the polymer chains. Kobayashi and Nagasawa [63]

write that the ratio of the stressed to quiescent nucleation rates is

$$\frac{N(Stressed)}{N(Quiescent)} = \exp\left[\frac{m\sigma^2\sigma_e}{kT}\left(\frac{1}{\Delta G_{def}^2} - \frac{1}{\Delta G_v^2}\right)\right] \qquad (2\text{-}31)$$

The above equation provides a convenient way to compare stress enhancement on nucleation rates which does not require knowledge of N_o or ΔF^*. However, the value of ΔG_{def} must still be evaluated.

Kobayashi and Nagasawa [63] evaluated ΔG_{def} for a melt assuming the effect of stress on ΔH to be zero,

$$\Delta G_{def} = -T\Delta S_{def} \qquad (2\text{-}32)$$

where ΔS_{def} is the reduction in melt entropy due to orientation. The authors utilized equations from rubber elasticity theory to evaluate ΔS_{def} from the molecular extension ratio, α

$$\Delta S_{def} = \frac{-kN}{2}\left[\alpha^2 + \frac{2}{\alpha} - 3\right] \qquad (2\text{-}33)$$

where N is the number of network chains/cm^3. They assumed that affine deformation applies to a polymer melt, in which the molecular extension ratio α would equal the macroscopic stretch ratio λ. However Ziabicki [55] points out that this analysis leads to

an overprediction of the value of ΔS_{def} for a melt.

Ziabicki [55,64,65] considered the direct formation of heterogeneous (athermal) nuclei in oriented systems. Ziabicki assumed that as the melt became oriented, some of the chain segments would become well enough aligned to obtain thermodynamic stability. Once stability was reached, spontaneous growth would result. The athermal contribution to the nucleation rate was

$$-\left(\frac{\partial R}{\partial \lambda}\right)\left(\frac{d\lambda}{dt}\right)\iint_s J\, ds \qquad (2\text{-}34)$$

where R is a vector characteristic for a critically sized nucleus, λ is the deformation ratio, and J is the distribution function for cluster size and shape, and s is the critical boundary area which defines a stable cluster of segments. Ziabicki approximated the above equation as a power series and postulated that for moderate orientations, only the quadratic term would be significant, concluding that

$$k(f) = k(f=0)_{max}\exp\left[A(T)f^2\right] \qquad (2\text{-}35)$$

where k is the reciprocal half-time of crystallization, f is a parameter describing orientation, and A(T) is a temperature dependent empirical parameter. Ziabicki postulated that if nucleation and growth rates had the same form, then for spherical

nuclei A(T) could be approximated as

$$A(T) = \frac{C_1 + C_2\Delta T_o}{\Delta T_o^3} \qquad (2\text{-}36)$$

where C_1 and C_2 are constants which depend on growth geometry and thermodynamic quantities and ΔT_o is T_m^o-T for the unstressed case. If equation (2-35) is combined with equation (2-24) then

$$K(T) = k_{max}\exp\left[\frac{-4\ln(2)(T-T_{max})^2}{D^2} + A(T)f^2\right] \qquad (2\text{-}37)$$

which may be used to describe crystallization kinetics during melt spinning [4,8,14,15].

Katayama and Yoon [66] utilized the work of Hoffman and others [57,63] along with the theory of rubber elasticity to derive the following expression for the ratio of oriented (k_{A0}) to quiescent (k_A) crystallization rate

$$\frac{k_{A0}}{k_A} = \exp\left\{\frac{C_1}{T\Delta T}\left(1 - \frac{1}{1 + C_2(T/\Delta T)(\Delta n)^2}\right)\right\} \qquad (2\text{-}39)$$

where Δn is the birefringence. The effect of stress may also be incorporated into the crystallization kinetic equation based on the Hoffman-Lauritzen theory [14]

$$K(T,f_a) = K_o \exp\left[\frac{-U^*}{R(T-T_\infty)}\right] \exp\left[\frac{-C_3}{T\Delta T + CT^2 f_a^2}\right] \qquad (2\text{-}38)$$

where f_a is the amorphous orientation function.

Several workers have studied the non-isothermal and/or oriented behavior of polyethylene. Some of their results are reported below.

Mandelkern [67] studied the effect of M_η on the density of non-isothermally crystallized HDPE. He observed that for a given M_η, the density of the non-isothermally crystallized HDPE was lower than for the isothermally crystallized case. In both the isothermal and non-isothermal cases, the general trend was that as M_η increased the density would decrease until a plateau was reached. For the non-isothermal case this plateau occurred above $M_\eta = 10^5$ while for the isothermal case this plateau did not occur until $10^6 < M_\eta < 10^7$.

Kawai and Tonami [68] studied the isothermal crystallization behavior of cross-liked polyethylene under stress. They observed an Avrami index of one in the initial stages of crystallization. During the latter part of the crystallization process, the Avrami analysis was not applicable.

Katayama and Nakamura [69] studied melt spinning of linear polyethylene. They observed that as the distance from the spinneret increased, the birefringence would pass through a maximum, then a minimum, and then another maximum. On-line

wide angle x-ray patterns suggested that the first crystallites formed have their c-axis oriented nearly parallel to the fiber axis. As the distance from the spinneret increased, the preferred orientation of the c-axis tilted away from the fiber axis, eventually reaching an inclination of 40° to 60°. From these observations, Katayama and Nakamura suggested that the variations in observed birefringence resulted from the tilting of highly anisotropic crystals as distance from the spinneret (crystallinty) increased.

Dees and Spruiell [7] also studied melt spinning of linear polyethylene. They observed that as fiber velocity (stress) increased, crystallization rate increased but final crystallinity decreased. These results were consistent with those of Nakamura et al. [52,53]. Dees and Spruiell proposed a morphological model based on the observed changes in the unit cell orientation functions (f_a, f_b, and f_c) with increasing stress. Three morphological forms for polyethylene were proposed: spherulitic morphology at low stress, row-nucleated twisted lamellae at intermediate stress and row-nucleated untwisted lamellae at high stress. Based on the results of Dees and Spruiell [7] and others, Spruiell and White [12] proposed a Continuous Cooling Transformation (CCT) approach for comparing the crystallization kinetics of melt spun and quiescently crystallized polymer samples. This approach was used to explain why polyethylene crystallizes at a higher temperature than polypropylene on the melt spinline whereas for quiescent conditions, polypropylene

crystallizes at a higher temperature. Lambach [8] studied melt spinning of linear polyethylene and linear low density polyethylene. He observed that linear polyethylene had a significantly higher c-axis orientation than LLDPE at any stress. Lambach also found that for low melt index resins (4 and 10), c-axis orientation would increase as stress increased. However little change in c-axis orientation was observed in higher melt index resins (26 and 40) at the same spinning conditions.

2.4 Fiber Spinning

The three principle types of fiber spinning processes are melt spinning, wet spinning, and dry spinning. In melt spinning, molten polymer is extruded through a capillary die. The liquid threadline solidifies while it passes through a cooling medium. Nylon, polyester, and polyolefin fibers are melt spun. In wet spinning, the polymer is dissolved in a solvent. The solution is extruded through a spinneret and the resulting filaments are passed through a coagulating bath. The coagulating bath solidifies the filaments. Viscose fibers are produced by the wet spinning process. In dry spinning, a polymer is dissolved in a solvent and the solution is extruded through a spinneret. The filaments travel through an enclosed chamber in which a hot gas is blown through. The hot gas evaporates the solvent and the filaments solidify.

Acrylic and poly(vinyl chloride) filaments are produced by the dry spinning process. Of the three major methods for producing fibers, melt spinning, wet spinning, and dry spinning, the most economical is the melt spinning process. Because of the growing importance of melt spinning, the study of melt spinning dynamics has received much attention during the past 25 years.

Force Balance

The fiber spinning force balance can be written as

$$F_{rheo} = F_{ext} + F_{inert} + F_{drag} + F_{grav} + F_{surf} \qquad (2\text{-}40)$$

where F_{rheo} is the rheological force in the fiber, F_{ext} is the external take-up tension, F_{inert} is the inertial force as the fiber is accelerated, F_{drag} is the drag force caused by the fiber moving through the air, F_{grav} is the gravitational force on the fiber, F_{surf} is the surface tension force at the fiber-air interface.

The magnitudes of these forces vary with spinning conditions. F_{surf} results from the change of the curvature of the fiber surface and corresponding surface energy of the fiber [55]. F_{surf} is proportional to the surface tension at the fiber-cooling medium interface and is usually ignored. White [70] identified four melt spinning regimes which depend on drawdown force and fiber velocity:

Regime 1 - Gravitational spinning

$$F_{rheo} \approx F_{grav} \tag{2-41}$$

Regime 2 - Low drawdown

$$F_{rheo} \approx F_{grav} + F_{ext} \tag{2-42}$$

Regime 3 - Moderate drawdown

$$F_{rheo} \approx F_{ext} \tag{2-43}$$

Regime 4 - High drawdown and take-up velocity

$$F_{rheo} \approx F_{ext} + F_{drag} + F_{inert} \tag{2-44}$$

Zieminski [15] derived differential equations for the spinline forces by simplifying the fundamental equations of continuity and motion [77].

$$dF_{rheo} = \pi\left(\frac{D}{2}\right)^2 d\sigma \tag{2-45}$$

$$dF_{inert} = Wdv \tag{2-46}$$

$$\delta F_{drag} = (\rho C_D v^2 \pi D)dz \tag{2-47}$$

$$\delta F_{grav} = \left(\frac{Wg}{v}\right) dz \qquad (2\text{-}48)$$

where D, σ, v, and ρ are the fiber diameter, stress, velocity, and density, g is the gravitational acceleration constant, and z is the distance along the spinline. W is the mass flow rate which is related to the other variables by the continuity equation

$$W = \rho\pi\left(\frac{D}{2}\right)^2 v \qquad (2\text{-}49)$$

At high spinning speeds, the air drag force becomes increasingly important. Many investigators have studied the nature of the drag coefficient, C_D, in the drag force equation. The drag coefficient is typically written in terms of a Reynolds number, Re.

$$Re = \frac{\rho_a v D}{\eta_a} \qquad (2\text{-}50)$$

where ρ_a and η_a are the density and viscosity of air. Various investigators have measured C_D by measurements of tension in a stationary fiber in an airstream. Hamana et. al. [72] reported for C_D:

$$C_D = 0.68\ Re^{-0.61} \qquad (2\text{-}51)$$

Similar results have been reported by other investigators [73-75], with the pre-exponential constant varying from 0.27 to 1.30.

Energy Balance

An energy balance is necessary to determine the fiber temperature as a function of time or distance. The first general form of the energy balance was proposed by Kase and Matsuo [76]. Their equation considered both convective and radiative heat loss to the environment. This equation was modified by Nakamura et al. [52,53] to allow for heat generation due to crystallization.

Zieminski [15] developed an energy balance equation for fiber spinning based on the basic energy equation in cylindrical coordinates [71]. Zieminski made the following simplifying assumptions:

1. Negligible radial and circumferential fiber velocities

2. Negligible radiative heat loss to the environment

3. Negligible conductive heat loss to the environment

4. Zero viscous heat generation

5. No radial variation in temperature.

The assumption of negligible radiative heat loss was based on the work of Ziabicki and Kędzierska [77] and Wilhelm [78]. These workers showed that the radiation contribution to the total heat flux ranged from 20% near the die to 1% a short distance away. Zieminski wrote the heat balance as

$$\frac{dT}{dz} = \frac{\pi Dh(T-T_a)}{WC_p} + \left(\frac{\Delta H}{C_p}\right)\frac{d\Theta}{dz} \qquad (2\text{-}52)$$

where T is the fiber temperature, D is the fiber diameter, h is the heat transfer coefficient, T_a is ambient temperature, W is the mass flow rate, C_p is the resin heat capacity, ΔH is the heat of fusion, and Θ is the crystalline fraction.

Kase and Matsuo [76] found that the heat transfer coefficient could be described with the following equation

$$h = 6.85 \times 10^{-5}\left(\frac{\rho v^2}{W}\right)^{0.259}\left[1 + \left(\frac{8v_y}{v_f}\right)^{0.167}\right] \qquad (2\text{-}53)$$

where v_y is the cross-air velocity and v_f is the fiber velocity.

The heat of crystallization will also effect the energy balance. Zieminski [15] determined that crystallization on the spinline was best described by a modified Avrami equation, equation (2-11). By differentiating the Avrami equation by t and substituting

$$dt = \frac{dz}{v} \qquad (2\text{-}54)$$

Zieminski wrote

$$\frac{d\Theta}{dz} = \frac{\Theta_\infty nK}{v}\left(\int \frac{K}{v} dz\right)^{n-1} \exp\left[-\left(\int \frac{K}{v} dz\right)^{n}\right] \qquad (2\text{-}55)$$

where Ziabicki's empirical formulation of K, equation (2-37) was used.

Birefringence and Orientation

Shimizu et al. [79] treated the amorphous birefringence by coupling the stress optical law with a Maxwell element. The stress optical law is written as

$$\Delta n_a = C_{op}\sigma \qquad (2\text{-}56)$$

where Δn_a is the amorphous birefringence, C_{op} is the stress optical coefficient, and σ is the stress. By differentiation equation (2-56) by t

$$\frac{\partial \Delta n_a}{\partial t} = C_{op}\frac{d\sigma}{dt} \qquad (2\text{-}57)$$

and substituting a Maxwell element for $d\sigma/dt$

$$\frac{d\sigma}{dt} = E\frac{dv}{dz} - E\frac{\sigma}{\eta} \qquad (2\text{-}58)$$

equation (2-59) is the result

$$\frac{d\Delta n_a}{dt} = C_{op}E\frac{dv}{dz} - C_{op}E\frac{\sigma}{\eta} \qquad (2\text{-}59)$$

where E is Young's modulus and η is the elongational viscosity. If the substitutions $dt = dz/v$ and $\Delta n_a = C_{op}$ are made then

$$\frac{d\Delta n_a}{dz} = \frac{C_{op}E}{v}\frac{dv}{dz} - E\frac{\Delta n_a}{v\eta} \qquad (2\text{-}60)$$

The total birefringence can be written as

$$\Delta n = (1 - \Theta)\Delta n_a + \Theta f_c \Delta_c^o \qquad (2\text{-}61)$$

where Θ is the crystallinity, f_c is the c-axis orientation function, and Δ_c^o is the intrinsic crystalline birefringence [80]. The form birefringence Δn_f has been excluded from equation (2-61). The form birefringence is caused by the distortion of a light wave's electrical field when passing through the interface between phases having dissimilar refractive indices. Stein [81] found that for LDPE

the form birefringence constituted 5-10% of the total birefringence. The amorphous orientation function f_a is calculated from

$$f_a = \frac{\Delta n_a}{\Delta_a^o} \qquad (2\text{-}62)$$

where Δ_a^o is the intrinsic amorphous birefringence. Stein and Norris [82] use the Lorenz-Lorentz equation to determine a value of 0.0572 for Δ_c^o based on the specific polarizabilities of $C_{36}H_{74}$ crystals parallel and perpendicular to the c-axis. Stein and Norris [82] report a value of 0.0428 for Δ_a^o for polyethylene. Katayama et al. [51] assume a value of 1.5×10^{-10} for the stress optical coefficient while Ishizuka and Koyama [83] assume $C_{op} = 1.8 \times 10^{-10}$ cm^2/dyne based on their HDPE melt spinning experiments.

Melt Spinning Modeling

Initial melt spinning studies were made on isothermal systems. The absence of heat transfer simplified the data analysis. These initial workers concentrated on studying the rheology of the spinline. Acierno et al. [84] found that for LDPE, elongational viscosity increased as stretch rate increased. Chen et al. [85] observed that the stress levels for a polyethylene melt were underpredicted, when based on external values in their model.

Metzner and Sperot [86] reported a linear increase in spinline velocity with distance for LDPE.

Kase and Matsuo [76,87] made the first attempt at modeling the non-isothermal melt spinline. They assumed a Newtonian fluid and neglected the forces of air drag, gravity, and surface tension. They assumed a forced convective mechanism for heat transfer.

Hamana et al. [72] derived a model applicable to high speed melt spinning by included inertial, air drag, and gravity forces. Hamana et al. also assumed a Newtonian fluid. Denn and Gagon [88] used both a Newtonian and non-Newtonian function in their model of the PET melt spinning process. They were unable to discern any difference between the functions due to the extreme sensitivity of the heat transfer coefficient used.

Yasuda et al. [89] allowed for a radial temperature gradient in the model. Their calculations showed a radial ΔT ranging from 2 to 12 °C. They were also able to measure the difference of birefringence between the center and the surface of as-spun PET fibers. This ΔT and difference of birefringence increased as fiber velocity increased, but decreased as cooling air temperature increased.

Ishizuka and Koyama [83] studied the apparent elongational viscosity of HDPE on a melt spinline at low spinning speeds. For a broad molecular weight distribution HDPE, the elongational viscosity was observed to increase as temperature decreased until 160 °C. Below 160 °C the elongational viscosity decreased and

reached a minimum at 130 °C. Ishizuka and Koyama reported that for a narrow molecular weight distribution HDPE, the elongational viscosity would increase with cooling until 115 °C. Below 115 °C the elongational viscosity would rapidly increase due to the onset of crystallization.

Here at the University of Tennessee, Zieminski [15] studied melt spinning and developed an extensive mathematical model which describes the high speed melt spinning of polymers. Zieminski's model included air drag, inertial and gravity effects in the force balance. Crystallization kinetics were included in the force and heat balances. An empirical correlation based on molecular weight characteristics and differential values of the fiber temperature were used to describe the elongational viscosity. The drag coefficient used was the form derived from boundary layer theory by Sakiadis [90]. The heat transfer coefficient used was based on the work of Kase and Matsuo [76,87]. Zieminski used Shimizu et al.'s [79] theoretical treatment of birefringence and orientation. The kinetic rate constant included the effects of temperature and orientation [55]. Zieminski [15] combined the above concepts with the basic equations of continuity, energy, and motion to derive a system of eight ordinary differential equations. Those equations are listed below.

$$dF_{rheo} = dF_{inert} + \delta F_{drag} - \delta F_{grav} \qquad (2\text{-}63)$$

$$dF_{inert} = Wdv \tag{2-46}$$

$$\delta F_{drag} = (\rho_a C_D v^2 \pi D)dz \tag{2-47}$$

$$\delta F_{grav} = \left(\frac{Wg}{v}\right) dz \tag{2-48}$$

$$\frac{dT}{dz} = \frac{\pi Dh(T-T_a)}{WC_p} + \left(\frac{\Delta H}{C_p}\right)\frac{d\Theta}{dz} \tag{2-52}$$

$$dt = \frac{dz}{v} \tag{2-54}$$

$$\frac{d\Delta n_a}{dz} = \frac{C_{op}E}{v}\frac{dv}{dz} - \frac{E\Delta n_a}{v\eta} \tag{2-60}$$

$$\frac{dv}{dz} = \frac{\sigma}{\eta} \tag{2-64}$$

These equations were solved numerically using IBM's Continuous System Modeling Program (CSMP), available on the University of Tennessee's IBM 370 computer system. Zieminski used his model to predict the spinline behavior of nylon 6,6 and polypropylene at speeds up to 7000 m/min. These predictions were compared to actual on-line birefringence, diameter, temperature, and tension data. Fair agreement was observed between the model and experimental data for nylon 6,6 and polypropylene.

Bheda [4] was the next person at the University of Tennessee to study fiber spinning. Bheda studied high speed melt spinning of nylon 6, and made two important improvements to the fiber spinning research program. His first improvement was to develop an on-line non-contact method for diameter measurement which was a great improvement over the microscope technique used previously. His second improvement was to use an "inversion" procedure on the model to determine the proper values of the elongational viscosity and heat transfer coefficient. The inversion technique is similar to that used by George and Deeg [91]. In this technique, experimental diameter, temperature, and tension data are fed into a variant of the melt spinning model. An initial value of the rheological force at the spinneret is chosen and supplied to the inversion program. If this initial rheological force is correct, the experimental and predicted tension values will be the same and correct values of the elongational viscosity and heat transfer coefficient are obtained. If these values are not the same, a new value of the initial rheological force is chosen and the process is repeated. Bheda [4] successfully used this inversion technique to predict birefringence, diameter, and temperature profiles which were in good agreement with experimental data.

Lambach [8] was the next person to emerge from the fiber spinning program at the University of Tennessee. Lambach studied melt spinning of polyethylenes at speeds ranging from 500 to 4000 m/min. Lambach's polymer samples were a HDPE having

a melt index (MI) of 10 and three LLDPE's (ethylene-octene copolymers) having melt indices of 4, 26, and 40. Lambach reported several differences between the resins:

1. The LLDPE's exhibited c-axis orientation that was significantly less than that of HDPE at any stress.

2. C-axis orientation increased for the 4 and 10 MI resins as stress increased, however little change was reported for the 26 and 40 MI resins for the same condition.

3. The Continuous Cooling Transformation approach demonstrated that stress enhanced the crystallization of the 4 and 10 MI resins but had little effect on the 26 and 40 MI resins, at least in the range of conditions studied.

4. Modeling of the melt spinning behavior of the 26 and 40 MI resins was successful, however the model could not accurately predict the diameter profile and onset of crystallization for the 4 and 10 MI resins.

Jianguo Zhou [14] was the next person to study fiber spinning at the University of Tennessee. Zhou worked with three polypropylenes having melt indices of 12, 35 and 300 and the speeds ranging from 1000-5000 m/min. He observed that the 12

MI resin possessed a monoclinic crystal structure at all spinning speeds, whereas the 300 MI resin contained primarily the smectic phase. The 35 MI resin's structure would change from smectic to monoclinic as take-up velocity increased. Zhou attributed these changes in crystalline order to differences in crystallization kinetics caused by the molecular orientation and changes in temperature during processing. An important contribution by Zhou was the use of a crystallization rate equation based on isothermal growth theory. Using the melt spinning model and the Continuous Cooling Transformation approach, Zhou demonstrated that for the samples studied, crystallization kinetics are largely controlled by the molecular orientation developed in the melt in the temperature range where crystallization can occur. The crystallization kinetics and elongational viscosity were observed to be related to the molecular weight. As the molecular weight increased, elongational viscosity would increase. The resulting increase in orientation produced large increases in crystallization kinetics.

CHAPTER 3

EXPERIMENTAL MATERIALS AND PROCEDURES

3.1 Resin Identification and Characterization

Ten polyethylenes supplied by the Dow Chemical Company were used in this study. They included one HDPE and nine LLDPE resins. Eight of the LLDPE resins were ethylene-octene copolymers while the other was an ethylene-propene copolymer. Each resin was assigned a sample number by Dow and its characteristics were reported by the same. For convenience a University of Tennessee (UT) sample code was assigned to each resin. These codes, molecular weight, melt index, density, and polydispersity values for each resin are reported in Table 2. Dow also provided branching information in the form of Analytical Temperature Rising Elution Fractionation (ATREF) curves and the ratio of CH_3 groups to 1000 carbon atoms.

ATREF is a fractionation technique based on crystallinity. In this technique, the sample is dissolved in a solvent at an elevated temperature and injected into a pre-heated column. The column temperature is slowly decreased and the molecules precipitate onto a support. Fresh solvent is injected into the column as column

Table 2. Polyethylene Resin Identification and Properties

UT Code	Resin Type	Density (g/cm^3)	Melt Index	M_w	M_n	M_w/M_n
LL2	LLDPE	0.925	2.0	95800	14900	6.4
LL2.5	LLDPE	0.920	2.5	99400	18500	5.4
LL3.3	LLDPE	0.917	3.3	83500	12700	6.6
LL3.9	LLDPE	0.914	4.0	81200	14900	5.5
LL4	LLDPE	0.935	4.0	71500	16300	4.4
LLP†	LLDPE	0.951	4.0	80000	19200	4.2
LL4.3	LLDPE	0.941	4.3	79200	20100	3.9
LL26	LLDPE	0.940	26.5	43500	10900	4.0
LL40	LLDPE	0.935	40.0	36300	9840	3.7
HD10	HDPE	0.962	10.0	58500	14900	3.9

† LLP is an ethylene-propene copolymer while the other LLDPE resins are ethylene-octene copolymers.

temperature is raised. The relative amount of dissolved sample is then recorded as a function of column temperature.

The solubility characteristics of a polymer depends on its crystallinity which is chiefly controlled by the length, number and type of short chain branches. Molecules having a large number of short chain branches will dissolve at low temperatures whereas molecules with few short chain branches will dissolve only at higher temperatures. Thus an ATREF curve provides information as to the relative distribution of short chain branches in a sample.

Figure 1 shows ATREF curves for LL3.3 and LL26. The x-axis represents the dissolution (column) temperature. The y-axis represents the relative amount of sample which dissolved at this temperature. The LL3.3 resin displays a broad and complicated ATREF curve indicative of a broad and complex short chain branching distribution. The LL26 resin reveals a much sharper ATREF curve. Comparison of the y-axis reveals a large difference in scales between these resins. This provides evidence that LL26 has a narrow distribution of short chain branches. ATREF curves for all of the samples are found in Appendix A.

A convenient way to quantify the ATREF curves is by the average dissolution temperature, $\bar{x}$(ATREF). This information along with methyls/1000 carbon atoms is found in Table 3. Methyls/1000 C atoms and $\bar{x}$(ATREF) are plotted against density in Figures 2 and 3, Inspection of these figures reveals that density is strongly influenced by the degree of branching. This is to be

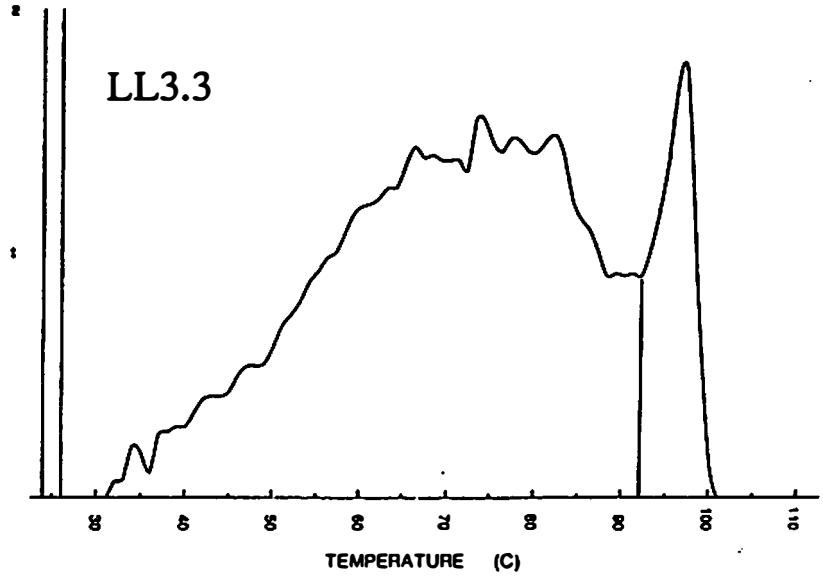

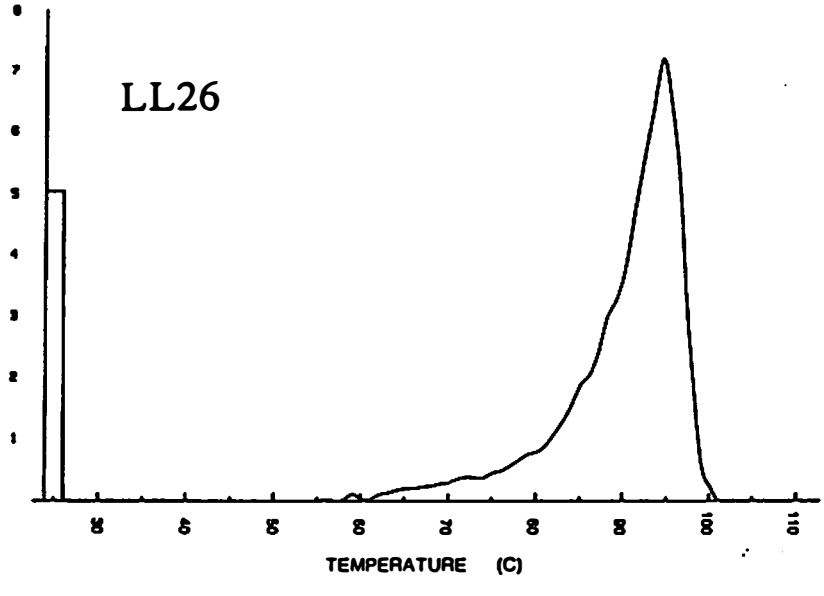

Figure 1 LL3.3 and LL26 ATREF curves.

Table 3. Polyethylene Branching Characteristics

UT Code	x(ATREF)	Methyls/ 1000 C
LL2	81.0	6.69
LL2.5	74.9	10.87
LL3.3	73.5	11.26
LL3.9	72.2	12.39
LL4	86.8	4.68
LLP	95.9	2.64
LL4.3	92.6	2.17
LL26	89.3	3.60
LL40	86.5	5.15
HD10	99.4	1.17

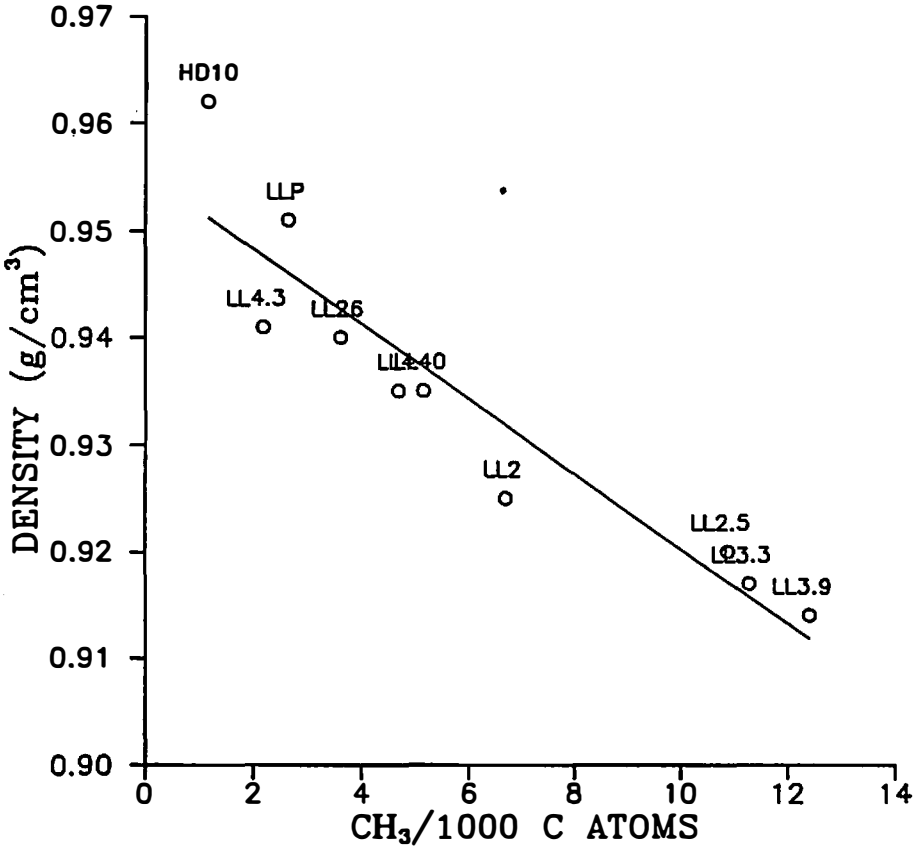

Figure 2 Density versus methyl groups per 1000 carbon atoms.

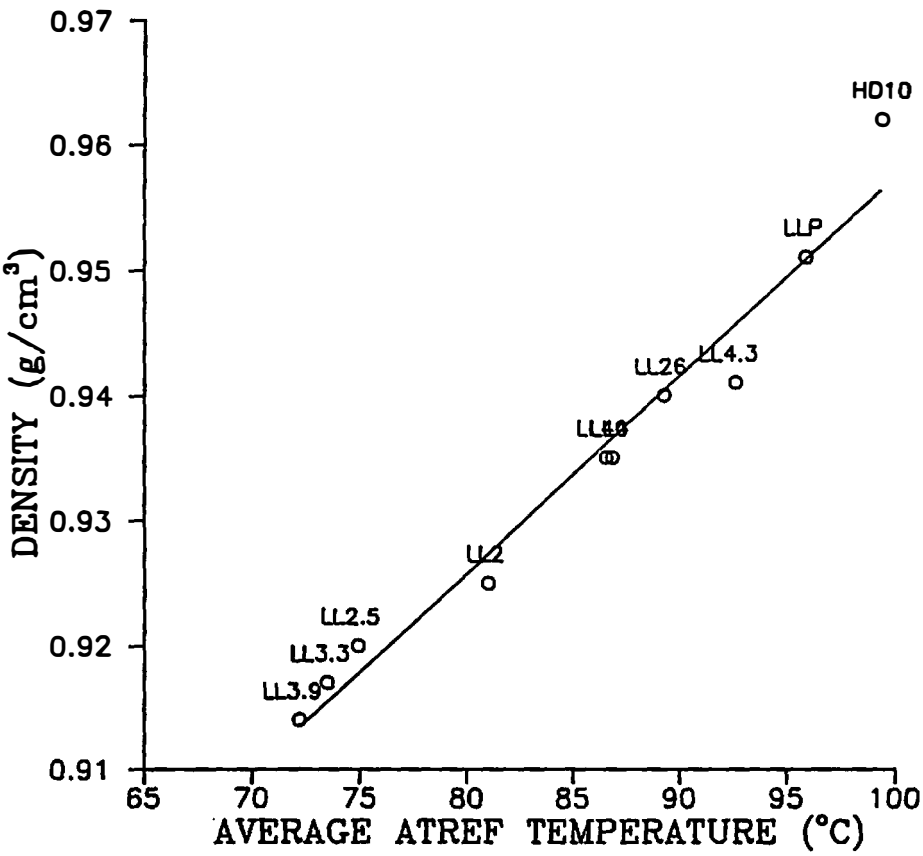

Figure 3. Density versus average ATREF temperature.

expected.

3.2 Experimental Procedures For Isothermal Crystallization

Depolarized Light Microscopy (DLM) was used to measure isothermal crystallization rates. Samples were prepared as films using a Wabash model 12-12-2TB 12-ton melt press. The resin pellets were placed between two clean pieces of Kapton™ polyimide film separated by a 50 μm aluminum spacer. This film-resin sandwich was placed between two stainless steel ferrotype platens and inserted between the press plates. The resin was allowed to melt at 160 °C and the press was closed.

Pressed films were placed between a glass slide and cover slip and melted in a Mettler FP82 hot stage controlled by a Mettler FP80 programmable controller. A window in the stage allows for the transmission of light through the sample. The films were melted at 160 °C for 15 minutes. This hot stage was placed on the microscope stage of an Olympus BH-2 optical microscope equipped with cross-polars. The light intensity was measured by an International Light IL700 Research Radiometer. The radiometer was calibrated such that the output was zero when the sample was completely molten. This output was sent to a Heath SR-205 strip chart recorder. The hot stage temperature was quickly lowered until the desired crystallization temperature was reached. At this

instant, the chart recorder was started. Crystallization was allowed to proceed until the intensity-time curve exhibited negligible slope. A straight edge was used to determine the point at which the slope had reached its constant value. This point was considered to represent the end of primary crystallization.

The chart paper was digitized by a Tektronix 4594 digitizing tablet. The data were then downloaded to an IBM-AT personal computer for analysis. The intensity-time data were treated to obtain relative crystallinity $\Theta(t)/\Theta(\infty)$ using equation (3-1).

$$\frac{\Theta(t)}{\Theta(\infty)} = \frac{I(t) - I(0)}{I(\infty) - I(0)} \qquad (3-1)$$

where I(t) is the intensity of light measured at any time t, I(0) is the initial intensity, and $I(\infty)$ is the final intensity.

3.3 Experimental Procedures For Non-isothermal Crystallization

Non-isothermal crystallization kinetics were measured by Differential Scanning Calorimetry (DSC). Sample pellets were cut and placed in aluminum sample pans. Sample weight ranged from 3 to 5 mg. The pans were placed into a Perkin-Elmer DSC7 attached to a refrigeration unit. The unit was turned on and allowed to come to equilibrium. Nitrogen purge gas flow rate was

set at 25 cc/min. The DSC7 was connected to a Perkin-Elmer 7500 Professional Computer through a TAS7 Instrument Controller.

Samples were heated to 160 °C for 5 minutes. The temperature was then decreased at a programmed rate. The resulting crystallization exotherms were plotted using an HP 7470A plotter attached to the computer. An example of a typical exotherm is shown in Figure 4.

These plots were digitized by a Tektronix 4594 digitizing tablet and downloaded to an IBM-AT personal computer for analysis. The data were represented by a cubic spline interpolating polynomial which was integrated stepwise using Simpson's Rule. A linear baseline between the start and end of crystallization was assumed. The relative crystallinity was given by

$$\frac{\Theta(T)}{\Theta(\infty)} = \frac{\int_0^t \left(\frac{dH}{dt}\right) dt}{\int_0^\infty \left(\frac{dH}{dt}\right) dt} \qquad (3\text{-}2)$$

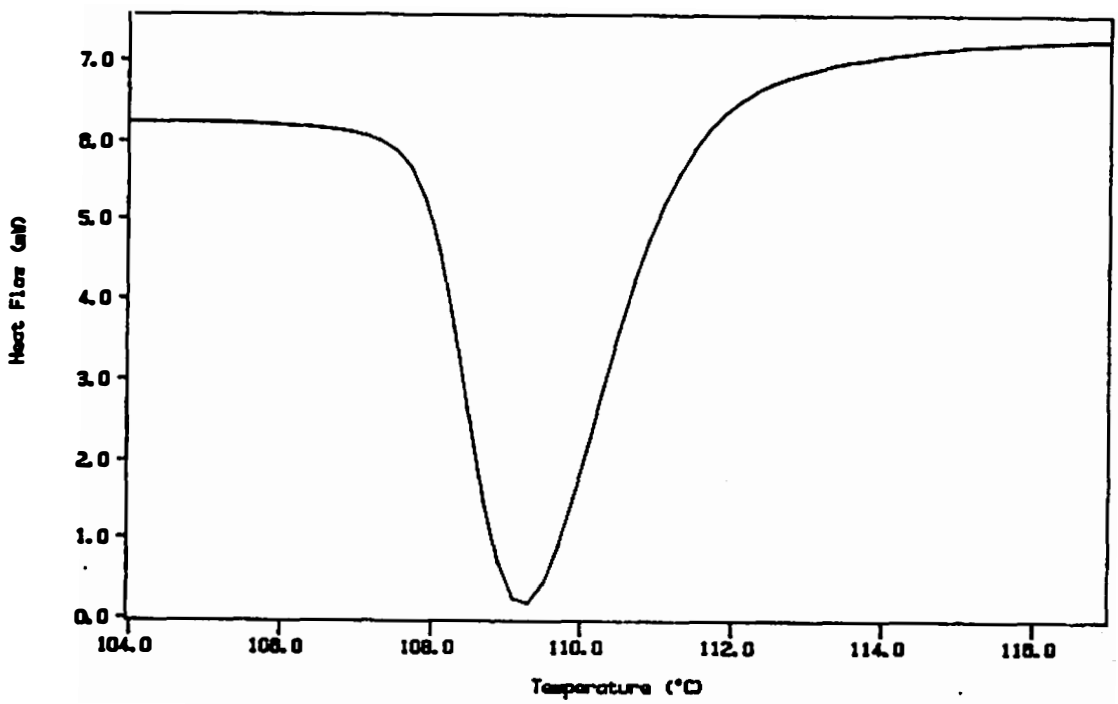

Figure 4. Sample DSC crystallization exotherm.

3.4. Melt Spinning Procedures

Description of Melt Spinning Apparatus

A Fourne extruder (shown schematically in Figure 5) manufactured by Fourne Associated, West Germany was used in all melt spinning experiments. The extruder has a 13 mm by 300 mm screw attached to a variable speed electric motor through a gear box. The screw speed may be varied from 18 to 120 rpm. The extruder is equipped with a 7 liter nitrogen purged hopper. The hopper feed throat is water cooled to avoid any back flow of melt. The extruder barrel is heated by two independently controlled band heaters. The resin passes through the extruder into the spinning assembly, consisting of the spinhead, a metering pump (Zenith type HPB-4647) and spinpack. The pump is a positive displacement type which provides for a constant volumetric flow rate. The pump speed is controlled by a variable speed motor. The spinpack consists of a single hole spinneret (0.813 mm diameter, L/D = 16.4, included angle of 60°), a spacer, breaker plate, and two fine metal mesh filter screens.

The spinning assembly was heated by two independently controlled band heaters. The polymer temperature was monitored by two platinum resistance thermocouples. Spinhead pressure was monitored by a Dynisco pressure transducer (model PT441AE-10M-6130). The extruder screw speed was adjusted to

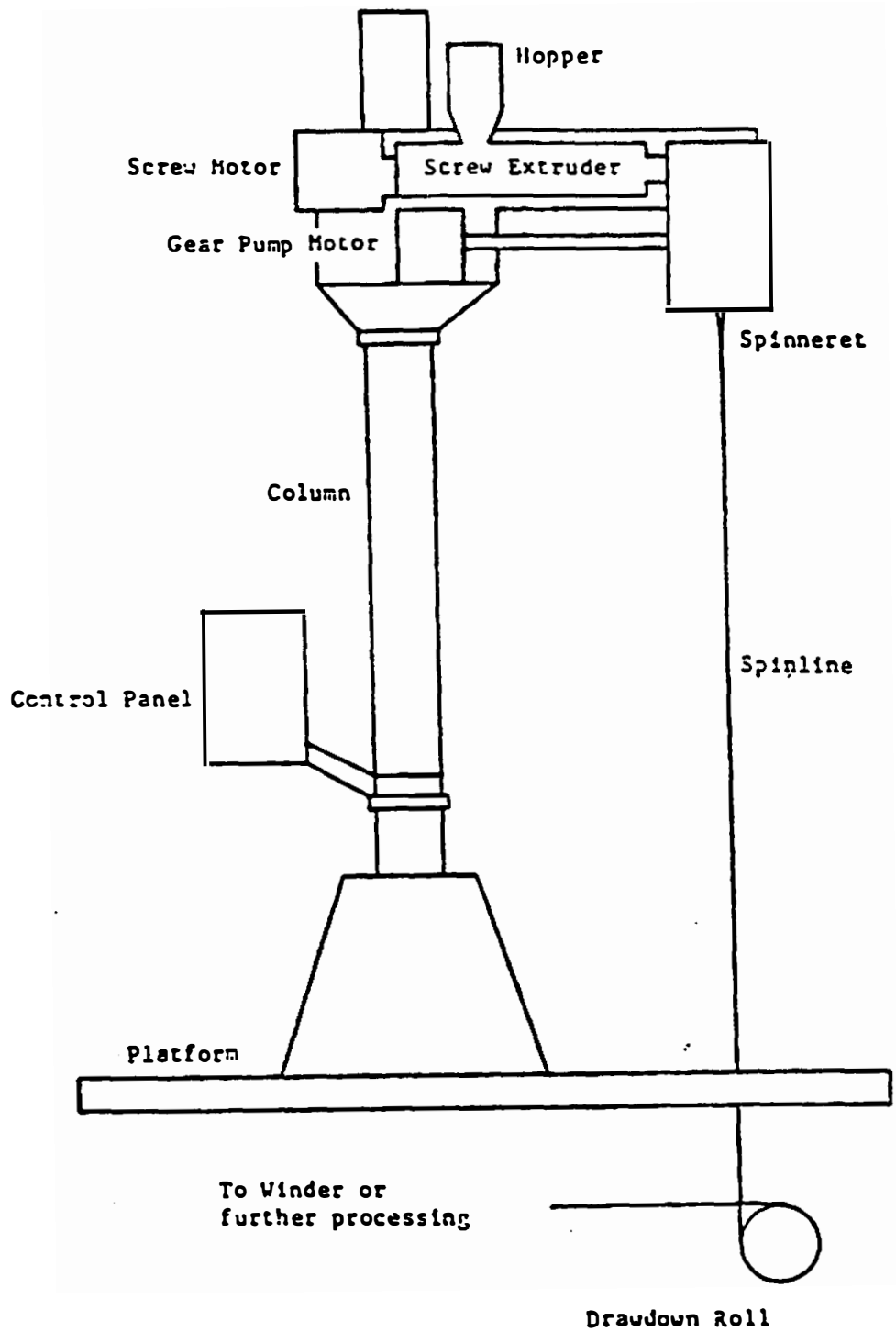

Figure 5. Schematic of the University of Tennessee's melt spinning equipment.

maintain a pressure between 1000 and 1500 psi.

The fiber was drawn down using a textured surface aluminum drum mounted on a B and B NSH-54RL tachometer feedback motor with a matching controller. The fiber was collected on a Lessona model 955 winder. This winder is equipped to wind the fiber at a constant tension.

Operating Procedure

The operating temperatures which were used for all resins were 170, 185, 215, and 215 °C for heater zones 1 through 4, respectively. After the heaters were turned on, at least two hours were required before temperature equilibrium was reached. The extruder screw and gear pump were then checked for free rotation. If no problems were found, the gear pump and extruder were turned on. The feed hopper was then opened. At least one hour was required for the system to void itself of air and for melt pressure to build up and stabilize. The gear pump and extruder speed were then adjusted to achieve the desired mass throughput and melt pressure. The mass throughput was measured by cutting the threadline near the spinneret, collecting the output and weighting it. The procedure was repeated many times to verify the consistency of the mass flow rate. The required motor speeds are listed in Table 4.

To draw down the fiber, the fiber was wrapped around the

Table 4. Required Extruder Speeds

Sample	Mass Flow Rate (g/min)	Fraction Gear Pump Speed	Extruder Screw Speed (rpm)
LL3.9	1.25	0.10	18
LL3.9	2.00	0.49	24
LLP	1.25	0.07	18
LLP	2.01	0.28	24
LL4.3	1.25	0.10	20
LL4.3	2.00	0.32	34

drum and compensator wheel at least three times. The compensator wheel prevents the fibers from rubbing against one another. The fiber is then passed around a constant tension control arm and attached to the bobbin. The combination of the textured drum surface and feed back loop ensured good fiber speed control.

3.5 On-line Measurements

Diameter

The on-line diameter measurements are made with a Zimmer diameter monitor (model 460/2A) and digital controller (model 466/2) built by Zimmer OHG, West Germany. A schematic of the Zimmer and its operating principle is shown in Figure 6. The instrument is based on an electro-optic back illumination principle which permits measurements on both semitransparent and opaque materials. The Zimmer diameter monitor has a measurement range of 0 to 2 mm with a resolution of 0.5 μm.

The Zimmer was interfaced to an IBM-AT personal computer through an A/D converter. A data collection program written by Steve Stiner of the UT Electronics Shop was used to collect the data. This program allows up to 10,000 data points to be collected at a minimum sample time of 1 msec. For this research, 2000 sample points were collected over a 20 second period. The average

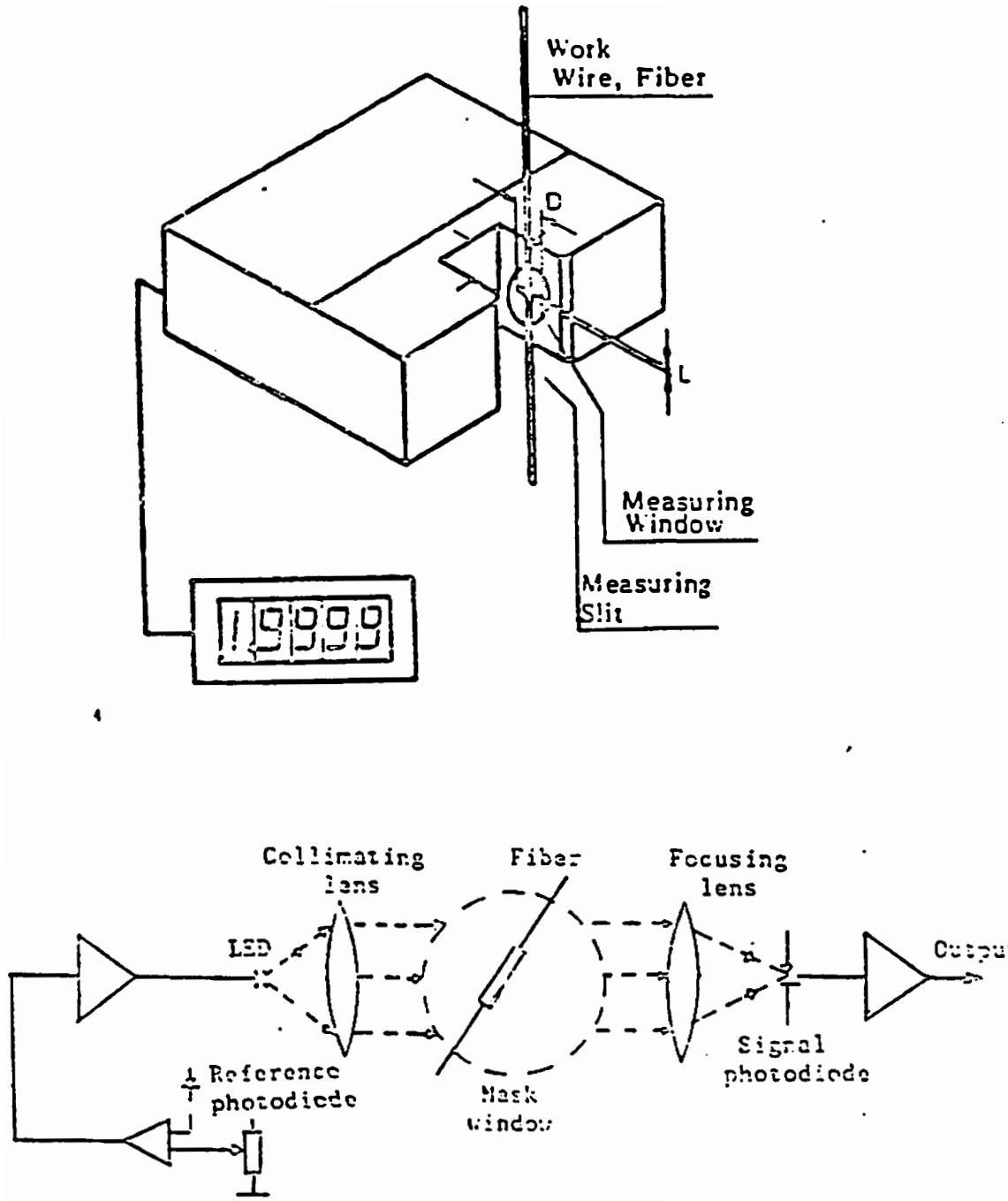

Figure 6. The Zimmer diameter monitor and its operating principle.

diameter was statistically obtained using a computer program written by Lambach [8].

The Zimmer was mounted on a stand which allowed movement up and down the spinline. The Zimmer's electronics required 30 minutes to reach steady state. Before measurement, the Zimmer was zeroed and calibrated with steel wires of known diameter. The spinline measurements were started near the floor and moved up at 5 or 10 centimeter intervals.

Birefringence

On-line birefringence measurements were made using an Olympus polarizing microscope (model 206080) and an Olympus fourth order Berek compensator (model CTPI-200205) to measure optical retardation. The microscope was mounted on a stand which allowed movement up and down the spinline. The microscope was moved to the proper angle and position on the spinline. The fiber was guided to the microscope's viewpoint using an aluminum guide. A schematic of the birefringence measurement setup is shown in Figure 7.

Birefringence measurements were taken with the polars crossed. With the compensator set at its neutral angle (30°), a black band was observed throughout the field of view. When the fiber was brought into view, this black band was shifted. The compensator was adjusted until the two crystal tilt angles which

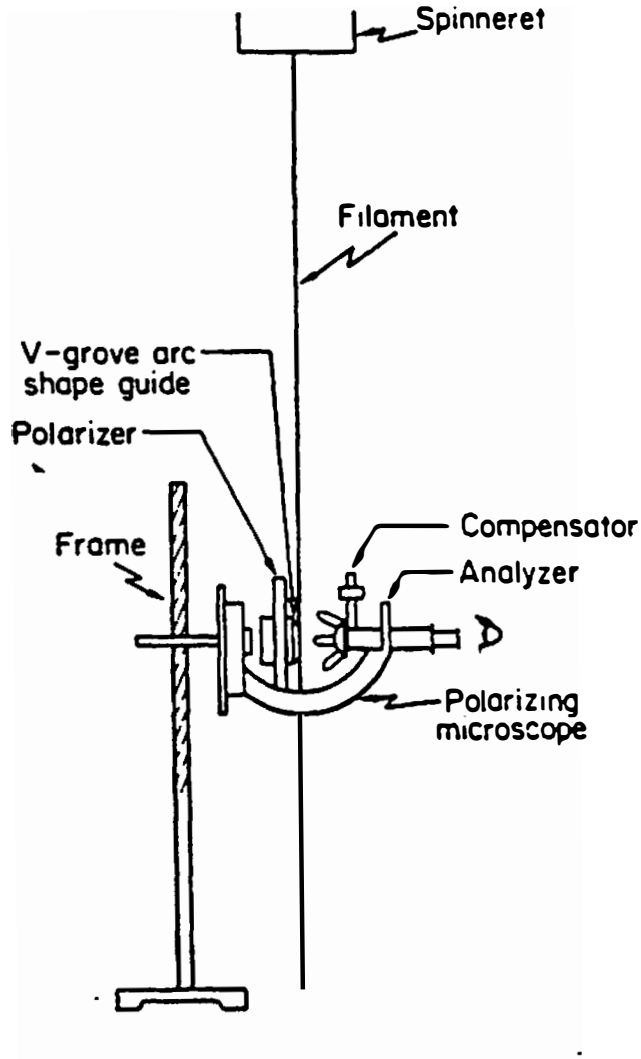

Figure 7. Schematic of on-line birefringence measurement.

brought the black band in the fiber to a chosen reference position were located. The smaller reading was subtracted from the larger reading and the difference divided by two. This value was used with an interpolation table to determine a value which when multiplied by a compensator constant of 0.895, provided the optical retardation in nanometers. The birefringence was then calculated by dividing the retardation by the fiber diameter as measured by the Zimmer.

Temperature

Fiber temperature was measured using a Hughes Thermal Imaging System. This system consists of a infrared video camera, video monitor, image processor, instant imager printer, video cassette recorder, and an IBM-AT personal computer. This system can measure temperatures from -20 to 960 °C with at resolution of 0.5 °C.

The experimental technique and correlations required in order to measure on-line fiber temperature were developed by Hajji [92]. The infrared camera was mounted on a stand which allowed movement up and down the spinline. The camera lens was moved to a distance 3.5 cm from the fiber and then focused until a well defined thermal image was obtained, see Figure 8. The images may be analyzed live or stored for later use on video tape or the IBM's hard disk.

Figure 8. Infrared fiber image.

Temperature analysis requires the determination of the black body temperature profile across the fiber image. This was accomplished by using thermal analysis software provided by Hughes. An example line profile is shown in Figure 9. The peak temperature represents the black body fiber temperature. The actual temperature is then obtained using corrections for emissivity and ambient temperature. At least 8 images were analyzed at each location on the spinline and the results averaged together.

Tension

Spinline tension was determined using a Rothschild Electric Tensionmeter (model INTEG R-1198). The tensionmeter outputs a voltage which is proportional to tension. An IBM-AT personal computer is interfaced to the tensionmeter. The tension at the bottom of the spinline was measured by carefully inserting the tensionmeter into the spinline. A computer program written by Steve Stiner of the UT Electronics Shop was used to collect 2000 readings from the tensionmeter within 20 seconds. A computer program written by Lambach [8] was used to average the voltages.

To calibrate the tensionmeter, polyethylene fibers with attached weights were slowly pulled through the tensionmeter by a variable speed electric motor. Fibers used for calibration

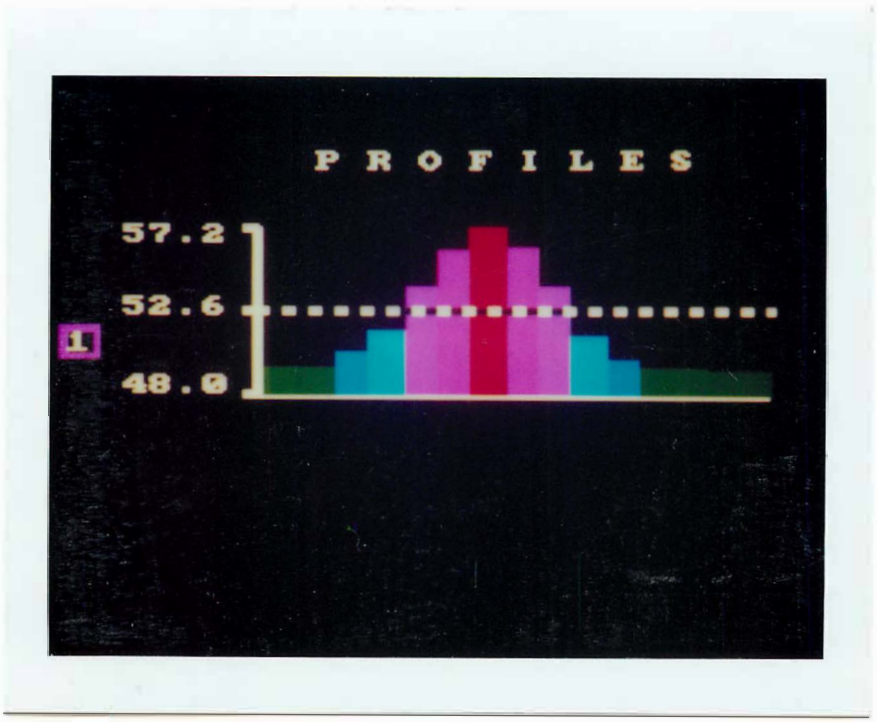

Figure 9. Fiber temperature line profile.

were of the same material and approximately the same diameter as for the on-line measurement. Voltage data for a series of weights was obtained. Using these values, the on-line tension was obtained.

3.6 Characterization of As-spun Fibers

Density and Crystallinity

The density of the as-spun fibers was determined using a density gradient column (DGC) prepared from an isopropanol-water mixture. Standard laboratory procedure was followed in preparing the column. A detailed discussion of this procedure is found in Appendix A of Wust's Ph.D. dissertation [93]. The column was calibrated using standard glass beads of known density. Samples were wetted with an isopropanol-water solution before introduction to the column. The samples were allowed to equilibrate for 24 hours before their position was recorded. At least three replicates from each sample were added to the column. The average value was used in equation (3-3) to calculate the weight-fraction crystallinity.

$$\Theta = \frac{\rho_c (\rho - \rho_a)}{\rho (\rho_c - \rho_a)} \qquad (3\text{-}3)$$

where ρ is the fiber density, ρ_a and ρ_c are the theoretical densities of the amorphous and crystalline phases. These values can be obtained from appropriate references.

Diameter

The Zimmer was used for static diameter measurements. The fibers were affixed to a mounting plate with double stick tape and placed in the Zimmer's field of view. At least six replicate fiber samples were measured, and the average diameter reported.

Birefringence

Static birefringence measurements were made by placing the mounting plate with attached fiber in the proper orientation under the polarizing microscope. The same techniques used to determine on-line retardation and birefringence were used for the static measurements.

Wide Angle X-ray Scattering

Wide angle x-ray scattering (WAXS) patterns were obtained from a Statton flat plate camera mounted on a Phillips-Norelco water-cooled x-ray generator (model 12045B). The x-ray unit

emitted nickel filtered CuKα radiation of wavelength 1.542 Å. The unit was operated at 30 kV and 20 mA. Samples were prepared by winding the fiber on a Warhus yarnholder/pinhole collimator until the sample bundle was 1 to 1.5 mm thick. The yarnholder has a 0.025 inch pinhole and a 0.040 inch shelf. The yarnholder was mounted in the camera normal to the x-ray beam. Kodak Blue Brand x-ray film was mounted 3 cm from the yarnholder. Exposure time was four hours. The films were developed in Kodak Industrex developer for three minutes, fixed in Kodak Rapidfix for ten minutes and then placed in a water bath for 15 minutes.

CHAPTER 4

RESULTS AND DISCUSSION

4.1 Isothermal Crystallization Studies

The purpose of these isothermal studies is to obtain crystallization kinetics data which can be used to make relative comparisons between the samples and to obtain the parameters required to predict non-isothermal crystallization kinetics from isothermal data. Isothermal crystallization kinetics were studied using Depolarized Light Microscopy (DLM) as described in Section 3.2. These polymer samples were observed to rapidly nucleate. Generally, the spherulites which developed were small, ill-defined, and overlapping. This prevented the use of spherulite radial growth rates to study crystallization kinetics and necessitated the use of half time analysis.

Half Time Analysis

The half times are obtained from the crystallization isotherms. An example of the isotherms obtained is shown in Figure 10. The half time was taken as the time at which relative crystallinity = 1/2. In this research, the induction time was

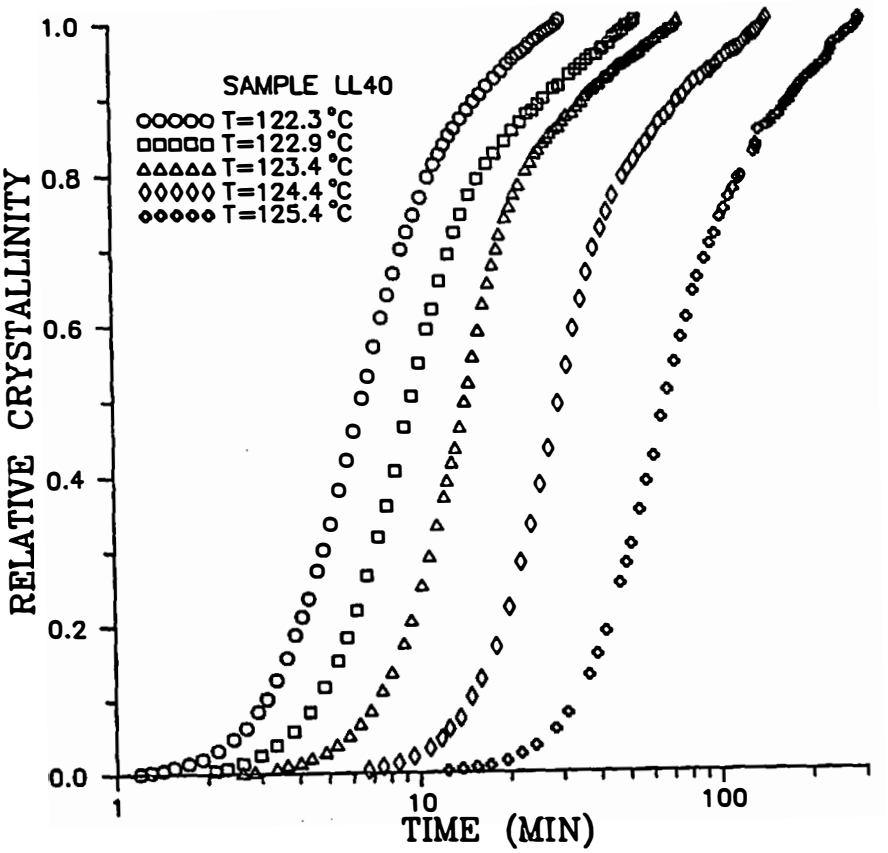

Figure 10. LL40 crystallization isotherms.

included in the half times.

Four of the samples studied: LL2, LL3.3, LL3.9, and LL4 exhibited isotherms which are markedly different than those found for the other resins. Figure 11 shows the isotherms for LL3.9. Notice the lack of superposability except at low values of crystallinity. This identical behavior was observed by Mandelkern [41,94] in his study of polyethylene containing noncrystallizing units. The author postulated that the lack of superposability was due to the changing composition of the melt as noncrystallizing units were rejected from the crystalline phase during transformation. The samples which show a lack of superposability also possess broad ATREF curves. This suggests that a large variance in SCB induces large differences in the melt composition as transformation progresses. A comparison of the superposability of these resins with M_n reveals that as M_n decreases, the superposability generally decreases. This may be due to a reduction in the distribution of branch free chain segments, as caused by a reduction in chain length. However without knowledge of the actual distribution of branches on a chain, this should be considered as speculation. Isotherms for all resins are found in Appendix B.

The reciprocal half times obtained from these isotherms are plotted versus crystallization temperature in Figure 12. This figure clearly indicates that large differences in crystallization kinetics exist between these resins. No single parameter can

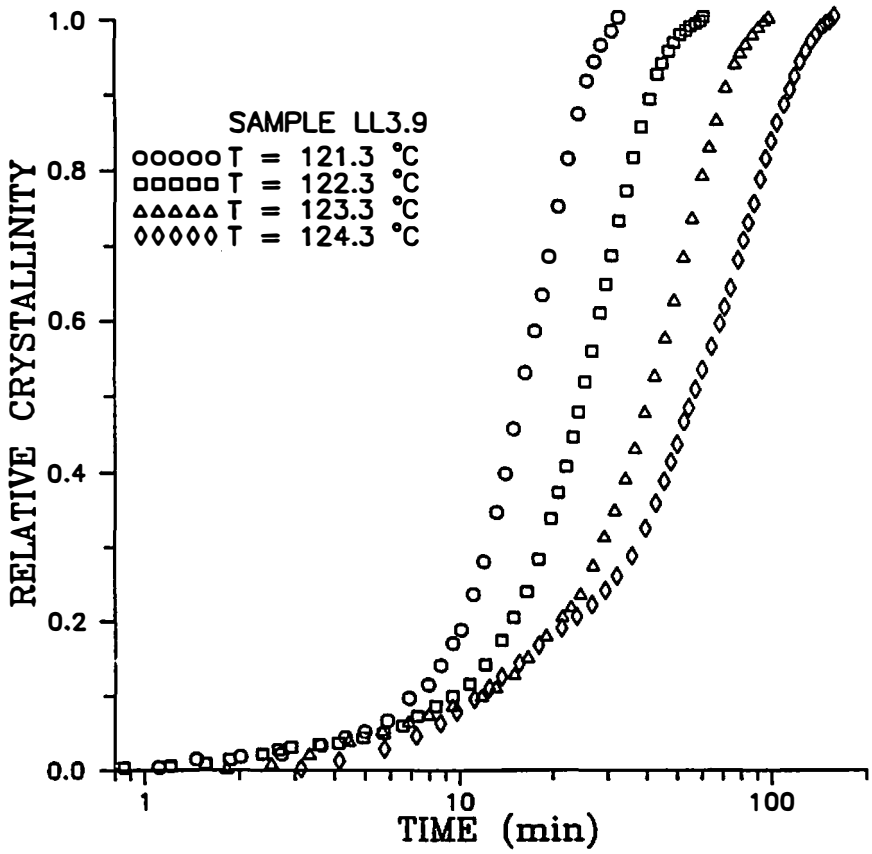

Figure 11. LL3.9 crystallization isotherms.

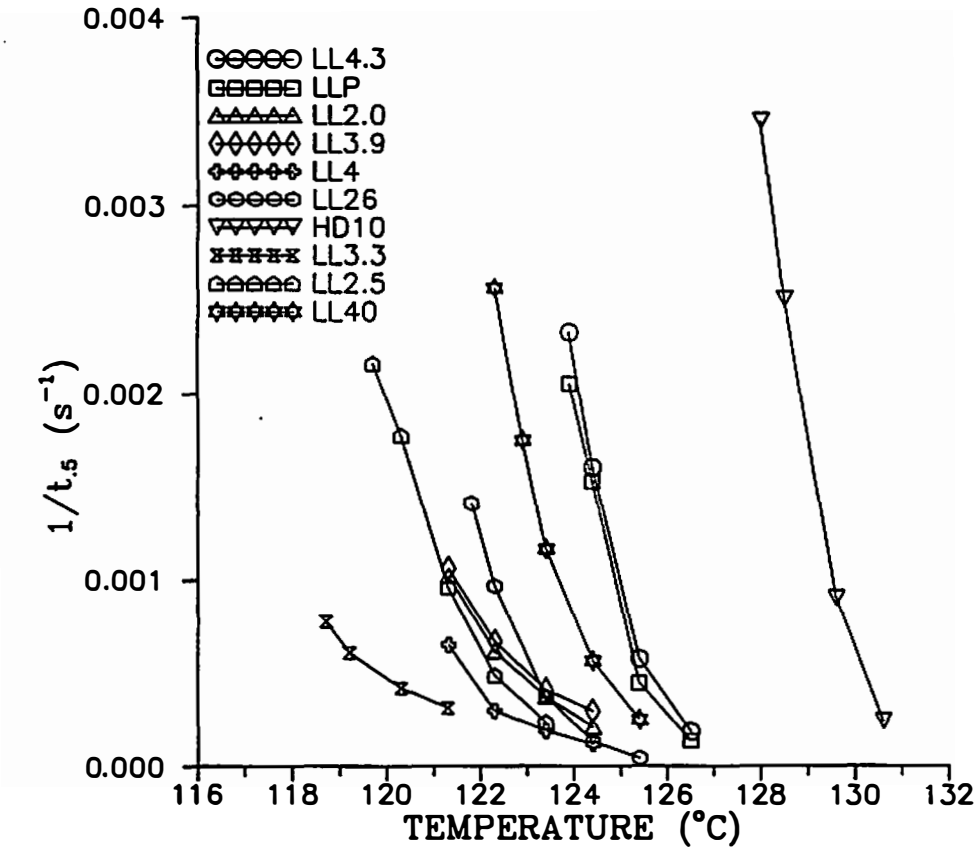

Figure 12. $1/t_{1/2}$ versus crystallization temperature.

correlate $1/t_{1/2}$ versus T_c for all samples; however, the general trend is that a decrease in density brings about a decrease in the crystallization rate at a given temperature, see Figure 13. It would appear that the samples requiring smaller supercoolings to obtain a given crystallization rate are those which possess the higher crystalline order. Many investigators have studied the effects of copolymerized units, branches, and other defects on the melting behavior of polymers and have reported similar results [41,95-102].

The half time may be related to temperature by equation (2-26).

$$\frac{1}{t_{1/2}} = \left(\frac{1}{t_{1/2}}\right)_0 \exp\left[\frac{-U^*}{R(T-T_\infty)}\right]\exp\left[\frac{-C_3}{T\Delta T}\right] \qquad (2\text{-}26)$$

Equation (2-26) represents a combination of both nucleation and growth rates as has been determined by Hammami [60]. By plotting $\ln(1/t_{1/2}) + U^*/R(T-T_\infty)$ versus $-1/T\Delta T$ one can obtain C_3 and $(1/t_{1/2})_0$ [58,59], see Figure 14. The values of $\ln(1/t_{1/2})_0$ and C_3 are found in Table 5.

At this time it is helpful to examine what $(1/t_{1/2})_0$ and C_3 actually represent. Recall that equation (2-26) is derived from growth theory and therefore the coefficients $(1/t_{1/2})_0$ and C_3 have fundamental meanings based on growth theory whenever nucleation density can be assumed constant. In this case the pre-

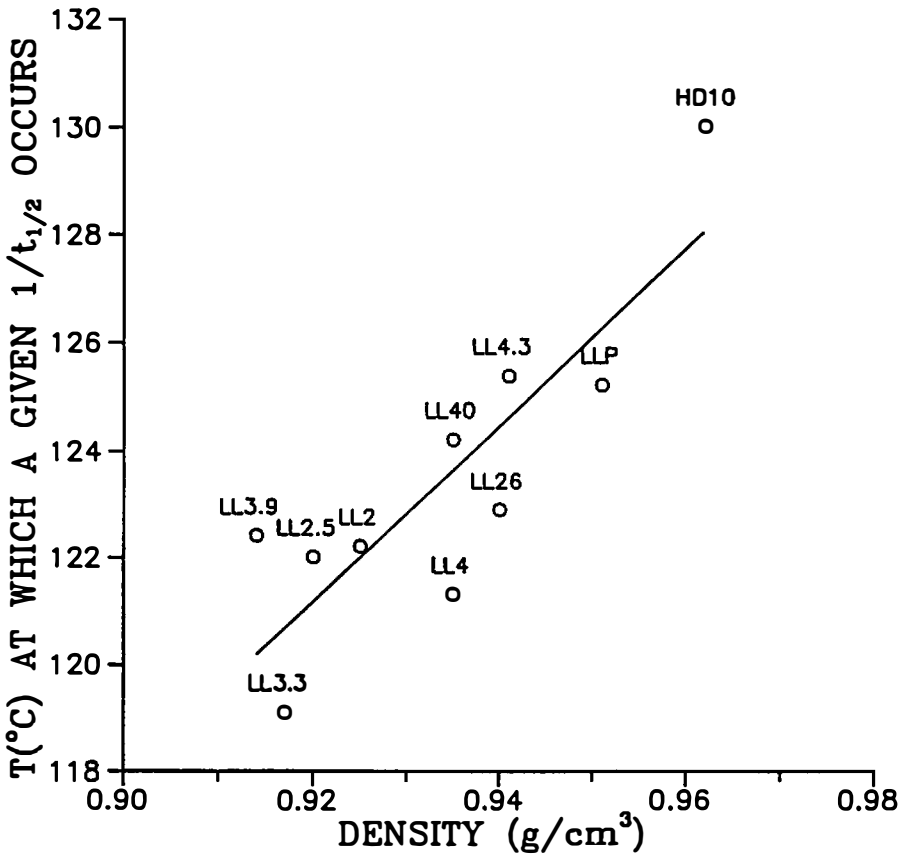

Figure 13. Temperature at which a given $1/t_{1/2}$ occurs versus density.

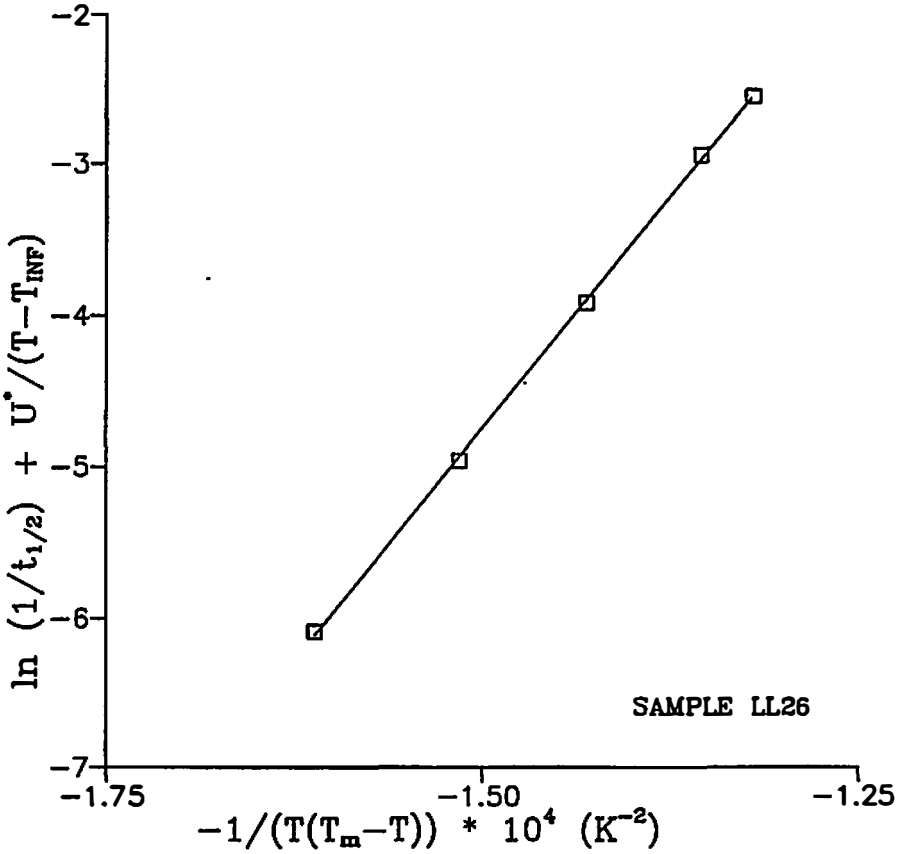

Figure 14. Determination of $(1/t_{1/2})_0$ and C_3.

Table 5. Isothermally Obtained Crystallization Kinetic Parameters

Sample	$\ln(1/t_{1/2})_0$ $\ln(s^{-n})$	$C_3 \times 10^{-3}$ (K^2)
LL2	6.31	71.4
LL2.5	9.94	100
LL3.3	4.60	67.4
LL3.9	4.75	59.3
LLP	14.5	112
LL4	6.26	75.4
LL4.3	13.2	103
LL26	13.6	122
LL40	10.4	91.8
HD10	9.69	59.3

exponential coefficient $(1/t_{1/2})_0$ is named G_0 in Hoffman and Lauritzen's growth rate theory [25]. G_0 is a term which contains many prefactors and is formulated differently depending on the crystallization regime [32]. For regime I,

$$G_{0I} = b\left(\frac{kT}{h}\right) n_s J_1 \exp\left(\frac{2ab\sigma_e\Psi}{kT}\right) \qquad (4\text{-}1)$$

and for regime II

$$G_{0II} = b\left(\frac{kT}{h}\right) J_1 \exp\left\{(2\Psi\text{-}1)\frac{ab\sigma_e}{kT}\right\} \qquad (4\text{-}2)$$

where a is the distance between chain segments on a nucleus, b is the thickness of a chain segment, kT/h is the frequency of thermally activated vibrations, n_s is the number of sites where a polymer chain may attach, J_1 is a term which refers to all remaining barriers not considered in the exp $[U^*/R(T-T_\infty)]$ term, σ_e is the fold surface free energy/unit volume, and Ψ is a parameter dependent on the path by which the first step chain segment is attached to the surface of the nucleus [32]. The significance of the parameters which are relevant to this research will now be discussed.

The J_1 factor is represented by

$$J_1 = \exp\left[\frac{-\Delta F^*}{RT}\right] \qquad (4\text{-}3)$$

J_1 typically ranges from 10^{-2} to 10^{-5} and tends to reduce the value of G_0. The critical free energy of nucleus formation, ΔF^* is given by

$$\frac{\Delta F^*}{RT} = \frac{\Delta H^*}{RT} - \frac{\Delta S^*}{R} \qquad (4\text{-}4)$$

ΔH^* is usually considered to be independent of branching, however branching will effect ΔS^*. An increase in branching (thus an increase in disorder) will cause a reduction in ΔF^*. A reduction in ΔF^* will cause an increase in J_1 therefore G_0 would be expected to increase as branching increases. The fold surface energy may be expressed as [103]

$$\sigma_e = \left(\frac{q}{a\,b}\right) + \sigma_{eo} \qquad (4\text{-}5)$$

where q is the work required to form the fold by bending the chain back upon itself in the appropriate configuration and σ_{eo} is the value of the surface free energy if no work was required to form the fold. If a polymer was highly branched, the steric hindrance present would prevent certain conformations from occurring thereby increasing the value of σ_e and therefore the value of G_0. Mandelkern [94] observed large increases in calculated values of σ_e as copolymer content increased.

The constant Ψ takes on different values depending on the way a polymer chain joins the surface [57]. If a chain attaches itself to the nucleus in a crystallographic fashion and if each chain segment simultaneously obtains both its lateral surface and free energy of fusion then $\Psi = 1$. Alternately, the polymer molecule may be adsorbed into the surface in a non-crystallographic fashion, in which case a "localized migration" is required before crystallographic crystallization may occur. This migration will lead to values of $\Psi < 1$. If a polymer is extensively branched, then instant crystallographic attachment to the surface becomes less likely and G_0 will decrease as branching increases. To test these ideas, log $(1/t_{1/2})_0$ is plotted against density, see Figure 15. A relationship between density and $(1/t_{1/2})_0$ may exist, however considerable scatter is present. Hammami [60] determined both $(1/t_{1/2})_0$ and G_0 for several polypropylenes. He observed a consistent difference between these values which he attributed to nucleation effects in the half time analysis. Therefore $(1/t_{1/2})_0$ should not be used to draw direct conclusions about G_0. Judgements about the relative effects of J_1, σ_e, and Ψ should only be considered as speculation.

In Hoffman and Lauritzen's growth rate theory [25], the coefficient C_3 is named K_g. K_g is related to the free energy required to form a critically sized nucleus and is given as

$$K_g = \frac{\gamma b \sigma^2 \sigma_e T_m^o}{k \Delta H} \qquad (4\text{-}6)$$

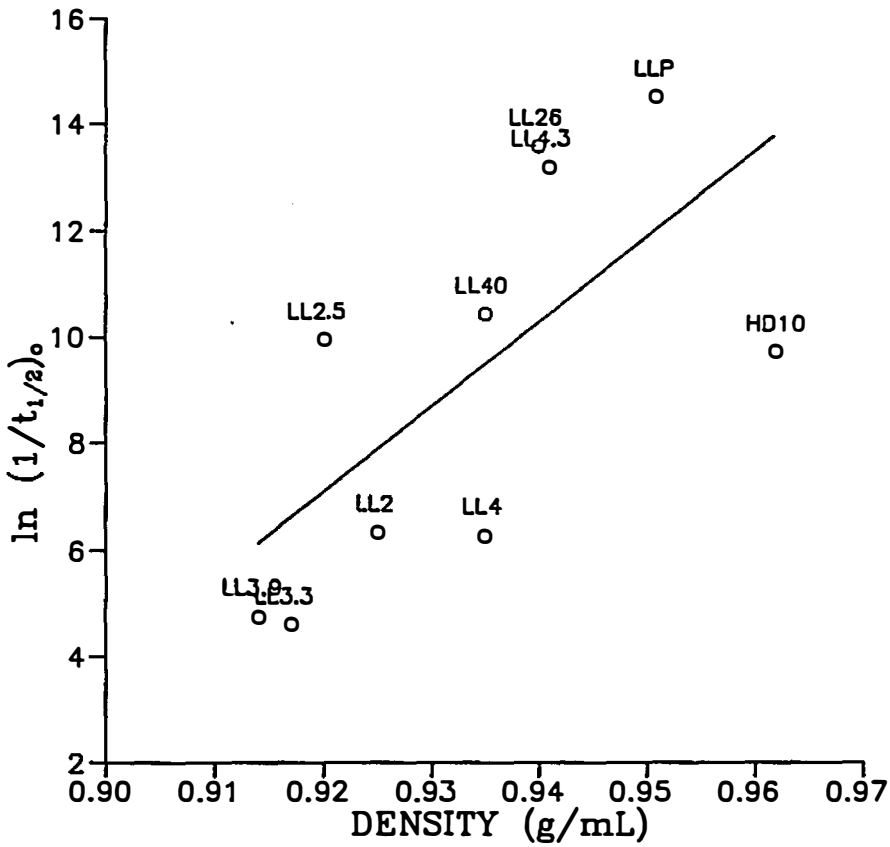

Figure 15. Logarithm of $(1/t_{1/2})_0$ versus density.

where $\gamma = 4$ for regime I crystallization and $\gamma = 2$ for regime II crystallization. In this expression ΔH has units of energy/volume. However enthalpies of fusion typically have units of energy/mass. One can write

$$\Delta H\left(\frac{\text{energy}}{\text{volume}}\right) = \Delta H^{\dagger}\left(\frac{\text{energy}}{\text{mass}}\right)\cdot\rho\left(\frac{\text{mass}}{\text{volume}}\right) \qquad (4\text{-}7)$$

and so if ΔH is essentially constant and the other parameters in equation (4-6) do not vary,

$$K_g \sim \frac{1}{\rho} \qquad (4\text{-}8)$$

In Figure 16, C_3 is plotted against $1/\rho$. For the LLDPE's a trend is clearly observed, as ρ increases C_3 increases. K_g can also be written as:

$$K_g = \frac{\gamma b \sigma^2 \sigma_e}{(\Delta f)kT} \qquad (4\text{-}9)$$

where Δf is the bulk free energy of fusion equal to $\Delta H(\Delta T)/T_m^o$. If the other parameters do not change much, then

$$K_g \sim \frac{1}{\Delta f} \qquad (4\text{-}10)$$

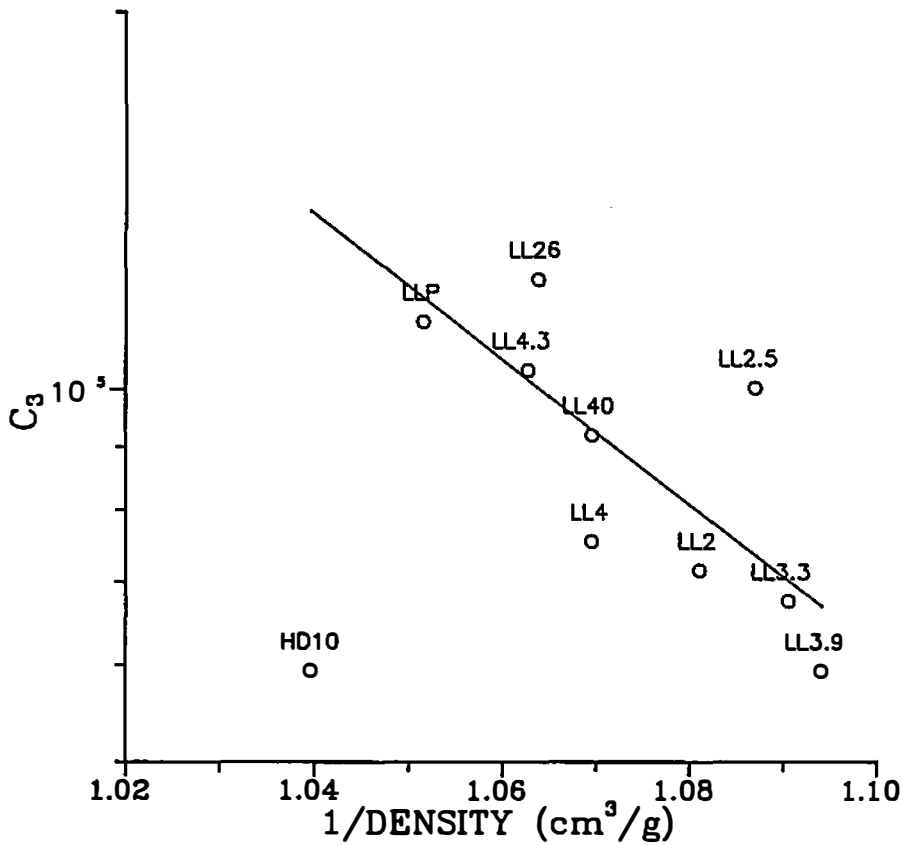

Figure 16. C_3 versus $1/\rho$.

Equation (4-10) indicates that as the critical free energy required for nucleus formation decreases, K_g increases. In other words, a sample having a high value of K_g has a lower barrier to nucleus formation. This suggests that polyethylene resins with higher density will nucleate and crystallize sooner at a given temperature than those with lower densities. This behavior was experimentally observed in this research. Hammami [60] also observed that the values of K_g and C_3 varied with copolymer content for several polypropylenes.

Avrami Analysis

Isothermal crystallization behavior can be modeled using the Avrami equation.

$$\frac{\Theta(t)}{\Theta(\infty)} = 1 - \exp(-kt^n) \qquad (2\text{-}11)$$

where $\Theta(t)$ is the crystallinity at time t, $\Theta(\infty)$ is the ultimate crystallinity, k is a rate constant containing both nucleation and growth mechanisms, and n is the Avrami index. By rearranging equation (2-11) and taking logarithms, equation (2-11) becomes

$$\ln [-\ln(1-\Theta/\Theta_\infty)] = \ln k + n \ln t \qquad (4\text{-}11)$$

By plotting the left hand side versus ln t, n and k may be

determined, see Figure 17. The rate constant k may also be obtained from the half time.

$$k = \frac{\ln(2)}{t_{1/2}^{n}} \qquad (4\text{-}12)$$

This figure exhibits a feature common for these resins. The slope of the line (n) varies as crystallization progresses. This behavior has been reported before for polyethylene and its copolymers and is usually attributed to secondary crystallization. This behavior has led some workers to use two Avrami equations either in serial or parallel in an attempt to more accurately represent the entire crystallization range. Banks et al. [45] applied two Avrami equations in parallel and series to describe consecutive and concurrent primary and secondary crystallization processes respectively. Hillier [46] proposed a modified Avrami equation consisting of two consecutive process, with the second process varying linearly with log time. Velisaris and Seferis [47] considered that bulk crystallization should involve two competing nucleation and growth processes. They proposed a linear combination of Avrami equations:

$$\frac{\Theta(t)}{\Theta(\infty)} = w_1\left[1-\exp(-k_1(T)t^{n1})\right] + w_2\left[1-\exp(-k_2(T)t^{n2})\right] \qquad (2\text{-}17)$$

where for the ith process, k_i is the temperature dependent

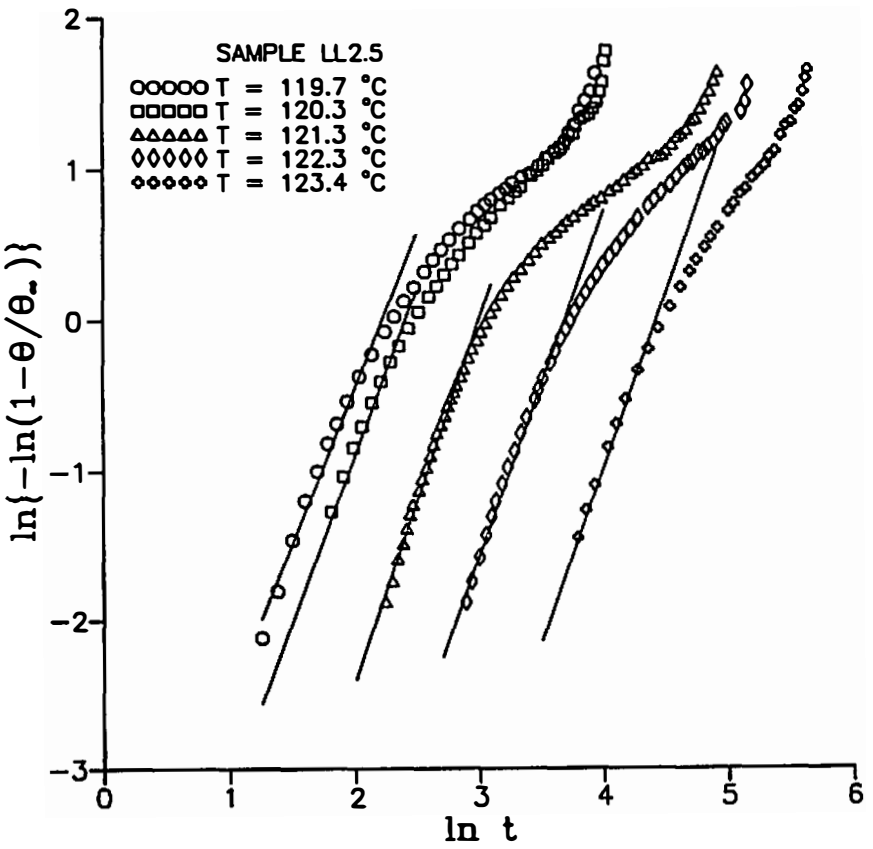

Figure 17. Avrami plot for LL2.5.

crystallization rate constant, n_i is the Avrami index and w_i is the weight fraction. The sum of the weight fractions $w_1 + w_2 = 1$.

One of the main goals of this research project was to understand the effect of stress on crystallization in the upper part of the melt spinline. For this purpose, fundamental understanding of the Avrami index was not necessary. The Avrami index was graphically determined over the range $0.1 < \Theta < 0.6$ to avoid difficulties associated with unusual birefringence variations during the initial and latter stages of crystallization.

Knowing $t_{1/2}$ and n, the crystallization isotherms can be modeled. Model predictions for LL40 are found in Figure 18. The predictions are quite good except in the region above 60% crystallinity. Above this region, secondary crystallization becomes important. A single Avrami equation (2-11) cannot deal with the effect of secondary crystallization.

Dietz [104] has suggested the addition of an "attenuation-function"

$$h(X) = \exp\left[\frac{-aX}{1-X}\right] \qquad (4\text{-}13)$$

to the Avrami equation in order to deal with the effects of secondary crystallization. Hammami [60] has used equation (4-13) to correct for some of the effects of secondary crystallization in polypropylene. The use of equation (4-13) for polyethylene will be explored in the future.

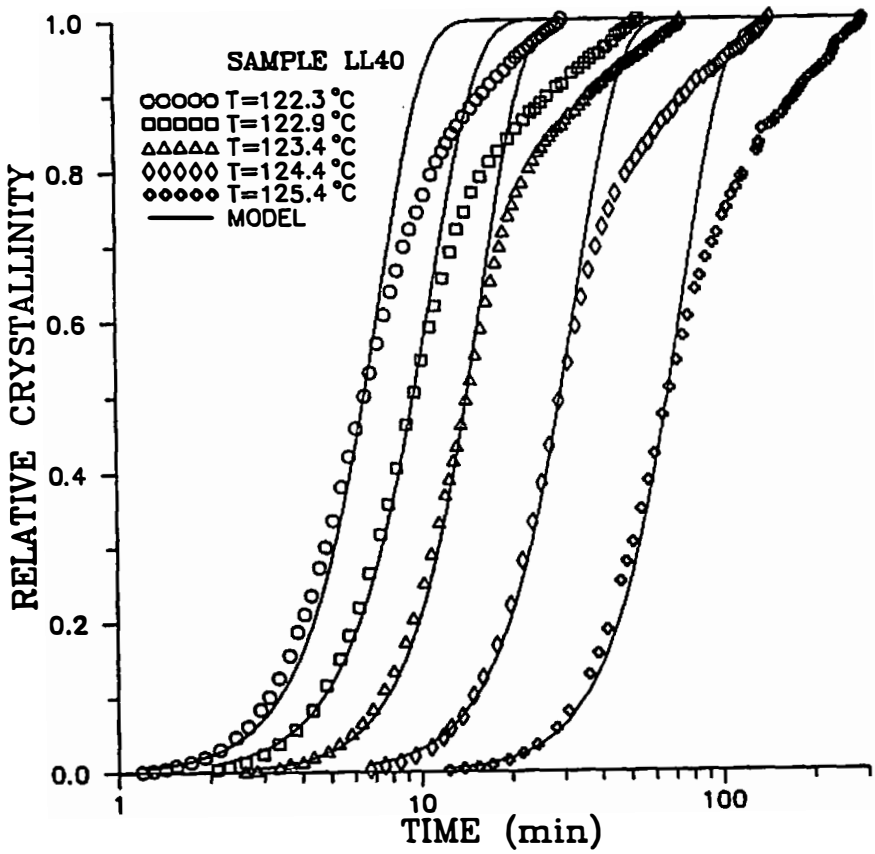

Figure 18. Isothermal crystallization model predictions for LL40.

The Avrami indices are listed in Table 6 and 7. For the most part, non-integer Avrami indices were found. The presence of secondary crystallization may introduce fractional components to the Avrami index [105,106]. Banks and his associates [107] considered that fractional Avrami indices may be due to a variation in a spherulite's density as it grows. However the authors were unable to suggest a mechanism to explain this decrease. Several of the resins have Avrami indices which are less than two. Avrami indices less than one have been reported for seeded polyethylene [108]. In this research project, the samples were heated above their equilibrium melting temperature for sufficient time to ensure melting of all crystallites [109]. This however does not preclude the existence of any inorganic heterogeneities capable of promoting epitaxial growth.

In Figure 19, the average Avrami index is plotted against the number of methyls/1000 C atoms. There does appear to be a relationship between n and the amount of branching. However the Avrami index must be dependent on many parameters. The nucleation and growth mechanisms are known to influence the Avrami indices. For this study, no conclusions will be made as to the nucleation and growth mechanisms present based on the experimentally obtained Avrami indices. Banks et al. [17,107] have concluded that the Avrami index should not be used to make conclusions about the nucleation and growth mechanism whether these values are fractional or integer.

Table 6. Avrami Indices for Broad ATREF Samples

Resin	Sample	Avrami Index
LL2	121.3	1.91
	122.3	1.78
	123.4	1.56
	124.4	1.14
LL2.5	119.7	2.07
	120.3	2.22
	121.3	2.41
	122.3	2.29
	123.4	2.33
LL3.3	118.2	1.84
	119.2	1.55
	120.3	1.34
	120.8	1.34
	121.3	1.21
LL3.9	121.3	2.59
	122.3	2.28
	123.4	1.97
	124.4	1.60
LL4	121.3	2.63
	122.3	2.09
	123.4	1.56
	124.4	1.45

Table 7. Avrami Indices for Narrow ATREF Samples

Resin	Sample	Avrami Index
LLP	123.9	3.07
	124.4	2.55
	125.4	3.53
	126.5	3.28
LL4.3	123.9	2.91
	124.4	3.42
	125.4	3.65
	126.5	3.68
LL26	121.8	1.55
	122.3	2.05
	123.4	2.34
	124.4	2.47
	125.4	2.25
LL40	122.3	2.84
	122.9	2.67
	123.4	3.00
	124.4	2.84
	125.4	2.97
HD10	128.0	3.98
	128.5	3.88
	129.6	4.00
	130.6	3.86

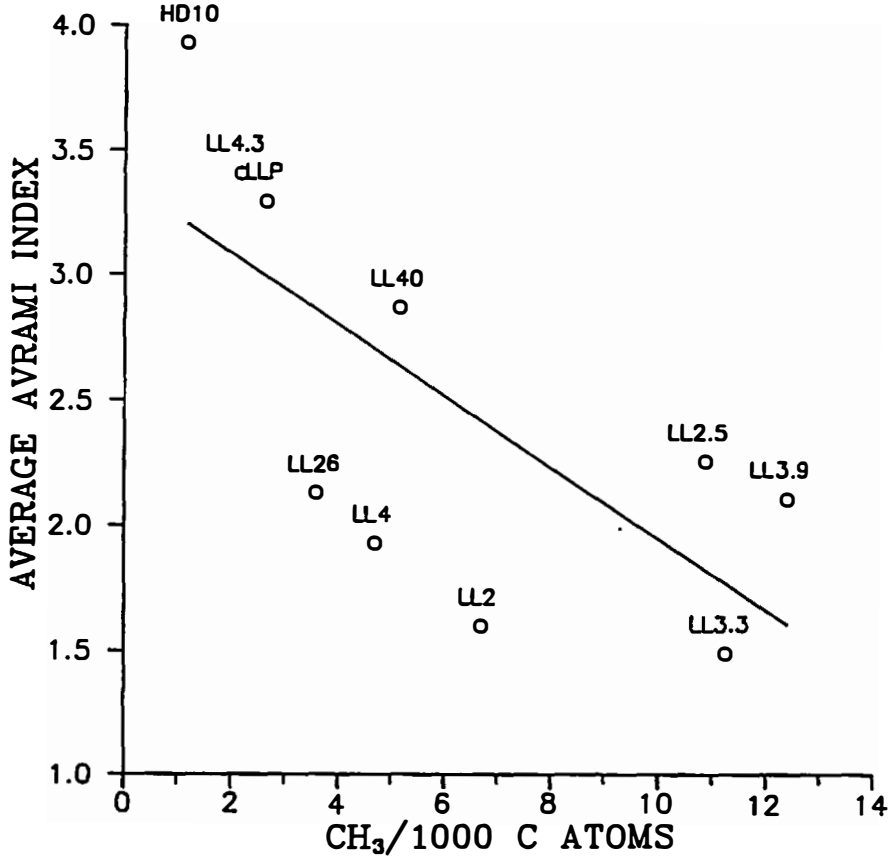

Figure 19. Average Avrami index versus methyl groups per 1000 carbon atoms.

Morphology

It was never the intent of this project to rigorously study the supermolecular structures developed from isothermally crystallized LLDPE resins; however, photomicrographs were taken to represent typical structures. Samples LL2 and LL2.5 exhibited large spherulites ≈ 40 μm. As T_c increases the spherulites are less well developed. Figure 20 shows photomicrographs for LL2 when $t \approx t_{1/2}$. For the other resins, smaller and more irregular spherulites are present. Figure 21 shows the structure developed for LL40 with $t \approx t_{1/2}$. The spherulites are quite small and poorly defined. The small angle light scattering (SALS) H_v pattern for LL40 isothermally crystallized at 119 °C is displayed in Figure 22. The four-lobed pattern typical of a spherulite is present although it is not as distinct as those which can be obtained from a linear polyethylene. The spherulite diameter calculated from SALS data is 33 μm. This is somewhat higher than what is observed in Figure 21 however diameters obtained from SALS represent an average throughout the sample and are weighted towards the diameter of larger structures.

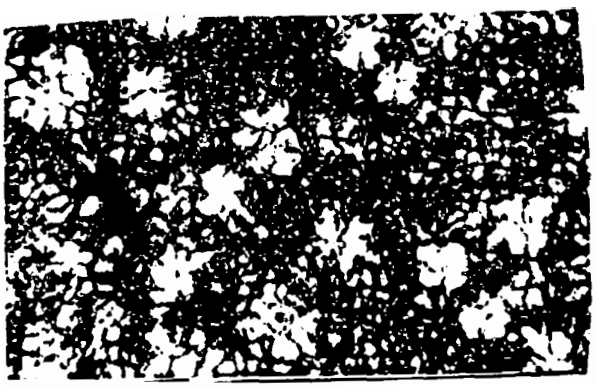

T_c = 118 °C

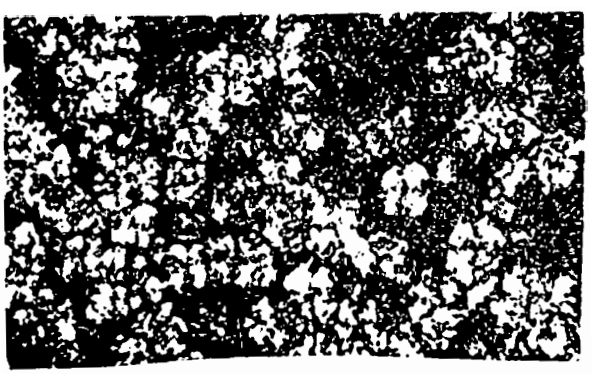

T_c = 120 °C

100 µm

Figure 20. LL2 photomicrographs.

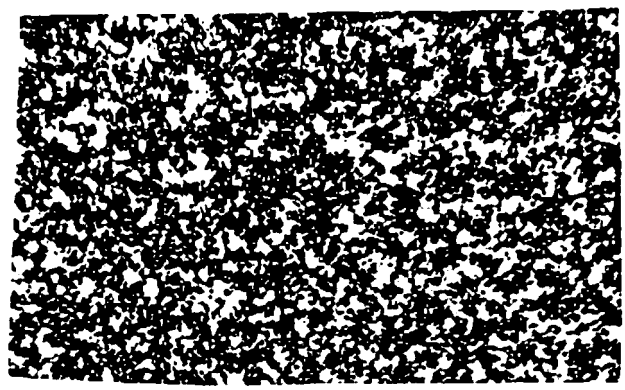

T_c = 119 °C

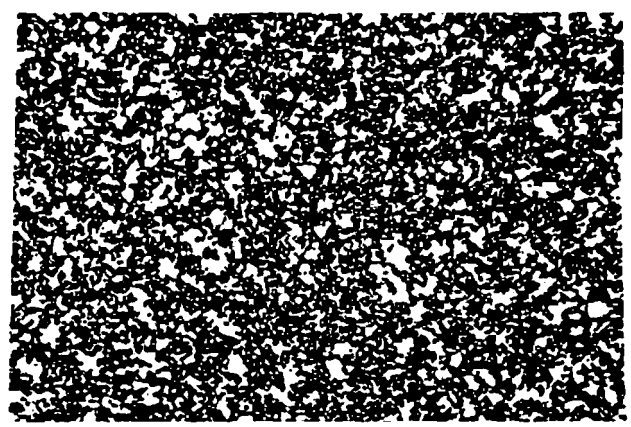

T_c = 120 °C

100 µm

Figure 21. LL40 photomicrographs.

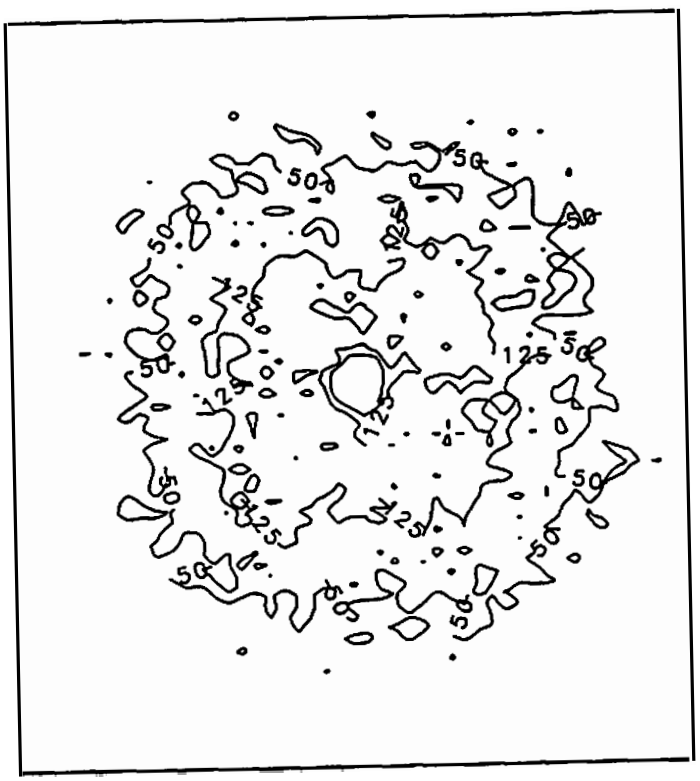

Figure 22. SALS H_v pattern for LL40 isothermally crystallized at 119 °C.

4.2 Non-isothermal Studies

The purpose of the non-isothermal studies is to obtain non-isothermal crystallization kinetics data which can be used to make relative comparisons between the samples and to establish whether non-isothermal crystallization kinetics can be predicted from isothermal crystallization data. Non-isothermal crystallization kinetics were studied using differential scanning calorimetry (DSC) as described in Section 3.3.

A typical set of non-isothermal crystallization curves is shown in Figure 23. Notice an increase in cooling rate results in a delay in the onset and half time of crystallization. As cooling rate increases, less time is available for the polymer molecules to organize themselves into a crystallizable group and a greater degree of supercooling is required to achieve a given level of crystallinity. Non-isothermal crystallization curves for all resins are found in Appendix C.

A convenient way to demonstrate this behavior is to use the Continuous Cooling Transformation (CCT) approach [12]. In the CCT approach, the temperature at which a given level of crystallinity occurs is plotted against the cooling time required to achieve this level of crystallinity. For 50% relative crystallinity the cooling time is given by equation (4-14).

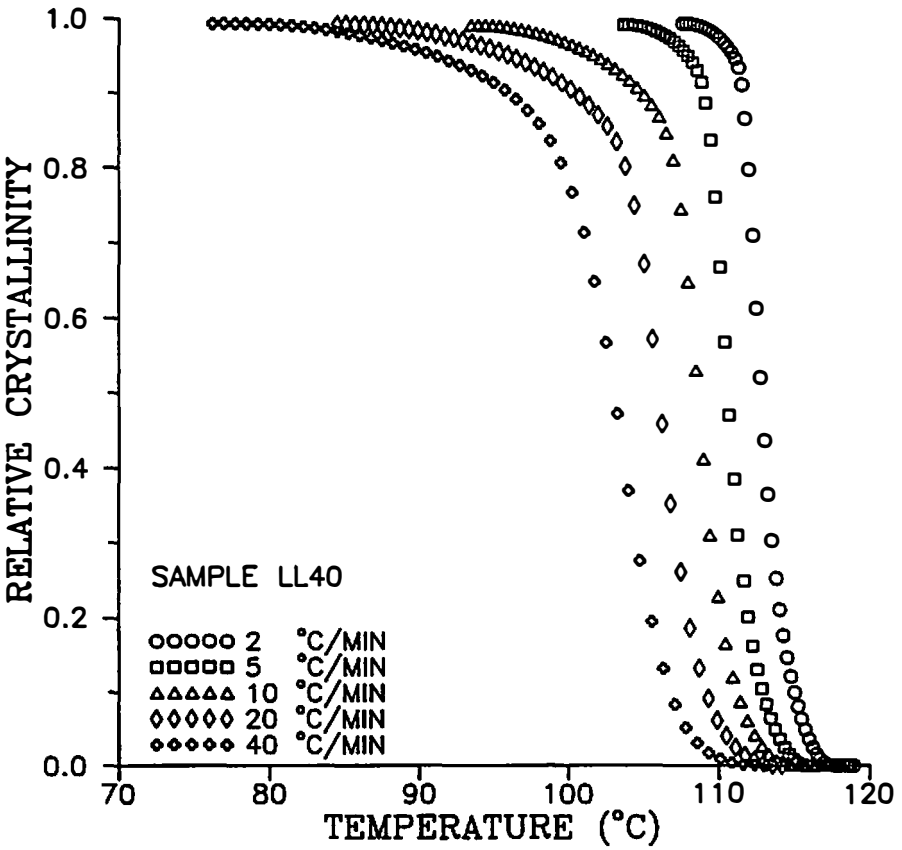

Figure 23. LL40 non-isothermal crystallization curves.

$$\text{Cooling Time} = \frac{T_m^o - T(\Theta(T)/\Theta(\infty)=1/2)}{\text{Cooling Rate}} \qquad (4\text{-}14)$$

where T_m^o = 141 °C [111]. The CCT curves for each resin are plotted on Figure 24. Notice that as cooling time decreases (cooling rate increases), the temperature decreases in a non-linear fashion. Figure 24 also serves as a convenient way to compare the relative non-isothermal crystallization behavior of the resin. The samples with higher crystallinity are observed to crystallize sooner and at higher temperatures than the less dense resins. This identical behavior was observed in the isothermal studies. A clear representation of this behavior is obtained by plotting half time temperatures versus density for the 2 °C/min cooling rate experiments, see Figure 25. This figure clearly shows that an increase in density causes increased in crystallization rate.

The effect of density on the temperature of crystallization may be explained by considering the entropy of the crystallizing system. The free energy of a system may be written as

$$\Delta F = \Delta H - T\Delta S \qquad (4\text{-}15)$$

For the case of an equilibrium phase change equation (4-15) may be rearranged to

$$T = \frac{\Delta H}{\Delta S} \qquad (4\text{-}16)$$

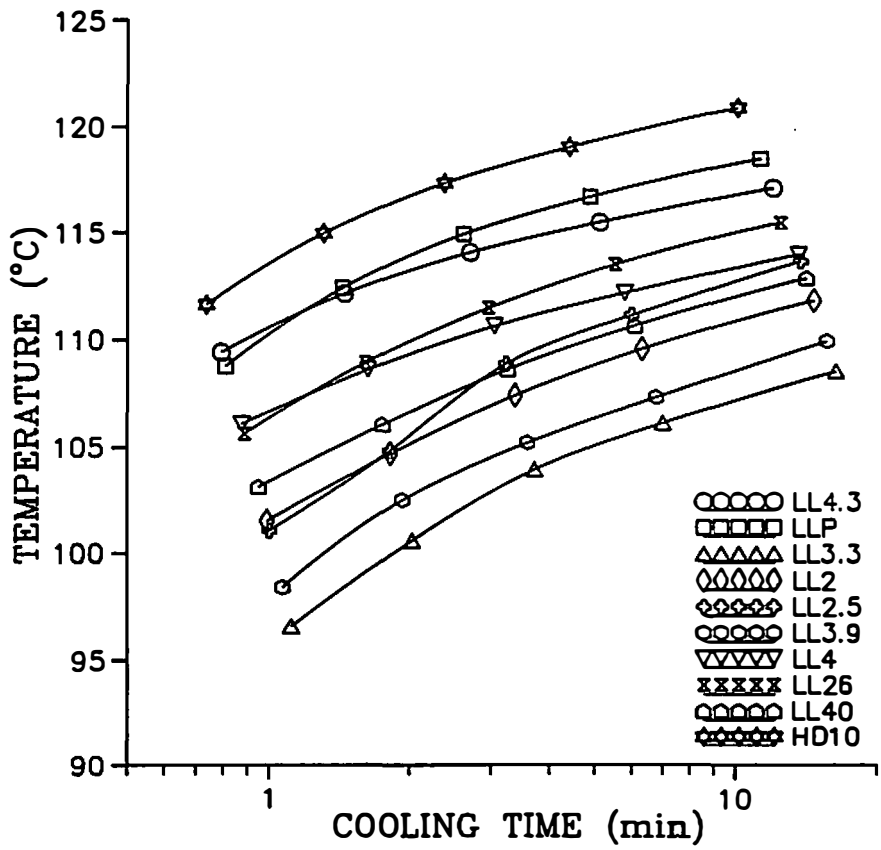

Figure 24. CCT curves for all resins.

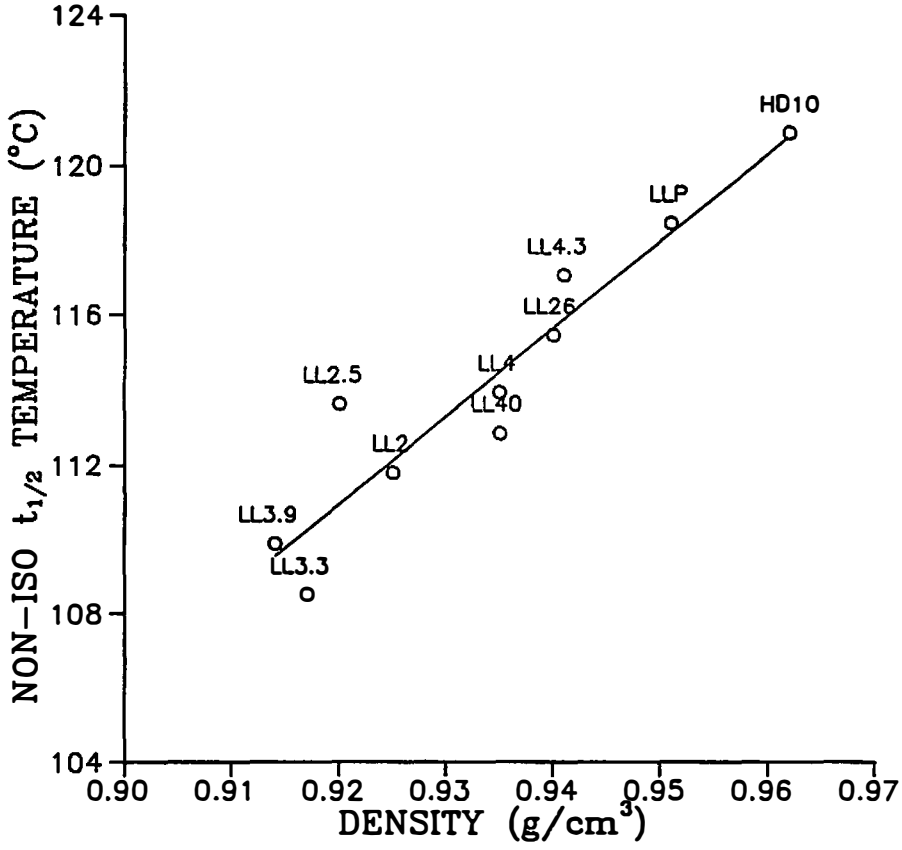

Figure 25. Half time temperature versus density.

Thus systems possessing greater disorder will experience a phase change at a lower temperature. This is in agreement with what has been observed in this work. Polymer samples which crystallize at lower temperatures are those possessing the most branching.

This half time temperature-density behavior is also observed at higher cooling rates. However at higher cooling rates, the non-isothermal crystallization curves begin to exhibit a greater retardation in crystallization rates at higher levels of crystallinity. This behavior is especially prominent in the resins which possess extensive short chain branches (broad ATREF curve). Figure 26 shows the non-isothermal crystallization curves for LL2.5. Note the significant tail associated with the higher cooling rate experiments. This prominent tail at higher cooling rates is present in all resins possessing broad ATREF curves.

Inspection of these ATREF curves, see Appendix A, reveals that a minimum separates a single peak at higher temperature from one or more peaks at a lower temperature. The molecules represented by the higher temperature peak would be responsible for the onset of crystallization and the initial level of crystallinity developed. As transformation progresses, the molecules with low levels of branching will crystallize from the melt to a much greater extent than the remaining highly branched molecules which will

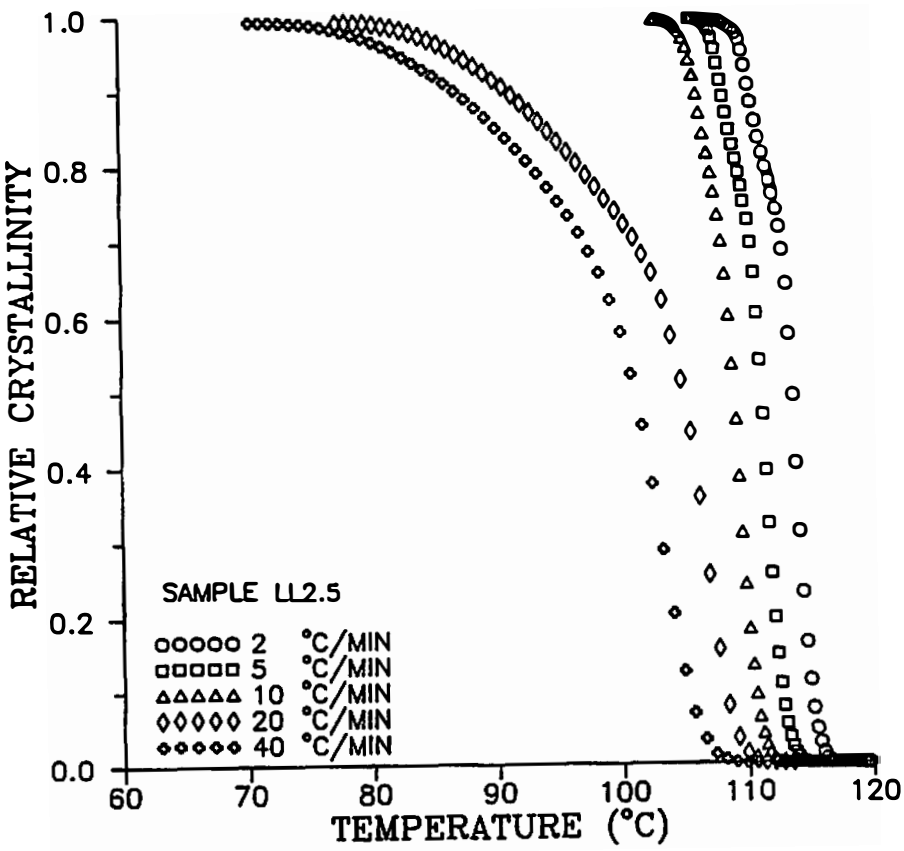

Figure 26. LL2.5 non-isothermal crystallization curves.

crystallize only at lower temperatures. These highly branched molecules will crystallize at a slower rate than those molecules with low levels of branching, thus the tail of the non-isothermal crystallization curve will lengthen. A broad ATREF resin could therefore be considered as a blend consisting of molecules having small degrees of branching and extensively branched molecules.

The crystallization behavior of these blends will be influenced by cooling rate. As the cooling rate increases less time is available for the molecules to preferentially crystallize according to degree of branching. The presence of the highly branched material will retard the crystallization rate of the whole and the tail will become more prominent.

The effect of cooling rate on the non-isothermal crystallization behavior of binary blends of linear polyethylenes has been studied by Smith and St. John-Manley [112]. They observed two types of crystallization which depended on cooling rate. At cooling rates less than 20 °C/min, separate crystallization of the components occurred and two SAXS peaks were present. The long periods corresponding to these peaks matched those of the pure fractions. At higher cooling rates, only one SAXS peak was observed which provided evidence that the blends co-crystallized. The SAXS peak present in the rapidly cooled sample corresponded to a long spacing intermediate in length between the long periods of the fractions present.

Non-isothermal Crystallization Modeling

Hammami [60] studied the modeling of non-isothermal crystallization using various models on polypropylene. He determined that the development of crystallinity was best described by the Nakamura et al. [58,59] formulation of non-isothermal crystallization kinetics

$$\frac{\Theta(T)}{\Theta(\infty)} = 1 - \exp\left[-\left(\int_0^t K(T)dt\right)^n\right] \qquad (2\text{-}20)$$

where n is an Avrami index which is not necessarily the same as that obtained from isothermal experiments. The Avrami index in equation (2-20) was assigned a value of 3. This is a reasonable assumption given the work of Mandelkern et al. [37]. Mandelkern and his associates studied the non-isothermal (quenched) supermolecular structure of branched polyethylenes. They observed that spherulitic structures existed within the range of branching and crystallization temperatures studied in this project.

The non-isothermal crystallization rate constant K is related to the isothermal crystallization rate constant k in the following form

$$K(T) = k(T)^{1/n} \qquad (4\text{-}17)$$

where n is the isothermal Avrami index. The isothermal crystallization rate constant is related to the half time in the following form

$$k = \frac{\ln(2)}{t_{1/2}^{n}} \qquad (2\text{-}27)$$

where the half time is related to temperature by the use of equation (2-26).

$$\frac{1}{t_{1/2}} = \left(\frac{1}{t_{1/2}}\right)_0 \exp\left[\frac{-U^*}{R(T-T_\infty)}\right]\exp\left[\frac{-C_3}{T\Delta T}\right] \qquad (2\text{-}26)$$

Combining the above three equations we have

$$K(T) = (\ln 2)^{1/n}\left(\frac{1}{t_{1/2}}\right)_0 \exp\left[\frac{-U^*}{R(T-T_\infty)}\right]\exp\left[\frac{-C_3}{T\Delta T}\right] \qquad (4\text{-}18)$$

Equations (2-20) and (4-18) were evaluated for each resin.

Figure 27 shows the non-isothermal predictions for LL40. The shape of the predicted crystallinity curves matches the experimental curves moderately well when relative crystallinity is less than 60%; however, the model underpredicts the required supercooling at all cooling rates. Hammami [60] studied the

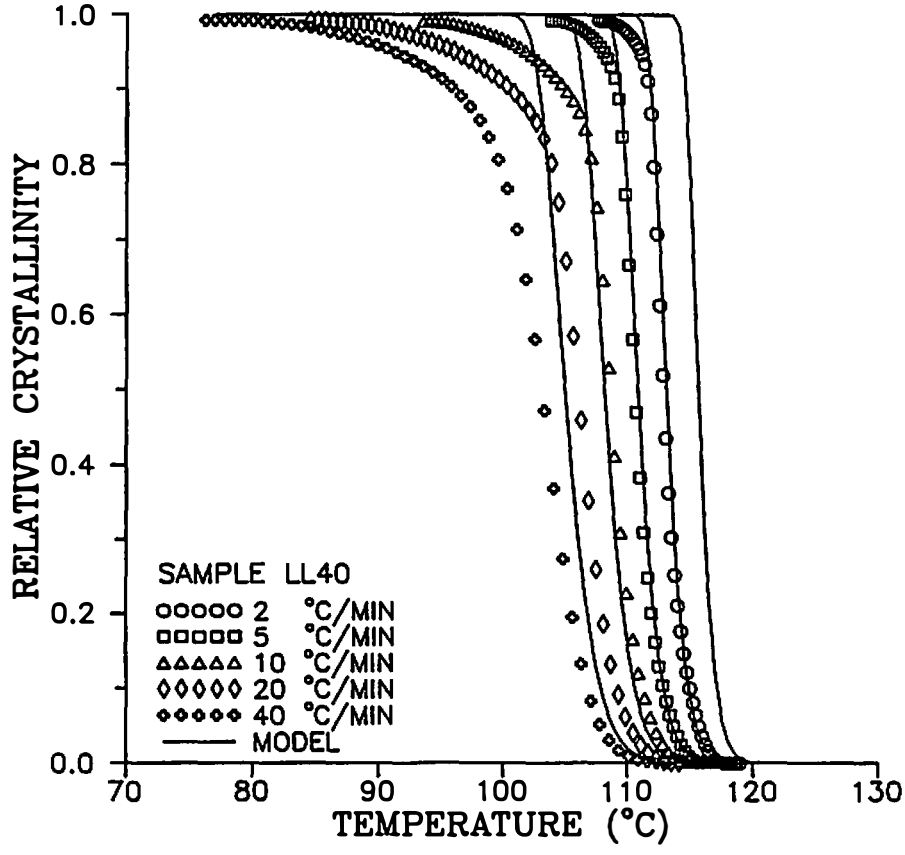

Figure 27. LL40 non-isothermal model predictions.

quiescent isothermal and non-isothermal crystallization behavior of polypropylene homopolymers and copolymers having low concentration of comonomer using depolarized light microscopy (DLM). He showed that predictions of non-isothermal crystallization behavior based on isothermal data were in fairly good agreement to experimentally obtained results. However in this study, predictions of non-isothermal crystallization behavior based on on isothermal data obtained by DLM were compared to non-isothermal crystallization data obtained by DSC. When experimental non-isothermal data obtained by both DSC and DLM were compared, the DLM curve occurred at a slightly higher temperature than the curve obtained from DSC and this difference decreased as cooling rate increased. This discrepancy will be examined in the future.

The presence of molecular fractionation may also influence the modeling predictions. Molecular fractionation involves the segregation and preferential crystallization of molecules and is present in polyethylene to a much greater extent than in polypropylene. Mandelkern [113] observed large differences in the isothermal crystallization rate of polyethylene as molecular weight varied. Hawkins and Smith [114] demonstrated that fractionation in polyethylene can occur due to differing degrees of branching. This may be especially prevalent in polydisperse randomly branched copolymers as the shorter molecules tend to possess more branches [32]. An uneven distribution of side

chains will create the possibility that parts of a chain can be incorporated into a lattice while other segments cannot [32].

The tendency of polyethylene to segregate upon crystallization may effect both the isothermal and non-isothermal crystallization kinetics. If the molecules with the least branching crystallize first then the onset of crystallization and initial levels of crystallinity will not be controlled by the bulk sample but chiefly by the fraction of molecules with the least branching. This behavior would result in an underprediction in the supercooling require for crystallization to occur. Mandelkern [94] studied isothermal crystallization behavior of LLDPE resins. He observed a lack of superposability in the crystallization isotherms for the LLDPE resins except at low levels of crystallinity. The superposability observed may be due to the crystallization of molecules having small amounts of branching which have segregated from the melt.

Inspection of Figure 27 also reveals that the model does not fit well in the tail region of the crystallization curve. The tail region is due to some type of secondary crystallization effect as has been discussed previously. Dietz [104] suggested the addition of an "attenuation-function"

$$h(X) = \exp\left[\frac{-aX}{1-X}\right] \qquad (4\text{-}13)$$

to the Avrami equation in order to deal with the effects of

secondary crystallization. Hammami [60] has used equation (4-13) to correct for some of the effects of secondary crystallization in non-isothermally crystallized polypropylene. The use of equation (4-13) for polyethylene will be explored in the future.

The model predictions shown in Figure 27 are not typical. Figure 28 displays the model predictions for LL4. The model seriously overpredicts the supercooling required for crystallization. This behavior is also observed in the LL2, LL3.3, and LL3.9 resins. Nakamura's model assumes that the crystallization kinetic coefficients are obtained from superposable isotherms [104]. Inspection of Appendix B reveals that these resins have isotherms which are not superposable. The isothermal modeling of these resins was reasonably successful. The non-isothermal modeling of the resins which have superposable isotherms was also successful. Therefore the large error observed between the predicted and experimental non-isothermal crystallization data must be due to the choice of parameters supplied to the model.

Non-linear Non-isothermal Regression

As one of the main goals of this project was to understand non-isothermal stress enhanced crystallization, it was decided to use non-linear regression to fit the non-isothermal data to Nakamura's model equation (2-20). For this purpose it was necessary to modify equation (4-18)

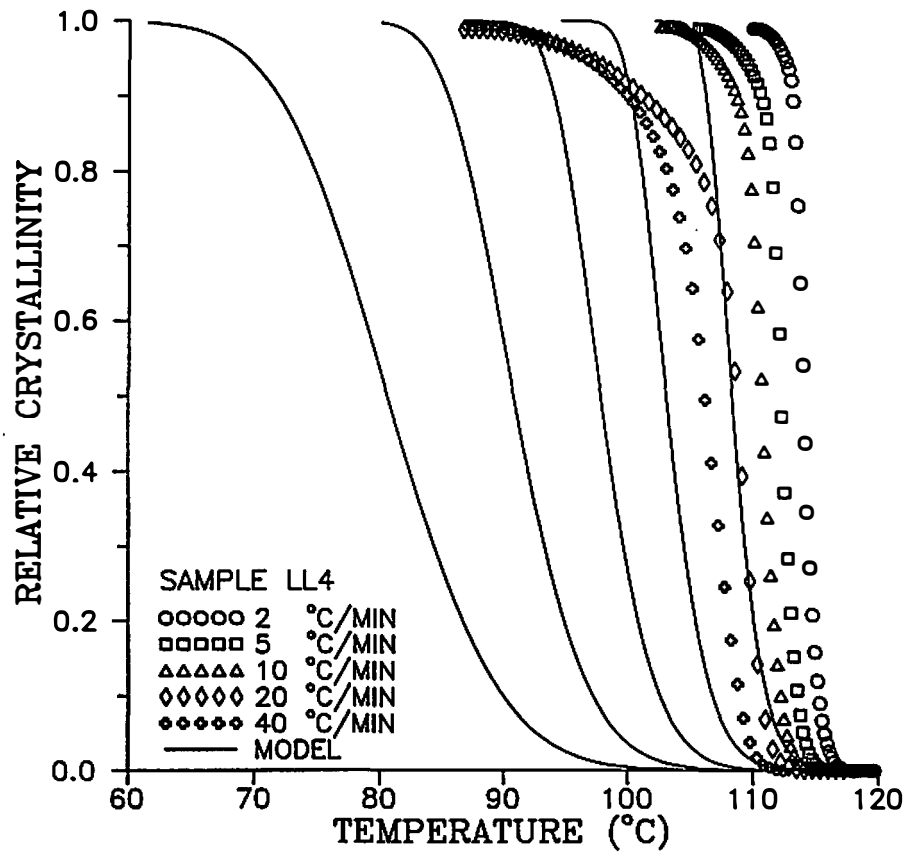

Figure 28. LL4 non-isothermal model predictions.

$$K(T) = (\ln 2)^{1/n}\left(\frac{1}{t_{1/2}}\right)_0 \exp\left[\frac{-U^*}{R(T-T_\infty)}\right]\exp\left[\frac{-C_3}{T\Delta T}\right] \qquad (4\text{-}18)$$

slightly because the isothermal Avrami index cannot be determined from non-isothermal experiments. The new non-isothermal crystallization rate equation becomes

$$K(T) = K_0\exp\left[\frac{-U^*}{R(T-T_\infty)}\right]\exp\left[\frac{-C_3}{T\Delta T}\right] \qquad (4\text{-}19)$$

where $K_0 = (\ln 2)^{1/n}(1/t_{1/2})_0$.

The Marquardt method [115] was used to determine the fitting coefficients K_0 and C_3. This is an iterative method in which an initial guess of K_0 and C_3 is used to estimate new values of K_0 and C_3 such that the residuals are minimized. These values are reported in Table 8. The range of relative crystallinity used for the regression was 0 to 60%. In this regression method, different choices of K_0 and C_3 can produce similar predictions, and so no physical significance should be attributed to the values obtained.

Table 8. Non-linear Regression Crystallization Coefficients

Sample	ln K_0 $ln(s^{-n})$	$C_3 \times 10^{-3}$ (K^2)
LL2	9.91	112
LL2.5	7.89	85
LL3.3	9.88	124
LL3.9	9.82	119
LLP	7.69	68
LL4	12.6	131
LL4.3	10.1	93
LL26	9.59	97
LL40	10.9	120
HD10	7.71	62

The non-isothermal crystallization behavior for LL4 as predicted by equation (4-19) is shown in Figure 29. The fits are quite good for the early part of the crystallization curve, but equation (4-19) is incapable of describing the latter portion of the crystallization curve. This is not surprizing due to the complications in the crystallization process during the latter region, as previously discussed. Non-linear regression fits for the other resins are found in Appendix D.

4.3 Melt Spinning Studies

The series of melt spinning experiments that were completed are summarized in Table 9. At spinning speeds higher than those used the spinline would break frequently. The breaks would occur near the spinneret. The fiber length would recoil a few centimeters after the break. This recoil is consistent with fluids possessing elastic properties. This lack of spinnability in the upper (molten) region of the spinline is due to cohesive fracture [55]. According to the theory of cohesive fracture, spinnability is controlled by the relaxation time of the material, its tensile (melt) strength, and the deformation conditions. The relaxation times are very sensitive to temperature and molecular structure. Relaxation times greater than one second have been reported for high molecular weight polyolefins [55].

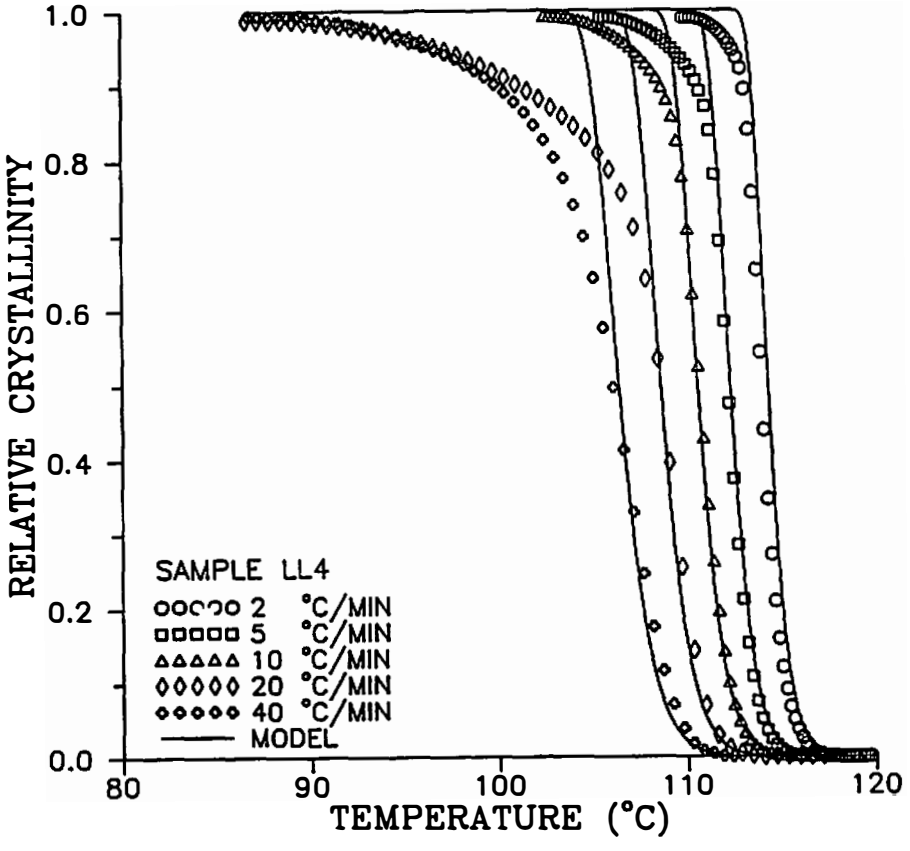

Figure 29. Non-linear non-isothermal model predictions for LL4.

Table 9. Summary of Melt Spinning Experiments

Resin	Mass Flow Rate (g/min)	Terminal Velocity (m/min)
LL3.9	1.25	62
LL3.9	1.25	190
LL3.9	2.00	66
LL3.9	2.00	262
LLP	1.25	65
LLP	1.25	152
LLP	2.01	85
LL4.3	1.25	57
LL4.3	1.25	214
LL4.3	2.00	57
LL4.3	2.01	173

For all experiments the spinline length was 2.5 m and the die diameter was 813 μm.

The extrusion temperature used was 215 °C. Slight melt fracture was present in the LLP and LL4.3 resins. Melt fracture is thought to be due to elastic effects. Several workers [115-118] have suggested that a distorted extrudate will occur when a critical amount of elastic strain energy is exceeded. The excess elastic strain energy may be converted into surface free energy, thereby yielding a distorted extrudate. Melt fracture was more severe at lower temperatures while at higher temperatures, the fiber would break more readily. Also at 230 °C, these polymers are susceptible to oxidation. The LL3.9 resin did not exhibit melt fracture at either 185 °C or 215 °C, although at higher melt flow rates, melt fracture was observed.

On-line Diameter Measurements

Figure 30 compares the diameter profiles of the three Dow LLDPE's at a mass flow rate of 1.25 g/min and a final velocity ≈ 60 m/min. Notice that the initial drawdown profiles are quite similar until spinline distance exceeds 30 cm. Beyond 30 cm, the drawdown rate differs for the resins. The LL3.9 resin has the lowest melt index (MI) and reaches final diameter further from the spinneret than the other resins. The LLP resin reached its final drawdown closer to the spinneret than the other resins. It has been discussed in previous chapters that ethylene-propylene copolymers (such as LLP) can crystallize in a manner similar to a high density polyethylene due to the relative ease at which methyl

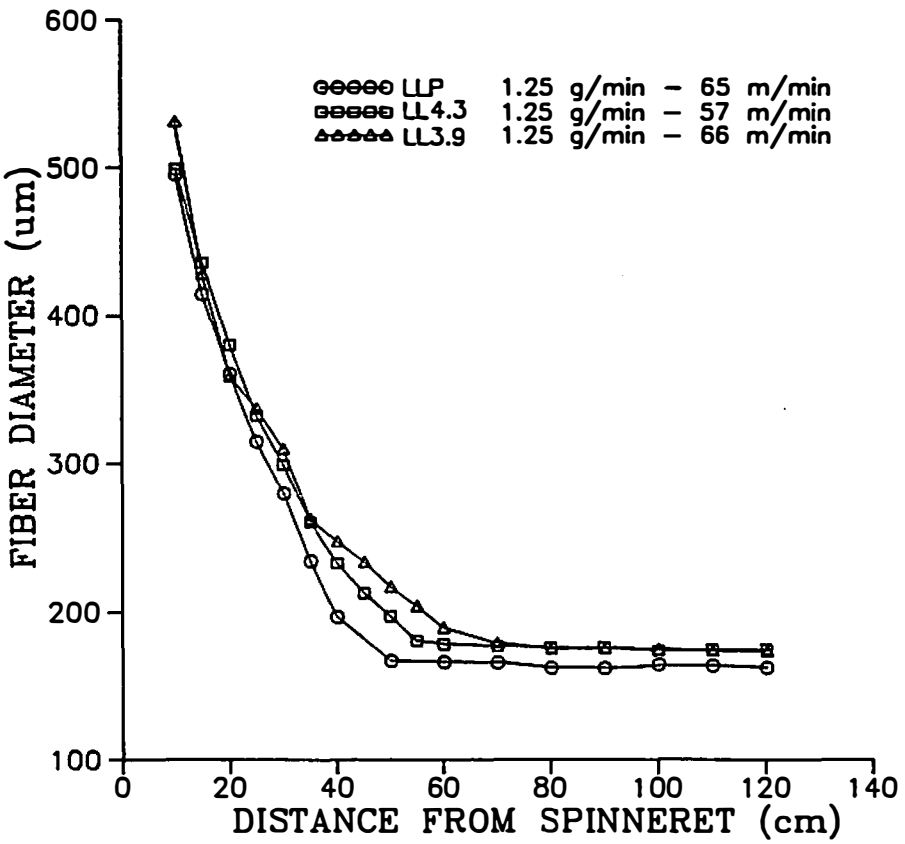

Figure 30. Diameter profiles of LL3.9, LLP, and LL4.3 at 1.25 g/min.

side groups are incorporated into a crystal lattice. Melt spinning studies on LL4, LL26, LL40, and HD10 by Lambach [8] have demonstrated that HD10 reaches it final drawdown diameter before LL4, LL26, or LL40. These diameter results would seem to indicate that LLP may possess spinline behavior similar to a high density polyethylene. Complete diameter drawdown profiles are found in the Appendix E.

On-line Temperature Measurements

Experimental on-line temperature profiles for LL4.3 are found in Figure 31. Inspection of this figure reveals that mass flow rate has a marked effect on temperature profile. For a given mass flow rate, the fiber temperature in the upper part of the spinline is essentially a function of position, not spinning speed. This behavior is present in the other resins and has been reported before [4,5,8-11]. Temperature profiles for LL3.9, LLP, and LL4.3 are compared in Figure 32. Notice from Figure 32 that fiber temperature is quite similar for the resins until the crystallization region is approached. Once crystallization begins to occur, the profiles are markedly different. The LLP fiber temperature increases in the crystallization region. The LL4.3 fiber temperature plateaus over a 45 cm range. A plateau also exists for the LL3.9 resin but at a temperature lower than the other resins. These temperature plateaus are caused by the heat of fusion being released from the crystallizing fiber. Temperature plateaus have

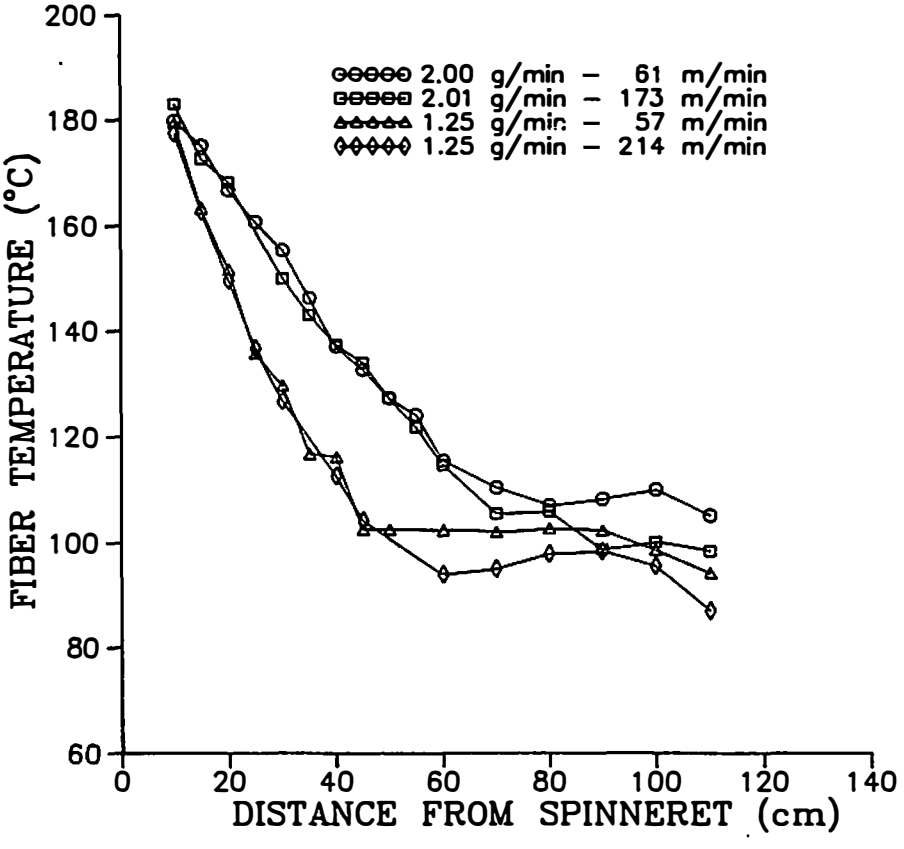

Figure 31. LL4.3 temperature profiles.

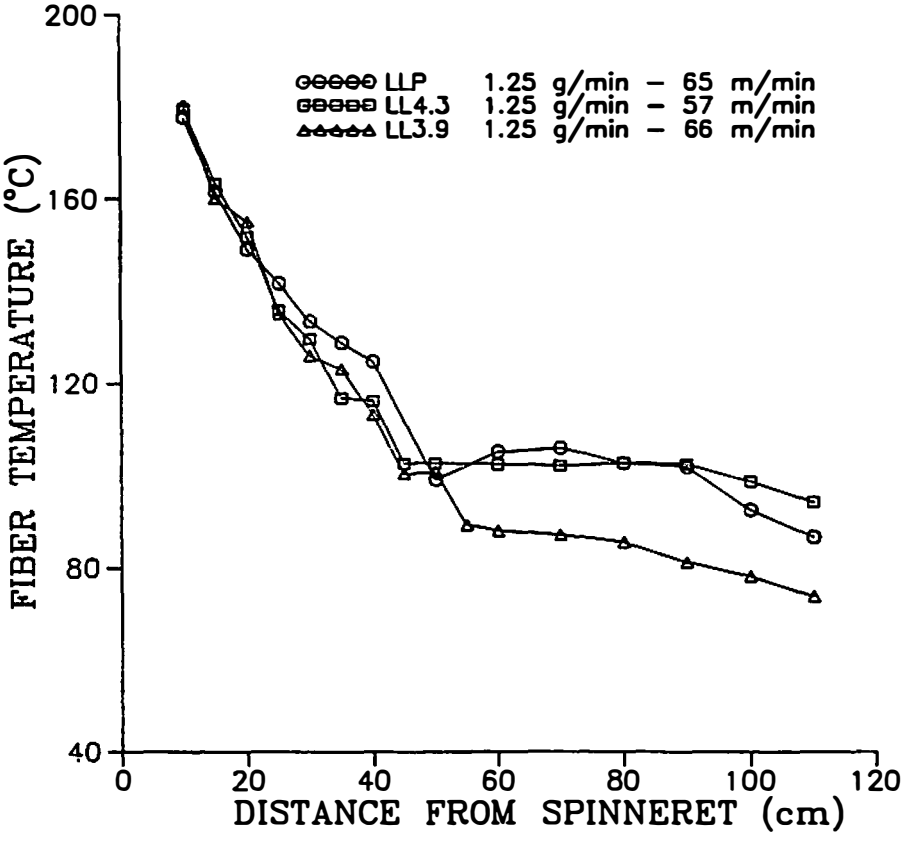

Figure 32. LL3.9, LLP, and LL4.3 temperature profiles.

been reported by other researchers studying polyethylene [6,8,83].

The amount of heat released during crystallization is proportional to the amount of crystallinity present. The sample with the highest crystallinity (LLP) shows an increase in temperature during crystallization. Resin LL4.3 has less crystallinity and displays a flat temperature plateau. Resin LL3.9 has much less crystallinity and displays a less well defined plateau at a somewhat lower temperature.

These observations are in agreement with the relative non-isothermal crystallization rates. Resin LLP has the highest crystallization rate and it shows an increase in temperature in the plateau region. Resin LL4.3 has a crystallization rate which is similar to LLP. The temperature plateau associated with LL4.3 occurs at a temperature which is similar to that of LLP. Resin LL3.9 has a crystallization rate which is much lower than LLP or LL4.3. LL3.9's plateau occurs at a lower temperature than the other resins. A complete set of temperature profiles is found in Appendix E.

On-line Birefringence Measurements

The experimental on-line birefringence profiles for LL4.3 are shown in Figure 33. For this resin, the initial appearance of birefringence is related to spinning speed (stress) and mass throughput rate. At a given mass flow rate, the higher the spinning velocity, the sooner initial birefringence is observed. For

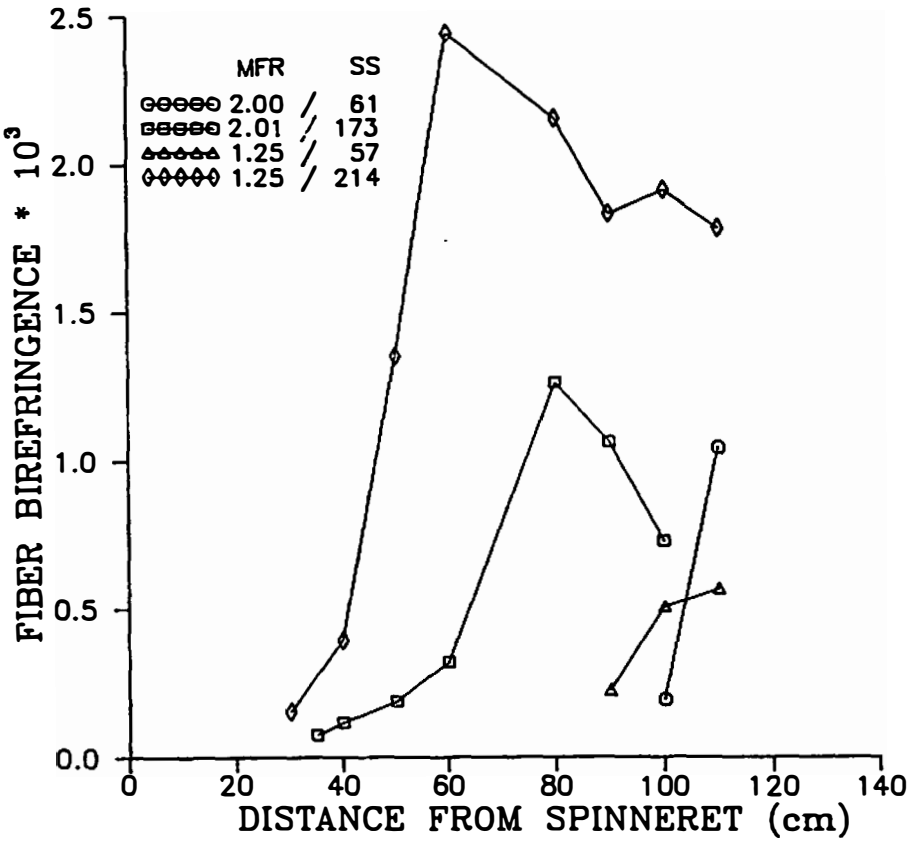

Figure 33. LL4.3 birefringence profiles.

the higher speed runs, the birefringence would reach a maximum and then decrease. This decrease in birefringence is believed to be due to a reduction in fiber transparency as crystallization progresses. No terminal as-spun birefringence could be measured for these samples due to fiber opacity.

A decrease in on-line birefringence has been reported before. Katayama et al. [69] studied melt spinning of HDPE. They observed a complex birefringence profile which was attributed to a complex crystallization scheme. The birefringence would pass through a maximum then a minimum then another maximum, eventually reaching some saturation value. They obtained on-line WAXS and SAXS patterns and reported c-axis inclination values of ϕ = 40 to 60° away from the fiber axis. The authors considered that a radial temperature gradient across the fiber would cause the surface of the fiber to crystallize first. This in turn concentrates the tension at the surface and would orient the c-axis of the crystallites almost parallel to the fiber axis. As transformation progressed, the core of the fiber began to crystallize resulting in a wider distribution of the tension. This decrease in tension will cause the core of the fiber to crystallize under less stress and therefore less orientation. Lambach [8] also observed complex birefringence profiles in LL4 and HD10.

The on-line experimental birefringence profiles for LL3.9 are found on Figure 34. An important feature observed is that the lower speed runs show a rapid increase in birefringence while the

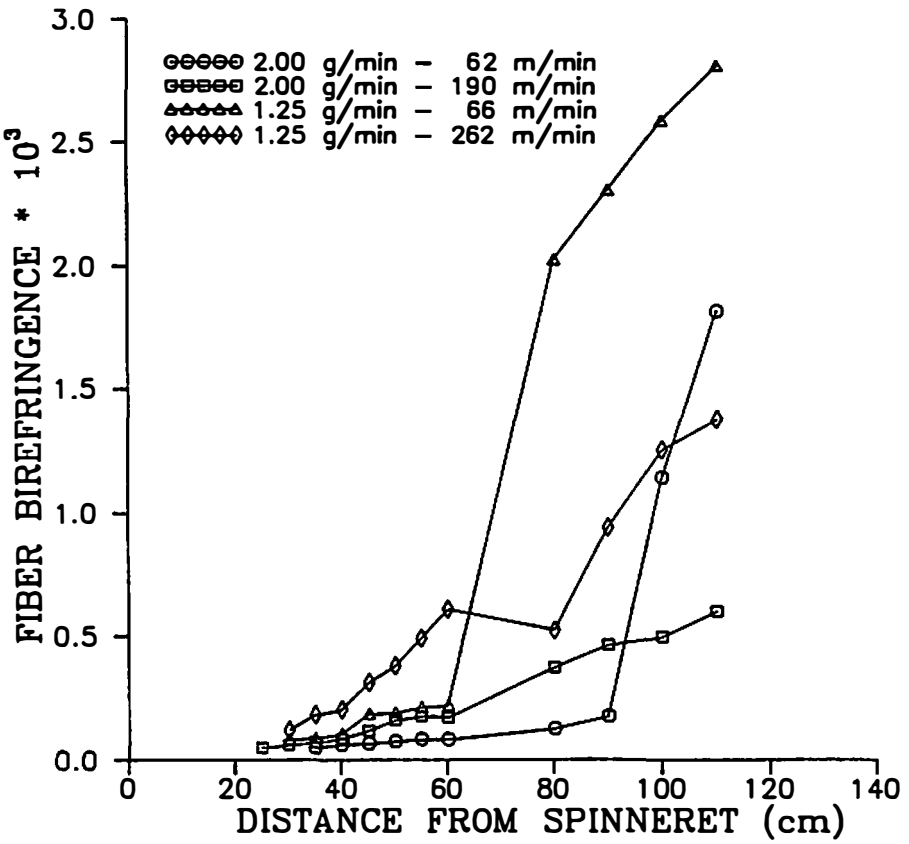

Figure 34. LL3.9 birefringence profiles.

higher speed (stress) runs do not. This provides evidence that the effect of cooling rate is greater than the effect of stress in enhancing crystallization kinetics for these spinning conditions. The final birefringence values could be measured and are reported in Table 10. The final birefringence values were higher for the higher speed than for the lower speed runs. Thus the rapid rise in birefringence exhibited by the low speed runs occurs farther down the spinline when spinning speed (stress) increases. It would appear that these spinning conditions represent a critical region. At low speed, crystallization readily occurs closer to the spinneret and at higher temperatures. At high spinning speed (high stress) the effect of heat transfer to the air is greater and crystallization is forced to occur at lower temperatures and hence farther from the spinneret. However these temperatures are not so low as to prevent the molecular alignment needed to obtain the large as-spun birefringence values observed. The mass flow rate also effects the development of birefringence. As mass flow rate decreases at a given spinning velocity, the stress increases. This was shown above to strongly influence the on-line birefringence profile.

The diameter, temperature, and birefringence are dynamic interacting variables. In Figure 35 these variables for LL3.9 at 1.25 g/min and 66 m/min have been plotted on the same normalized scale. Notice that the onset of birefringence occurs where the temperature plateau has begun. The diameter profile is

Table 10. Terminal As-spun Birefringence Values for LL3.9

Mass Flow Rate (g/min)	Spinning Speed (m/min)	Stress $\times 10^{-5}$ (dyne/cm^2)	$\Delta n \times 10^{-3}$
1.25	66	17.4	3.6
1.25	262	84.4	16.1
2.00	62	7.0	2.7
2.00	190	43.7	8.8

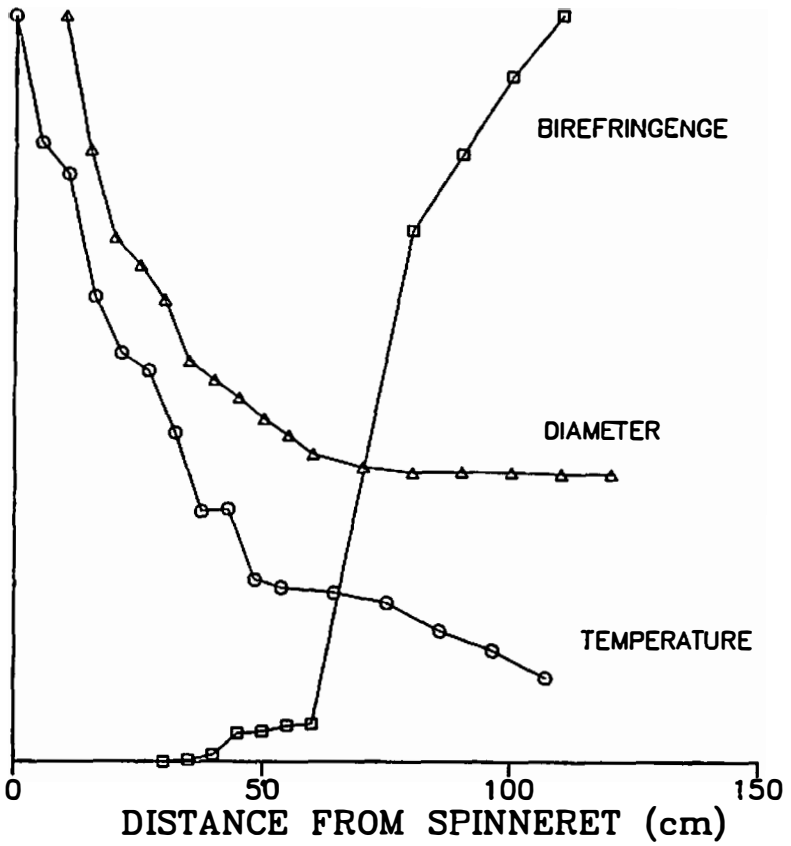

Figure 35. Normalized diameter, temperature, and birefringence profiles for LL3.9 at 1.25 g/min and 66 m/min.

also nearing its final diameter in this region.

On-line Tension Measurements

Fiber tension data were collected at a distance of 120 cm from the spinneret. The stress was determined by dividing tension by the fiber cross-sectional area at that 120 cm from the spinneret. The experimental fiber tension and stress are reported in Table 11. The fiber stress values for the 1.25 g/min runs are plotted in Figure 36. Inspection of Figure 36 reveals that stress increases as fiber velocity increases. It is also apparent that at a given velocity, stress increases as melt index decreases. This observation may be explained by examining the forces which contribute to the overall force balance. For the low speed spinning range studied, the force balance may be written as [70]

$$F_{rheo} \approx F_{grav} + F_{ext} \qquad (2\text{-}41)$$

where F_{rheo} is the rheological force in the fiber, F_{ext} is the external take-up tension, and F_{grav} is the gravitational force on the fiber. As the diameter profiles and mass throughputs are similar for the samples, F_{grav} must be similar. Therefore the difference in fiber stress between the resins at a given terminal velocity must be due to different rheological properties between the samples.

Table 11. Experimental Tension and Stress Values

Resin	Mass Flow Rate (g/min)	Spinning Speed (m/min)	Tension (dyne)	Stress $\times 10^{-5}$ (dyne/cm^2)
LL3.9	1.25	66	472	17.4
LL3.9	1.25	262	574	84.4
LL3.9	2.00	62	262	7.0
LL3.9	2.00	190	650	43.7
LLP	1.25	65	121	4.6
LLP	1.25	152	453	40.1
LLP	2.01	85	57	1.8
LL4.3	1.25	57	131	4.2
LL4.3	1.25	214	427	52.6
LL4.3	2.00	61	*	-
LL4.3	2.01	173	407	25.1

* Malfunction of equipment prevented this measurement from being correctly completed.

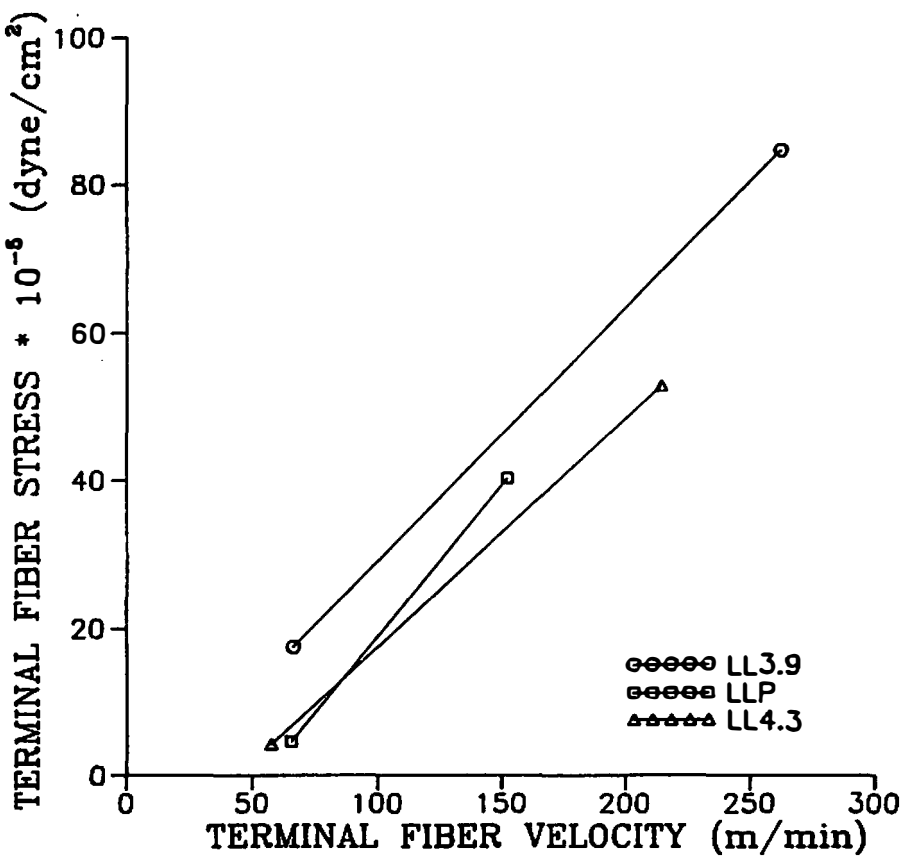

Figure 36. Fiber stress versus fiber velocity.

Crystallinity

The crystallinity of the as-spun fibers as determined by DGC are reported in Table 12. These crystallinities are from 8 to 10% less than the unprocessed resin crystallinities. The as-spun crystallinities are essentially constant for the different spinning conditions indicating that the processing effects which caused the reduction in crystallinity have reached a saturation level for these spinning conditions. Dees [7] studied low speed melt spinning of HDPE. He observed a reduction in as-spun crystallinity as fibervelocity increased from 50 - 400 m/min, but above 400 m/min no further reduction in crystallinity occurred. Lambach [8] reported that as-spun fiber crystallinity reached saturation level at speeds exceeding 500 m/min in his melt spinning studies of LL4, LL26, LL40, and HD10.

Wide Angle X-ray Scattering

The WAXS patterns of the as-spun fibers are shown in Figures 37 through 39. The fiber axis direction is parallel to the long dimension of the page. The fiber stress is indicated below each pattern. The two principal reflections are (110) and (200). The distribution of intensity in these reflections changed according to the spinning conditions. Figure 37 shows WAXS patterns for the LL4.3 resin. Notice that for the (110) reflections, the highest intensities are centered 30° from the equator in all LL4.3 WAXS

Table 12. Crystallinity of Melt Spun Fibers

Resin	Mass Flow Rate (g/min)	Terminal Velocity (m/min)	Crystallinity
LL3.9	1.25	62	0.369
LL3.9	1.25	190	0.369
LL3.9	2.00	66	0.369
LL3.9	2.00	262	0.377
LLP	1.25	65	0.626
LLP	1.25	152	0.626
LLP	2.01	85	0.619
LL4.3	1.25	57	0.562
LL4.3	1.25	214	0.555
LL4.3	2.00	57	0.562
LL4.3	2.01	173	0.555

A

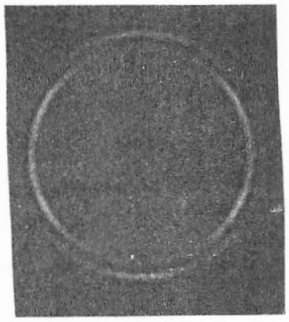

2.00 g/min - 62 m/min
-

B

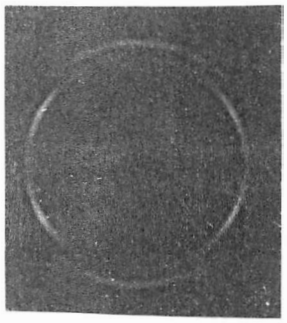

2.01 g/min - 173 m/min
$\sigma = 25.1 \times 10^5$ dyne/cm^2

C

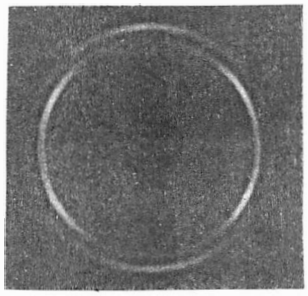

1.25 g/min - 57 m/min
$\sigma = 4.2 \times 10^5$ dyne/cm^2

D

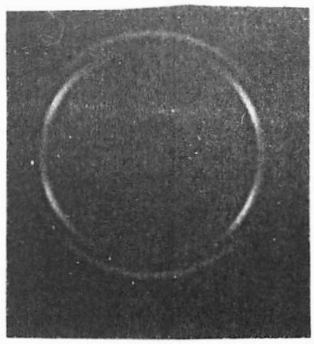

1.25 g/min - 214 m/min
$\sigma = 52.6 \times 10^5$ dyne/cm^2

Figure 37. LL4.3 WAXS patterns

A

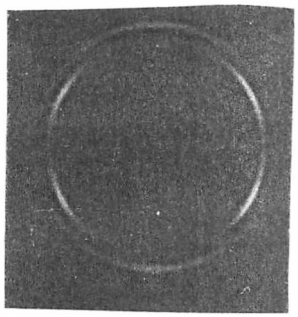

2.01 g/min - 85 m/min
$\sigma = 1.8 \times 10^5$ dyne/cm^2

B

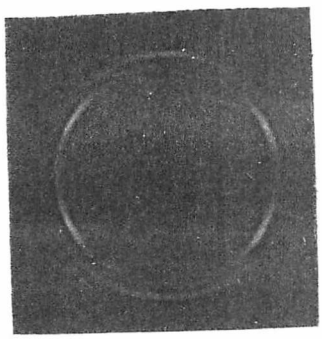

1.25 g/min - 65 m/min
$\sigma = 4.6 \times 10^5$ dyne/cm^2

C

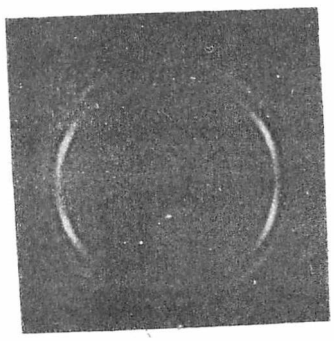

1.25 g/min - 152 m/min
$\sigma = 40.1 \times 10^5$ dyne/cm^2

Figure 38. LLP WAXS patterns.

A

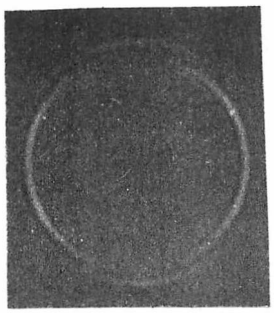

2.00 g/min - 62 m/min
$\sigma = 7.0 \times 10^5$ dyne/cm^2

B

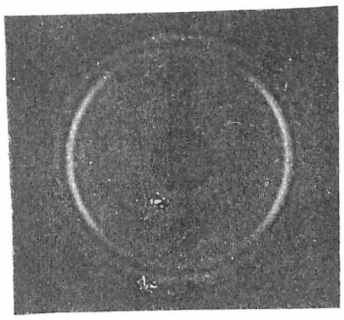

2.00 g/min - 190 m/min
$\sigma = 43.7 \times 10^5$ dyne/cm^2

C

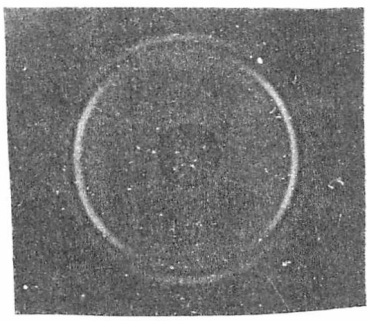

1.25 g/min - 66 m/min
$\sigma = 17.4 \times 10^5$ dyne/cm^2

D

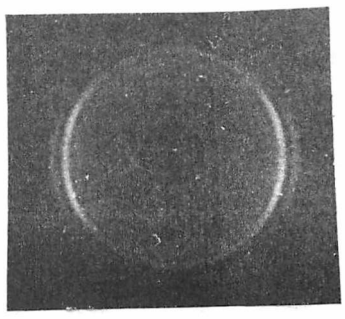

1.25 g/min - 262 m/min
$\sigma = 84.4 \times 10^5$ dyne/cm^2

Figure 39. LL3.9 WAXS patterns.

patterns. These patterns are better defined at higher speed (stress). The (200) reflection is present as an axially centered pattern.

Figure 38 show WAXS patterns for the LLP resin. The (110) reflection is quite distinct and is centered 30° from the equator in the low speed run. At the higher speed run, Figure 38C, these intensities have moved to 20° from the equator. For the low speed runs, Figures 38A and 38B, the (200) reflection is comprised of two arcs centered axially.

Figure 39 shows WAXS patterns for the LL3.9 resin. At low spinning speeds, the (110) reflection is composed of two broad arcs centered at the equator. As speed increases, the intensity of the (110) reflection increases at the equator. The (200) reflection is centered axially in Figures 39A through 39C. However for the high speed run, Figure 39D, the (200) reflection is centered at the equator, indicating that this run has developed considerably more orientation than the others.

Lambach performed extensive orientation analysis on LL4, LL26, LL40, and HD10. He observed that the preferential alignment of the crystalline growth front was perpendicular to the fiber axis. The low viscosity resins (LL26 and LL40) showed little change in orientation until the spinning speed exceeded 1000 m/min. The LL4 and HD10 resins showed an increase in orientation with each increase in spinning speed. Based on his orientation work, Lambach postulated that the orientation

developed in the LL26 and LL40 resins was due mainly to radial temperature differences except at the highest speeds. The LL4 and HD10 resins showed an increase in orientation even at the lowest speeds.

The WAXS patterns obtained in this study show the same features as did the patterns obtained by Lambach at much higher speeds. This indicates that these LLDPE's all develop the same low orientation until sufficient spinning speed (stress) is present. Based on Figure 39D, it would appear that the LL3.9 resin develops significant orientation at speeds far less than an HDPE with a similar WAXS pattern. The WAXS patterns for LLP and LL4.3 show only slight changes as spinning speed increases. The range of spinning conditions used was limited and therefore a definite conclusion cannot be made as to whether orientation will be controlled by spinning speed or radial temperature gradients based on the WAXS patterns.

Continuous Cooling Transformation Analysis

Cooling rate and stress are important factors which influence melt spinning crystallization kinetics. The relative affects of these factors may be understood by the use of Spruiell and White's continuous cooling transformation (CCT) approach [12]. The CCT approach permits both quiescently cooled crystallization and melt spinning crystallization behavior to be displayed on the same cooling time versus crystallization temperature plot.

The quiescently cooled crystallization behavior was obtained by DSC. Cooling rates were 2, 5, 10, 20, and 40 °C/min. The onset of crystallinity was chosen as the temperature at which 10% relative crystallinity was present. The cooling time required is given by

$$\text{Cooling Time} = \frac{T_m^o - T(\Theta(T)/\Theta(\infty)=0.1)}{\text{Cooling Rate}} \qquad (4\text{-}20)$$

For quiescent cooling modeling, the following equations were used

$$\frac{\Theta(T)}{\Theta(\infty)} = 1 - \exp\left[-\left(\int_0^t K(T)dt\right)^n\right] \qquad (2\text{-}20)$$

where
$$K(T) = K_0 \exp\left[\frac{-U^*}{R(T-T_\infty)}\right]\exp\left[\frac{-C_3}{T\Delta T}\right] \qquad (4\text{-}19)$$

and n is assigned the value of 3. The onset of crystallization was chosen as the temperature at which 10% relative crystallinity was present. The required cooling time is given by equation (4-20).

For the melt spinning experiments, a rapid rise in birefringence and/or the presence of a temperature plateau were used to determine onset temperatures. Due to a variable cooling

rate, equation (4-20) cannot be used to determine cooling times. However this information can be extracted from experimental diameter and temperature profiles.

In Figures 40 through 42, melt spinning and quiescently cooled CCT data are presented. The solid line represents quiescent non-isothermal crystallization modeling to provide an extrapolation to high cooling rates. Notice that this line curves downward as lower crystallization onset temperatures are approached. This is due to a reduction in molecular mobility as temperature decreases.

Observe that none of the experimental melt spinning points occur near the quiescently cooled modeling predictions. Each of these points is at a different cooling rate and stress. This indicates that stress does influence spinline crystallization of LL3.9, LLP, and LL4.3. The stress measured at 120 cm from the spinneret is shown in the legend. Inspection of Figures 40 - 42 also reveal that generally an increase in stress (spinning velocity) reduces the temperature at which crystallization begins. However in the present case the increased stress is accompanied by increased cooling rates. Therefore for the spinning conditions used, the increase of cooling rate produces greater supercooling faster than stress enhancement of crystallization kinetics can increase the crystallization temperature. Previous experience has shown that this is not always the case. This observation may indicate that the effect of stress on crystallization rates may saturate rather quickly

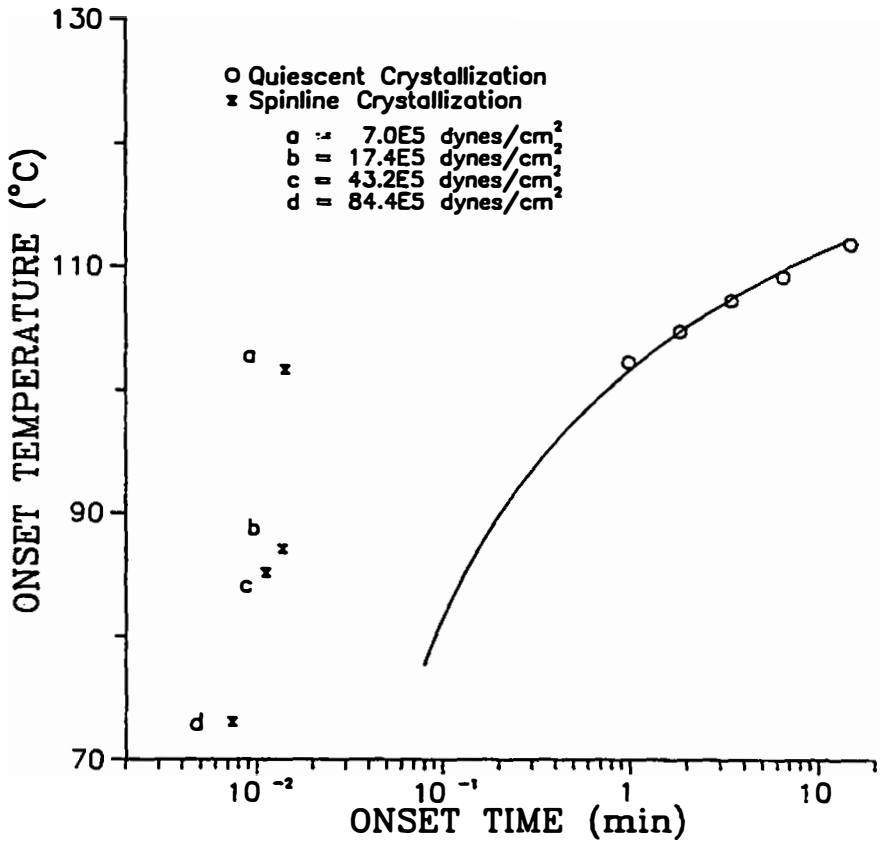

Figure 40. LL3.9 CCT analysis.

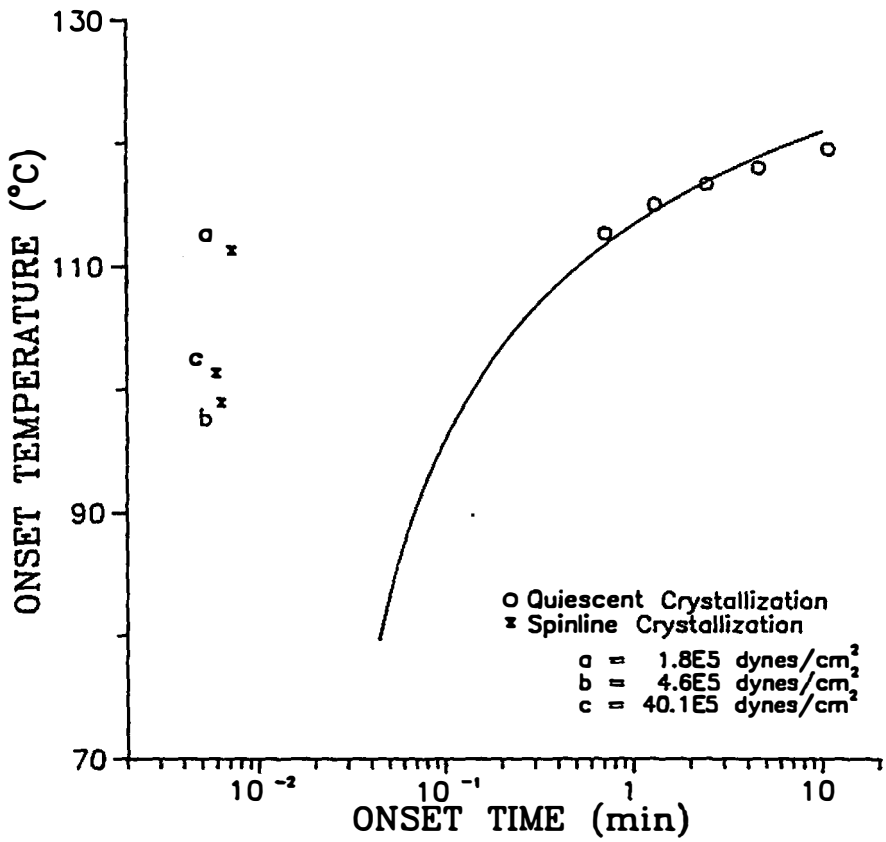

Figure 41. LLP CCT analysis.

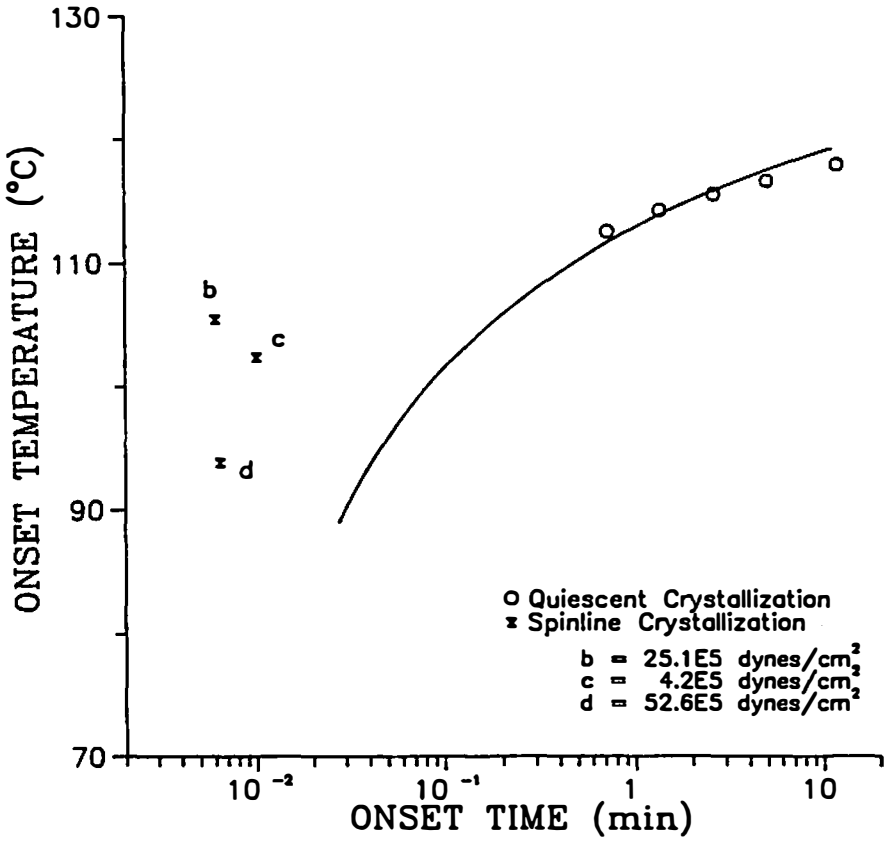

Figure 42. LL4.3 CCT analysis.

for polyethylenes. A comparison of stress-enhanced crystallization rates as influenced by branching was inconclusive due to the presence of both a changing cooling rate and stress.

At this point it is helpful to review the CCT data obtained by Lambach [8] for LL4, LL26, LL40, and HD10. In Figures 43 through 46, the melt spinning CCT data obtained by Lambach is plotted along with quiescently cooled CCT data obtained in this study. Equations (2-20) and (5-8) were used to generate the model extrapolations. The fiber stresses listed in the legend represent the predicted stress at the spinline position where crystallization occurs.

Lambach reported negligible enhancement of crystallization due to stress for samples LL26 and LL40. However this conclusion was based on the predictions of Ziabicki's [55] empirical non-isothermal crystallization kinetic equation

$$K(T) = k_{max}\exp\left[\frac{-4\ln(2)(T-T_{max})^2}{D^2}\right] \qquad (2\text{-}24)$$

which cannot predict the rapid decrease in onset temperature at rapid cooling rates. Inspection of Figures 43 through 46 reveal that stress does effect the crystallization of LL26 and LL40. For the LL4 and HD10 resins, stress is observed to be an important factor. Crystallization onset temperatures are considerably higher than would be expected in the absence of stress. However it must be realized that due to inoperative temperature measurement

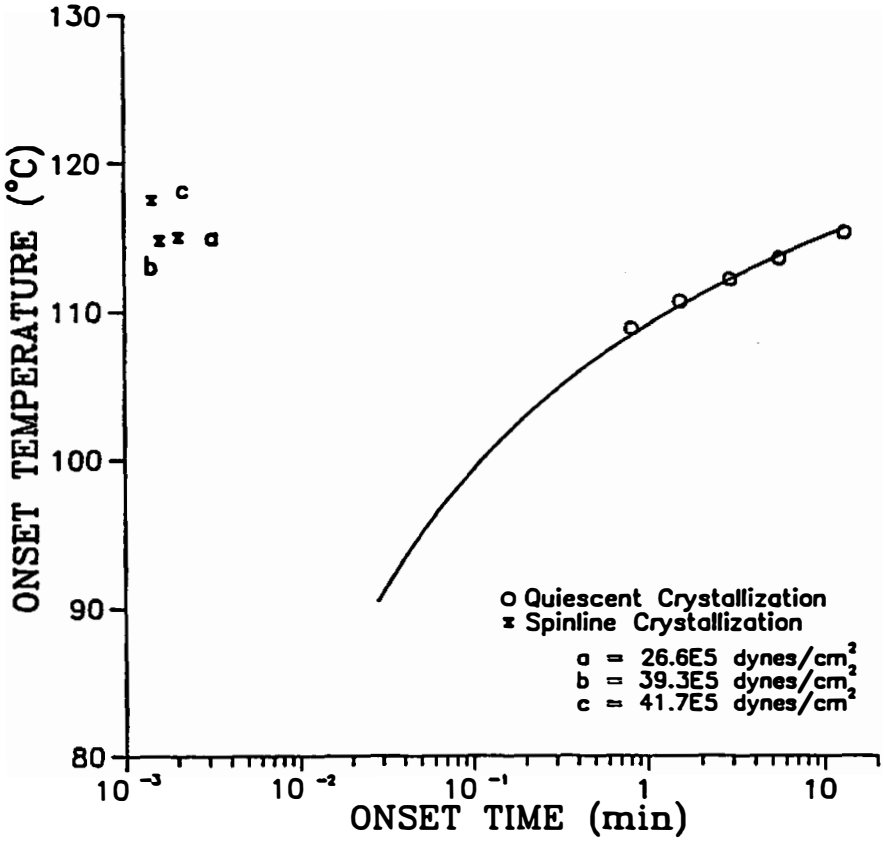

Figure 43. LL4 CCT analysis.

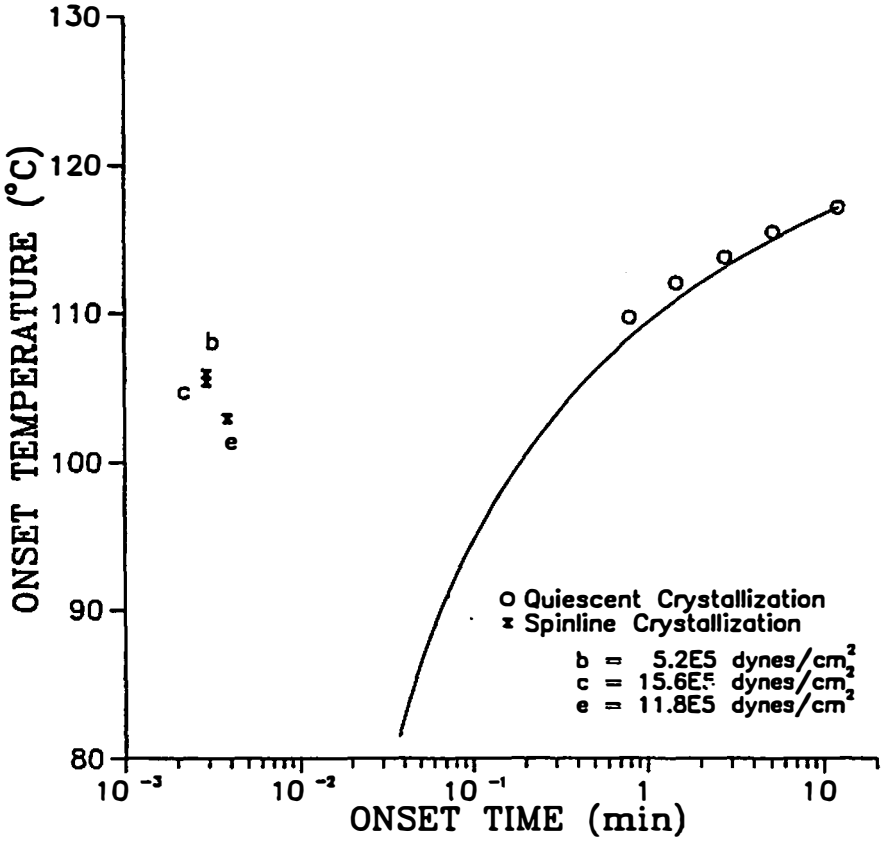

Figure 44. LL26 CCT analysis.

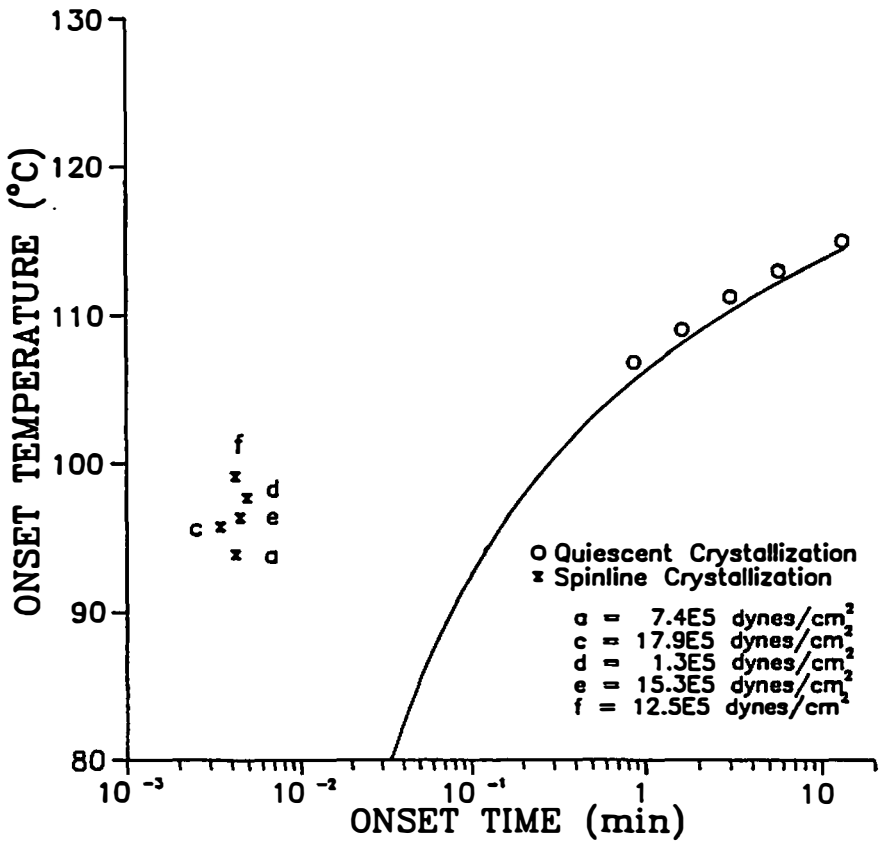

Figure 45. LL40 CCT analysis.

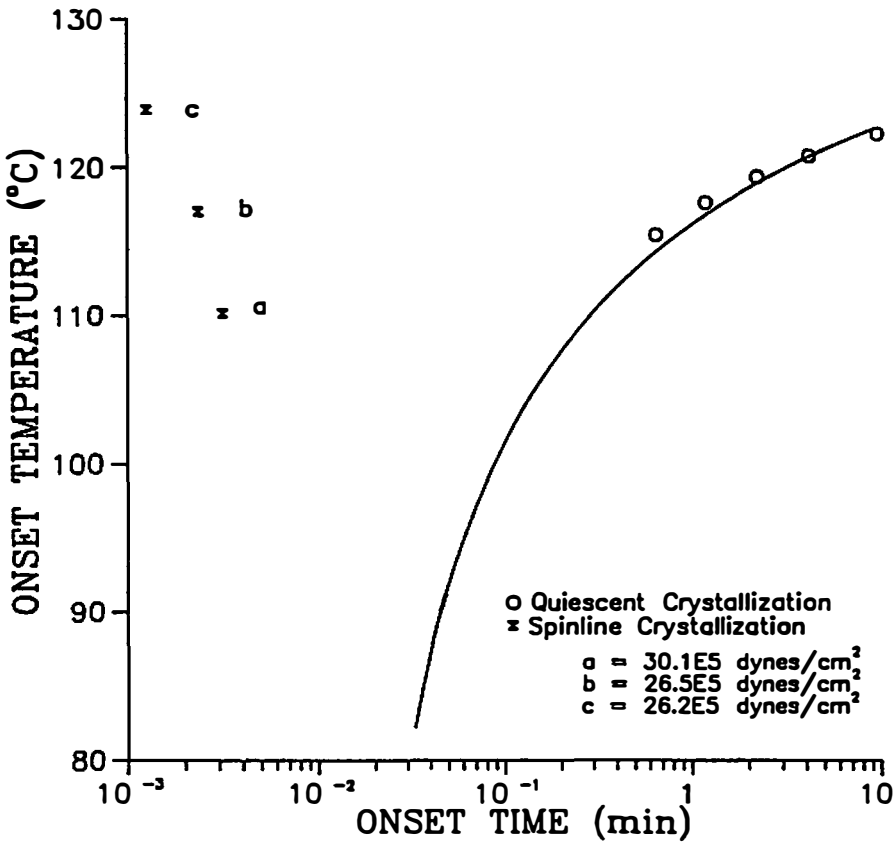

Figure 46. HD10 CCT analysis.

equipment, the melt spinning onset temperatures for LL4 and HD10 are the result of model predictions, not direct experimental measurement. The diameter and birefringence predictions for LL4 and HD10 were worse than for the less viscous resins, LL26 and LL40 [8].

4.4 Melt Spinning Computer Simulation

Use of the University of Tennessee's melt spinning model requires that many coefficients and parameters be known. A number of these coefficients are available in the literature; however, the most important parameters, elongational viscosity and heat transfer coefficients, cannot be reliably approximated from literature values. These parameters must be determined experimentally. To accomplish this, Bheda [4] developed an "inversion" procedure based on the work of George and Deeg [91]. In the inversion procedure, elongational viscosity and heat transfer coefficients are extracted from experimental diameter and temperature profiles using a variant of the melt spinning model. Once the elongational viscosity and heat transfer coefficients are approximated, these parameters and those obtained from the literature may be used to model the spinline.

To model the melt spinning processes, Zieminski [15] made appropriate assumptions and simplifications to the fundamental

equations of continuity, momentum, and energy transfer [71]. Zieminski [15] demonstrated that these equations reduce to a set of ordinary differential equations. The equations are shown in Figure 47. Several of these equations were shown in previous chapters.

Summary of Data Required for Modeling

A listing of the material parameters and coefficients required by the model are reported below. The density of polyethylene melt was taken as [120,121]

$$\rho_{am} = [1.135 + 0.00104(T)]^{-1} \qquad (4\text{-}21)$$

and in the solid as [122]

$$\rho = \left[\frac{1}{\rho_{am}} + \Theta\left(\frac{595\text{-}0.837(T)}{599\text{-}T} - \frac{1}{\rho_{am}}\right)\right]^{-1} \qquad (4\text{-}22)$$

where ρ and T have units of g/cm^3 and °C, respectively.

Elongational viscosity is written as a function of temperature and crystallinity in the following form

$$\eta_e = A\exp\left[\frac{E}{R(T+273)}\right]\exp\left[a\left(\frac{\Theta}{\Theta_\infty}\right)^b\right] \qquad (4\text{-}23)$$

The pre-exponential constant A and the activation energy E are

1. CONTINUITY

$$W = (\pi D^2/4)v\rho$$

$$D = \sqrt{4w/\pi\rho v}$$

$$v(0) = v_o \text{ with } D = D_o$$

2. MOMENTUM BALANCE

$$dF_{rheo} = dF_{inert} + \delta F_{drag} - \delta F_{grav}$$

$$dF_{inert} = w \cdot dv$$

$$\delta F_{drag} = \pi \rho_{air} C_D v^2 D \, dz$$

$$\delta F_{grav} = (wg/v) \, dz$$

$$F_{inert}(0) \approx 0$$

$$F_{rheo} = ? \text{ (Guess)}$$

3. ENERGY BALANCE

$$\frac{dT}{dz} = \frac{\pi D h (T-T_a)}{WC_p} + \left(\frac{\Delta H}{C_p}\right)\frac{d\Theta}{dz} \qquad T(0) = T_o$$

4. RHEOLOGICAL EQUATION

$$dv/dz = \sigma/\eta_e$$

$$\sigma = F_{rheo}/(\pi D^2/4)$$

$$T > T_m \Rightarrow \eta_e = A\exp[E/R(T+273)]$$

$$T < T_m \Rightarrow \eta_e = A\exp[E/R(T+273)]\exp[a(\Theta/\Theta_\infty)^b]$$

5. BIREFRINGENCE AND ORIENTATION

$$\frac{d\Delta n_a}{dz} = C_{op}\frac{d\sigma}{dz} \qquad \Delta n_a(0) = \Delta n_{ao}$$

$$\Delta n = (1-\Theta)\Delta n_a + \Theta f_c \Delta_c^\circ$$

$$f_a = \Delta n_a/\Delta_a^\circ$$

6. CRYSTALLIZATION KINETICS

$$\frac{d\Theta}{dz} = \frac{\Theta_\infty n K}{v}\left(\int\frac{K}{v}\,dz\right)^{n-1}\exp\left[-\left(\int\frac{K}{v}\,dz\right)^n\right], \quad \Theta(0) = 0$$

$$K(T) = K_0\exp\left[\frac{-U^*}{R(T-T_\infty)}\right]\exp\left[\frac{-C_3}{T\Delta T + CT^2 f_a^2}\right]$$

Figure 47. Working relationships of the fiber spinning model.

determined separately for each polymer from the inversion procedure. The exponential term in equation (4-23) which describes the effect of crystallinity on elongational viscosity was suggested by Kikutani [123]. The weighting constants a and b have to be determined through a trial and error process, Lambach [8] used the values of 12.5 and 2 for a and b. Zhou [14] used the values of 4.605 and 12 for a and b, respectively.

The specific heat of polyethylene as a function of temperature was expressed as [124]

$$C_p = 0.490 + 0.000867(T) \qquad (4\text{-}24)$$

where C_p has units of cal/g·°C and T has units of °C. The heat of fusion was assumed to be 66 cal/g [125]. The intrinsic amorphous and crystalline birefringences were set to 0.0428 and 0.0572, respectively [82]. Due to an absence of literature values for Young's modulus for polyethylene near T_m, the change in amorphous birefringence was modeled as

$$\frac{d\Delta n_a}{dz} = C_{op}\frac{d\sigma}{dz} \qquad (4\text{-}25)$$

The stress optical coefficient was set equal to 1.5×10^{-10} $cm^2/dyne$ [126].

An important crystallization kinetic parameter is the Avrami index. The most reliable experimental data on stress enhanced

crystallization has been obtained from cross-linked systems. Crystallization rates and Avrami indices have been shown to be controlled by deformation. Gent [127] studied the effect of deformation on the crystallization rate of cross-linked rubbers. Gent observed an increase in crystallization rate and a decrease in the Avrami index until n = 1 as deformation increased. Kim and Mandelkern [128] also studied cross-linked rubbers and reported similar results. They report an Avrami index = 3.6 at an extension ratio of 1 and an Avrami index = 1.3 at an extension ratio of 6. Kawai et al. [129] studied the isothermal crystallization kinetics of cross-linked, elongated polyethylene. They found an Avrami index ≈ 1 during the initial stages of crystallization, but as transformation progressed, the crystallization changed to one which could not be modeled by an Avrami equation. Given the above studies, the Avrami index was set to unity for all melt spinning simulations. Katayama and Yoon [66] also modeled the melt spinning process and chose n = 1.

Inversion of the Computer Model

The inversion procedure was used to generate separate elongational viscosity and heat transfer coefficients for each resin at the highest mass throughput - lowest spinning speed conditions available in order to minimize the effects of crystallinity. A detailed explanation of this procedure is available in reference [4].

The inversion procedure will be briefly outlined below.

1. Diameter and temperature profiles are fitted to polynomial functions.

2. The fiber velocity profile is calculated using the continuity equation.

3. The smooth velocity and temperature profiles are differentiated to obtain the velocity gradient dv/dz and the temperature gradient dT/dz profiles along the spinline.

4. The heat transfer coefficient is given as

$$h = \frac{-wC_p}{\pi D(T-T_a)} \frac{dT}{dz} \qquad (4\text{-}26)$$

and the "apparent" elongational viscosity is given by

$$\eta_{eapp} = \sigma\left(\frac{dv}{dz}\right)^{-1} \qquad (4\text{-}27)$$

where

$$\sigma = \frac{F_{rheo}}{(\pi D^2/4)} \qquad (4\text{-}28)$$

Step 4 requires a guess for F_{rheo} at the die. If this guess is correct,

the predicted tension will equal the measured tension and the best approximation of η_{eapp} and h are obtained. If not, a new guess for $F_{rheo}(0)$ is made and the procedure is repeated. To facilitate this, a BASIC language computer program was written which performs steps 2-4 and the tension predictions.

As mentioned above, the apparent elongational viscosity is found. The word apparent is used because a non-Newtonian viscoelastic fluid is modeled as a Newtonian fluid. Generally, most polymers exhibit non-Newtonian viscoelastic behavior and their viscosities will depend on both deformation histories and rates.

The inversion procedure is applied to the spinline regions where crystallinity is absent. In the absence of crystallinity, η_{capp} and h may be modeled in the following form

$$\eta_{eapp} = A\exp\left[\frac{E}{R(T+273)}\right] \qquad (4\text{-}29)$$

$$h = h_1\left(\frac{v}{A}\right)^{h_2} \qquad (4\text{-}30)$$

where A, h_1, and h_2 are constants, E is the activation energy for flow, R is the ideal gas constant, and v and A are the local fiber velocity and cross-sectional area. The apparent elongational viscosity and heat transfer coefficient have units of dyne·sec/cm^2 and cal/s·cm^{2}·°C, respectively. The form of equation (4-30) was suggested by Kase and Matsuo [87].

Experimental viscosity versus reciprocal temperature data for LL4.3 at 2.01 g/min and 173 m/min are plotted on Figure 48. Least squares regression was used to fit equation (4-29) to these data. The fitting parameters for the resins are listed in Table 13. The apparent elongational viscosities found in this study and by Lambach [8] are shown in Figure 49. The extrusion temperatures for LL26, LL40, and HD10 were 185 °C while for the other samples 215 °C was used. Notice that approximately two decades separate the viscosities of these resins. Lambach [8] studied melt spinning of LL4, LL26, LL40, and HD10. He observed that as melt index increased η_{eapp} decreased for these resins. However this does not hold for the lower MI resins. Resins LL3.9, LL4, and LLP have melt indices equal to four. However inspection of Figure 49 reveals very large differences in η_{eapp} between these resins. Obviously melt index alone does not control the η_{eapp} for the more viscous resins. Long chain branching is known to increase melt viscosity due to entanglements, however no information of this type is available. The relative differences in η_{eapp} are easily seen in the experimental data. Consider the diameter profiles shown in Figure 30. Notice that in the region from 30 to 60 cm from the spinneret, the resin with the largest η_{eapp} (LL3.9) also shows the greatest diameter. Likewise the sample with the least η_{eapp} (LLP) draws down the quickest. The tension data also follows this trend. For the runs compared above, LLP has the lowest tension while LL3.9 has the highest, see Table 11. Therefore the values of η_{eapp}

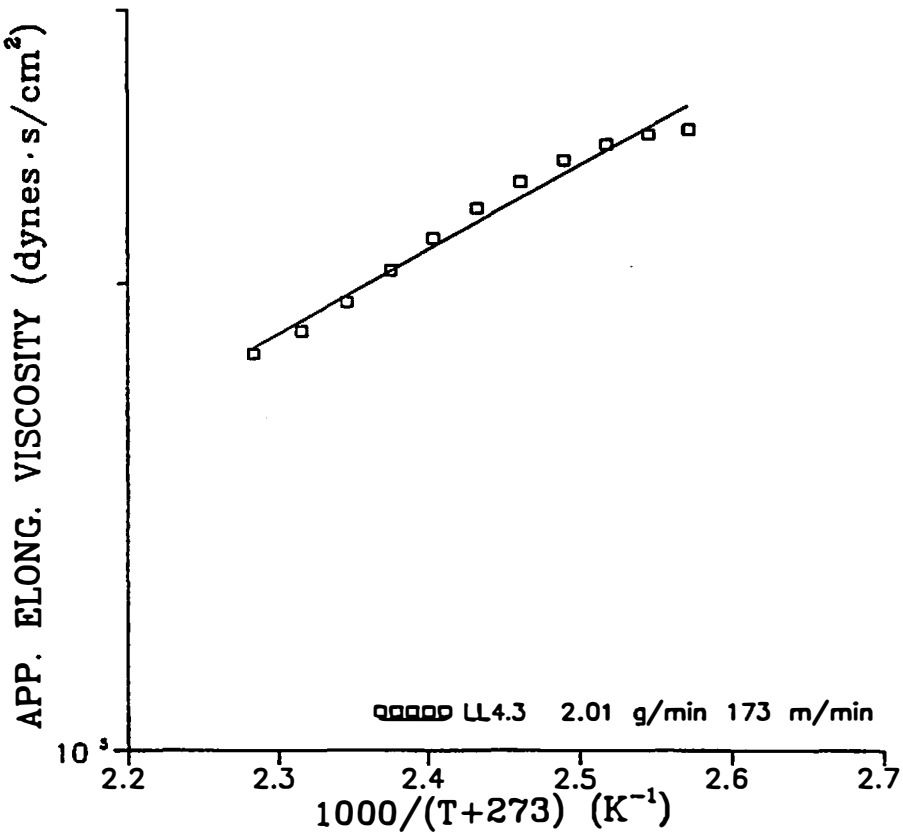

Figure 48. Elongational viscosity versus 1/T for LL4.3.

Table 13. Apparent Elongational Viscosity and Heat Transfer Coefficient Fitting Parameters

Resin	A	E/R	h_1	h_2
LL3.9	2636	1975	4.37×10^{-4}	0.161
LLP	2452	1212	5.76×10^{-5}	0.326
LL4.3	10564	1246	1.65×10^{-4}	0.236

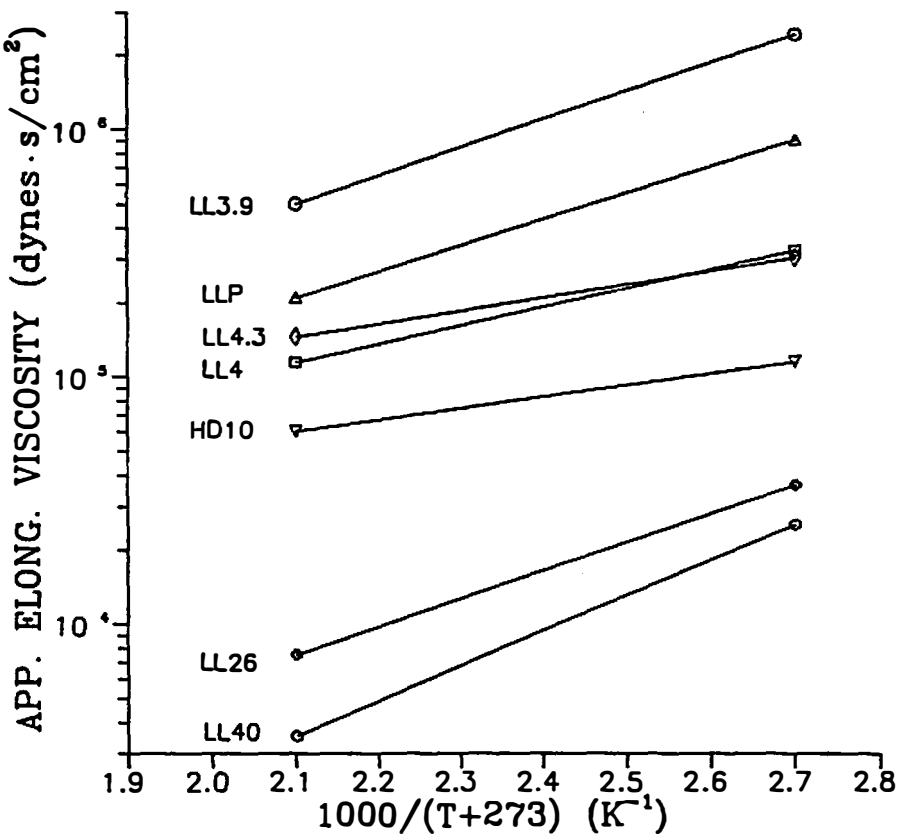

Figure 49. Elongational viscosity versus 1/T for all resins.

appear to be qualitatively correct. Figure 50 presents experimental values for the heat transfer coefficient as determined by the inversion technique for LL4.3 at 2.01 g/min and 173 m/min. Least squares regression was used to fit equation (4-30) to this data. The fitting parameters for the resins are listed in Table 13. Lambach [8] reported heat transfer coefficients which were essentially the same for LL4, LL26, LL40, HD10. The heat transfer coefficients found in this study and by Lambach are shown in Figure 51. Inspection of Figure 51 reveals that the heat transfer coefficients for LLP and LL4.3 are similar to that found by Lambach [6]. On the other hand, LL3.9's heat transfer coefficient is observed to be different. The value of h_2 found for LL3.9 was smaller than for the other resins. This low value results in the small slope for LL3.9 found in Figure 51. This difference may be due to some environmental effects such as cross air currents or a change in ambient temperature that was not noticed. Lambach was able to calculate heat transfer coefficients over a much larger range of velocity/area (due to the higher spinning speeds and smaller fiber diameters obtainable) than could be accomplished in this study. The effect of temperature gradients are ignored and they may be greater for the large filaments produced in this study. This probably contributes to the differences observed.

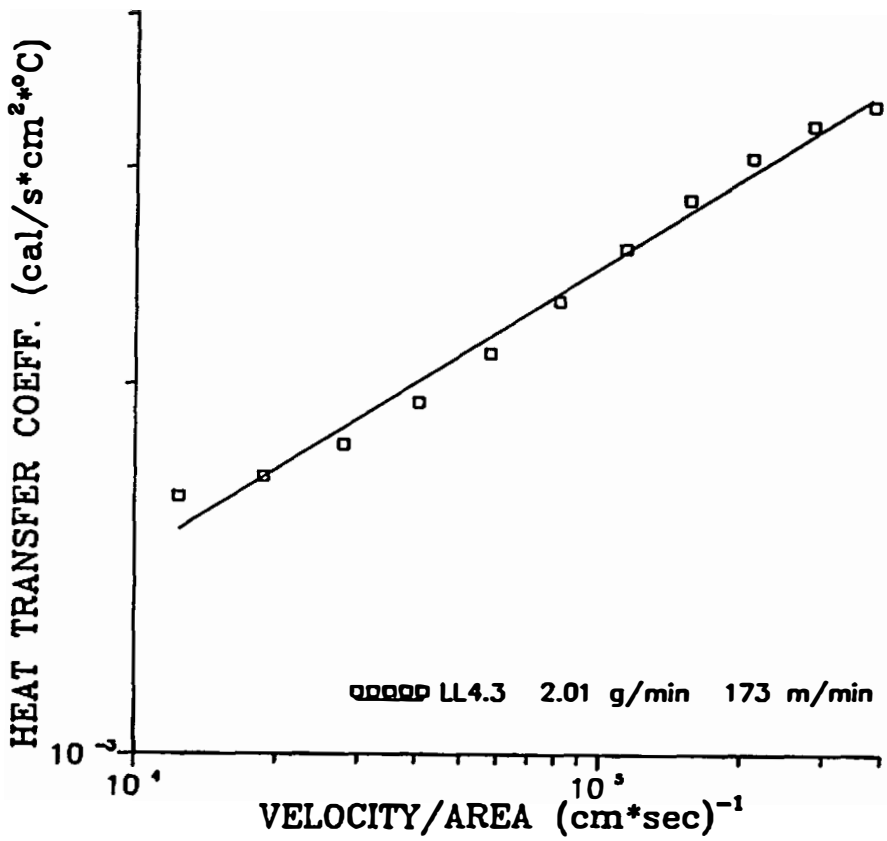

Figure 50. Heat transfer coefficient relation from inversion procedure.

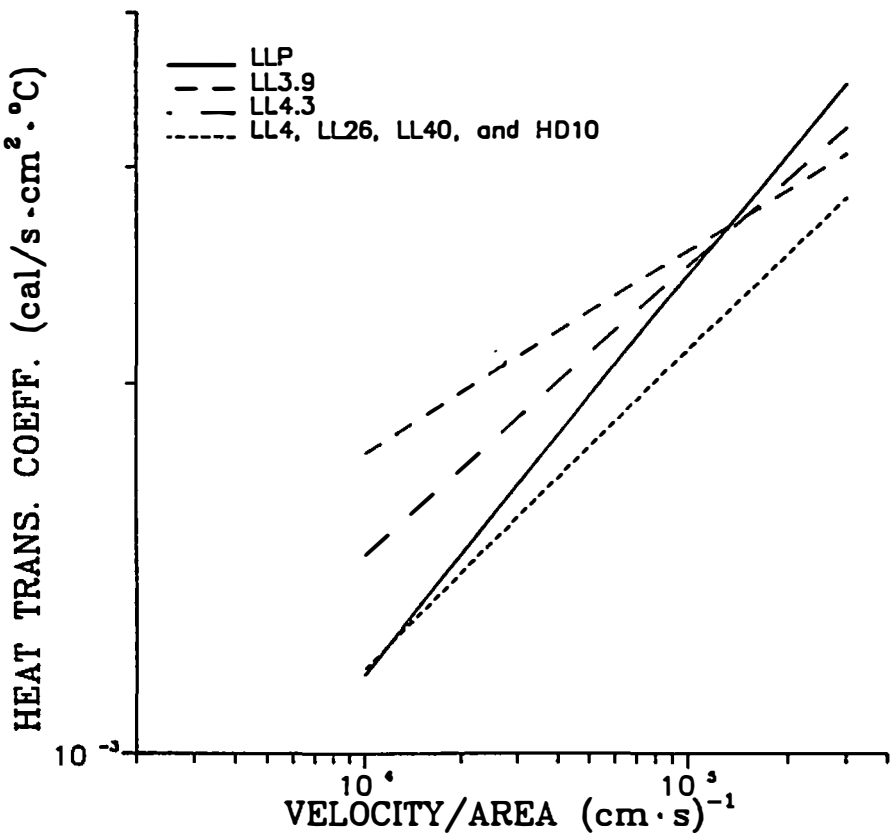

Figure 51. Comparison of heat transfer coefficient from inversion procedure with previous results.

Computer Modeling

A BASIC language computer program was utilized to simulate the melt spinning process. The simulation program requires four coefficients: an initial guess of the rheological force at the die $F_{rheo}(0)$, the crystallization-stress coefficient C, and the viscosity-crystallinity coefficients a and b. The equations which require a, b, and C are reshown below.

$$\eta_{eapp} = A\exp\left[\frac{E}{R(T+273)}\right]\exp\left[a\left(\frac{\Theta}{\Theta_w}\right)^b\right] \qquad (4\text{-}23)$$

$$K(T,f_a) = K_o\exp\left[\frac{-U^*}{R(T-T_\infty)}\right]\exp\left[\frac{-C_3}{T\Delta T+CT^2f_a^2}\right] \qquad (2\text{-}38)$$

The simulation process will be briefly outlined below.

1. Initial guesses of $F_{rheo}(0)$, a, b, and C are supplied to the program.

2. The simulation is run and the predicted final diameter is compared to the experimentally measured final diameter. If the predicted and experimental final diameter values differ, the simulation is rerun with a different choice of $F_{rheo}(0)$ until the diameters are the same.

3. The coefficient C is adjusted as necessary to correctly predict the temperature and birefringence profiles.

4. If predictions are not satisfactory, the viscosity-crystallinity coefficients a and b are changed and steps 2 and 3 are repeated.

This procedure is the same as was used by Lambach [8] and Zhou [14]. The LL3.9, LLP, and LL4.3 spinline behavior was not as successfully predicted as was polypropylene [14] and low viscosity LLDPE [8]. As elastic effects were less obvious in LL3.9, modeling efforts concentrated on this resin and will be reported in this work. On the following figures, the spinning conditions, viscosity-crystallinity coefficients a and b, and crystallization-stress coefficient C are listed in the legend.

Figure 52 shows the fiber diameter and temperature profiles predicted for the LL3.9 resin at 2.00 g/min and 61 m/min spinning speed. Notice that depending on the viscosity-crystallinity coefficient a, different diameter profiles are obtained. As a increases, η_{eapp} will increase for a given level of crystallinity. This increase in η_{eapp} results in an attenuation in the drawdown process. Therefore in order to achieve the same diameter, the $F_{rheo}(0)$ has to be increased which results in a more rapid drawdown. The temperature profiles are essentially

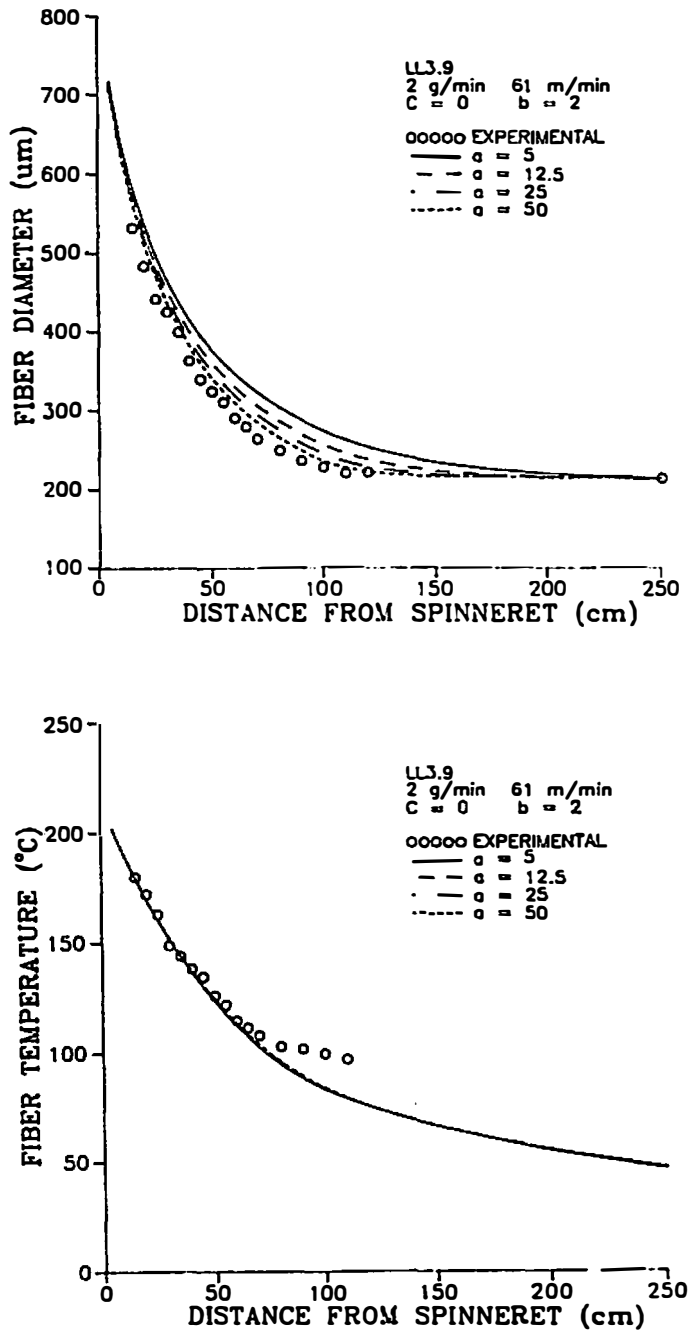

Figure 52. Comparison of predicted diameter and temperature profiles for LL3.9 with C = 0.

the same. This is to be expected as C was set to zero for these runs. By setting C to zero, crystallization will only be influenced by cooling effects. The experimentally observed plateau is not predicted, indicating that a non-zero value of C is required for plateau formation at these conditions.

The corresponding birefringence and crystallinity predictions are shown in Figure 53 and are less than that observed experimentally. One interesting feature about the crystallinity predictions is that as a increases, the level of crystallinity decreases. This phenomena is due to the fiber velocity. As was shown in Figure 52, the diameter drawdown is more rapid as a increases thus fiber velocity increases in the crystallization region. This increase in velocity results in an increase in cooling rate. This difference in cooling rate causes the slight difference in crystallinity predictions. The low crystallinity values and relative differences are also reflected in the predicted birefringence profiles. The model requires the as-spun value of f_c, however as orientation functions were not measured, a value of 0.22 was supplied in order to observe the model's behavior. The predicted profile does not rise as rapidly as the actual data. From Figure 52 and 53, it is clear that for these spinning conditions, a nonzero value of C is required. This provides further evidence that there is an influence of stress in the crystallization rate.

Figures 54 and 55 show predicted profiles for the same

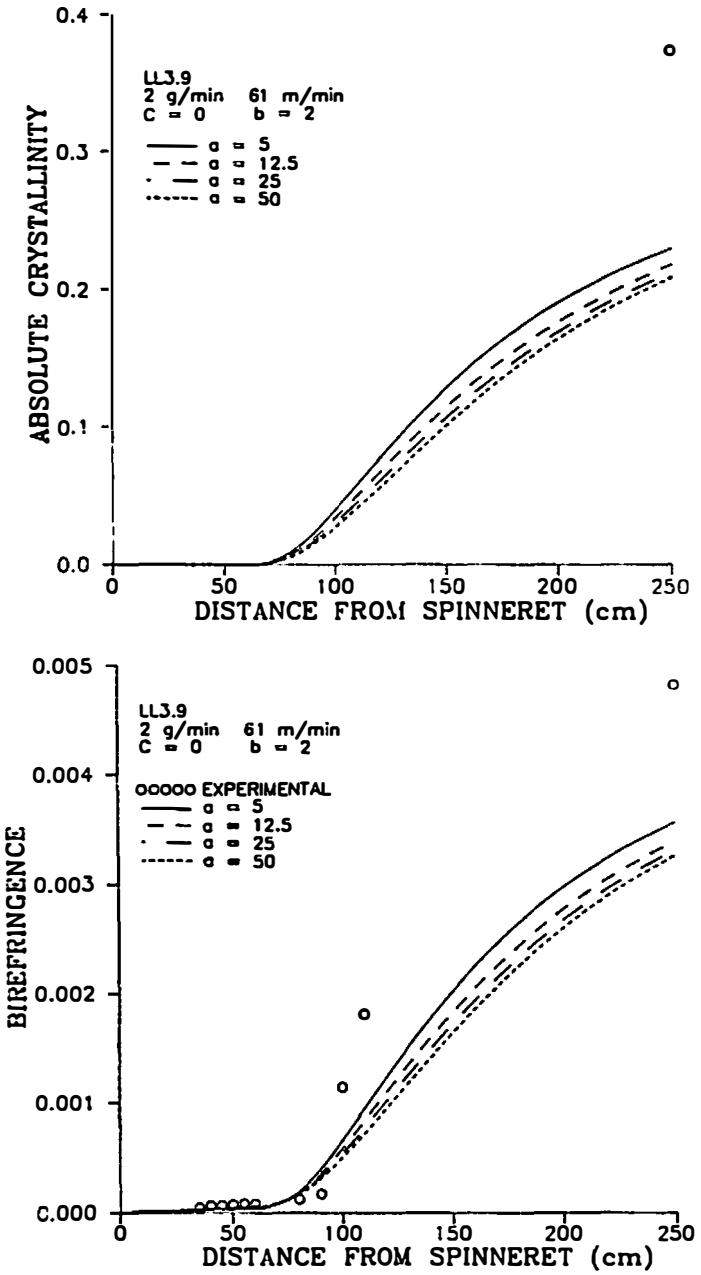

Figure 53. Comparison of predicted crystallinity and birefringence profiles for LL3.9 with C = 0.

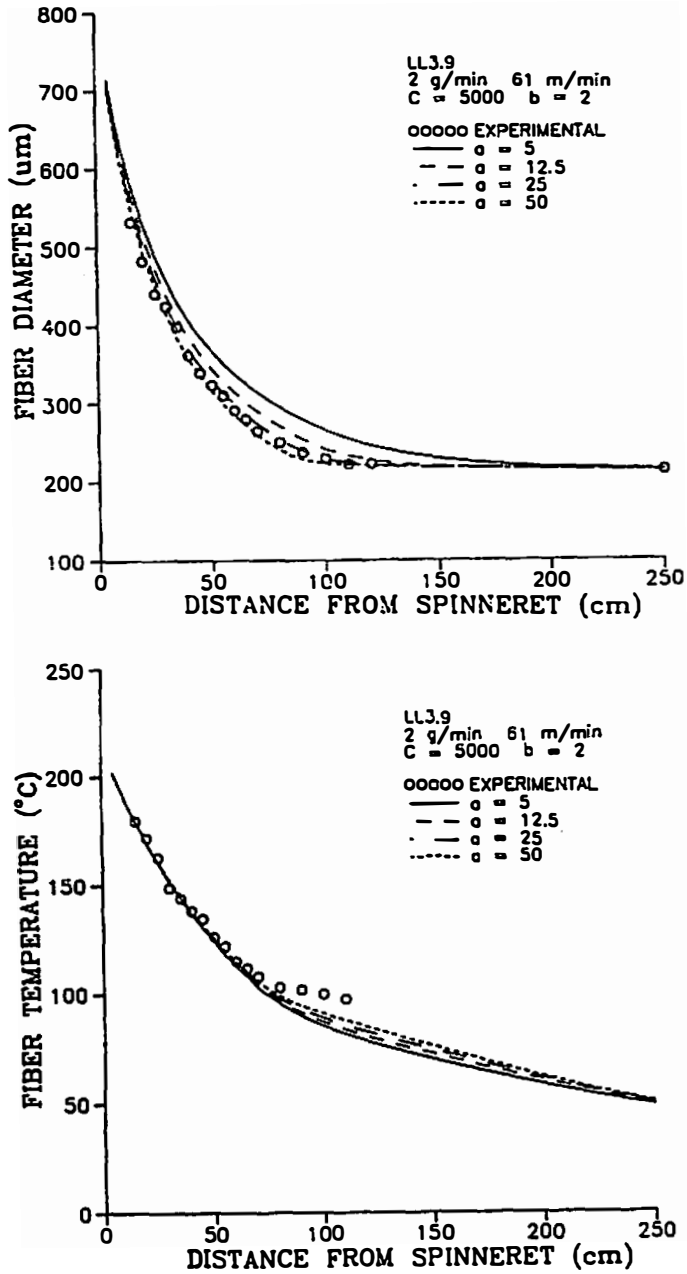

Figure 54. Comparison of predicted diameter and temperature profiles for LL3.9 with C = 5000.

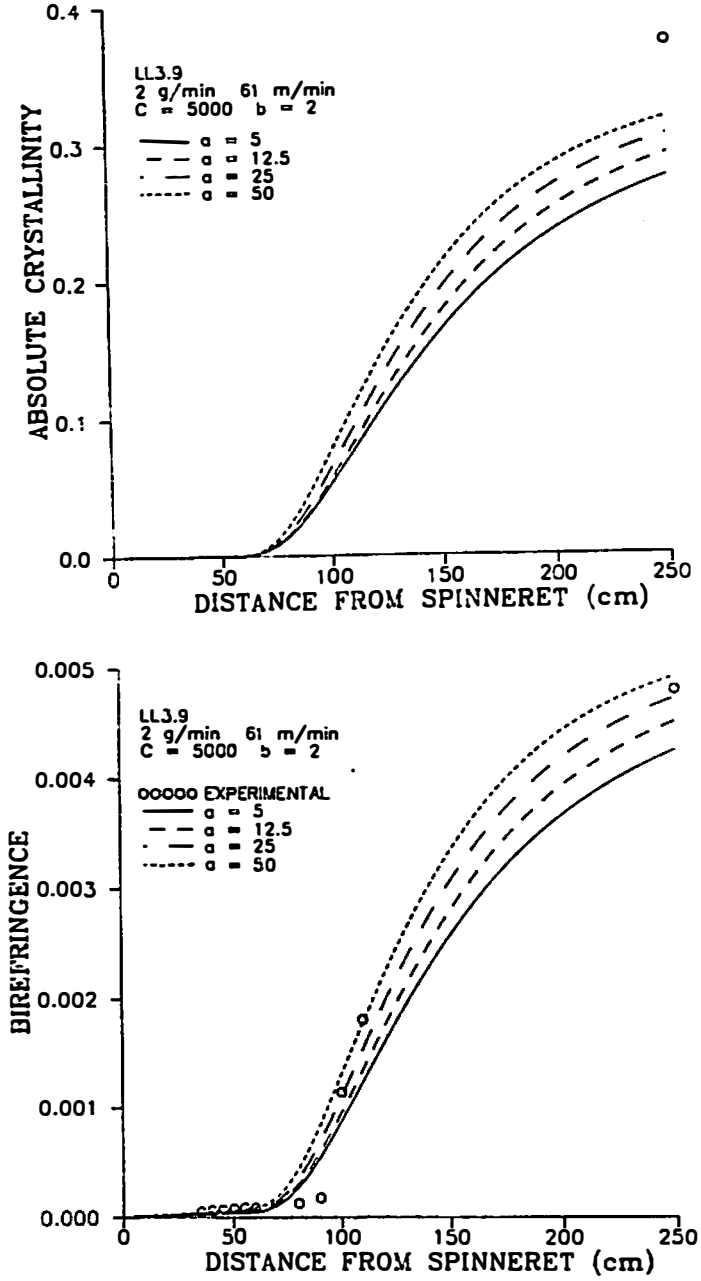

Figure 55. Comparison of predicted crystallinity and birefringence profiles for LL3.9 with C = 5000.

spinning conditions with C = 5000. Use of this value of C results in a faster rate of crystallization and a greater amount of terminal crystallinity. This increase in crystallinity will result in a larger η_{eapp} and so $F_{rheo}(0)$ must be increased to compensate. Table 14 shows the values of $F_{rheo}(0)$ required for different choices of a and C. Notice that an increase in either a or C necessitates the use of a larger $F_{rheo}(0)$ in order to compensate for the more rapid attenuation of diameter. Inspection of Figures 54 and 55 reveal the effects of a non-zero value of C. The fiber diameter profiles have drawn down more. The differences between temperature profiles may be distinguished. That profile having the highest $F_{rheo}(0)$ also has the highest temperature. The crystallinity profile exhibits a larger terminal crystallinity. The greater stress present in the a = 50 run results in greater crystallinity and birefringence. Comparison with Figures 52 and 53 shows that the jump in birefringence occurs closer to the spinneret. Therefore as C is increased such that the temperature profile is matched, the jump in birefringence predicted by the model will occur closer to the spinneret. This situation is common to all of the simulation runs.

Simulated profiles of LL3.9 at 2.00 g/min and 190 m/min are found in Figures 56 through 59 for C = 0 and C = 500. If a value of C = 5000 is used, the predicted temperature will be above the melting temperature of the resin. Use of C = 500 requires a larger value of $F_{rheo}(0)$ as was described previously.

Table 14. Initial Rheological Forces (dyne) As Required By Different Choices of a and C

Spinning Conditions	a	Crystallinity-stress factor C			
MFR/SS		0	500	1000	5000
2.00	5	355	355	356	363
	12.5	371	372	373	387
62	25	382	384	385	404
	50	392	394	396	420
2.00	5	420	427	441	-
	12.5	435	455	-	-
190	25	449	487	-	-
	50	464	521	-	-
1.25	5	338	340	343	450
	12.5	360	365	370	-
66	25	375	381	388	-
	50	387	395	404	-
1.25	5	394	-	-	-
	12.5	414	-	-	-
262	25	431	-	-	-
	50	449	-	-	-

For the $F_{rheo}(0)$ denoted by -, the values of C used were too large.

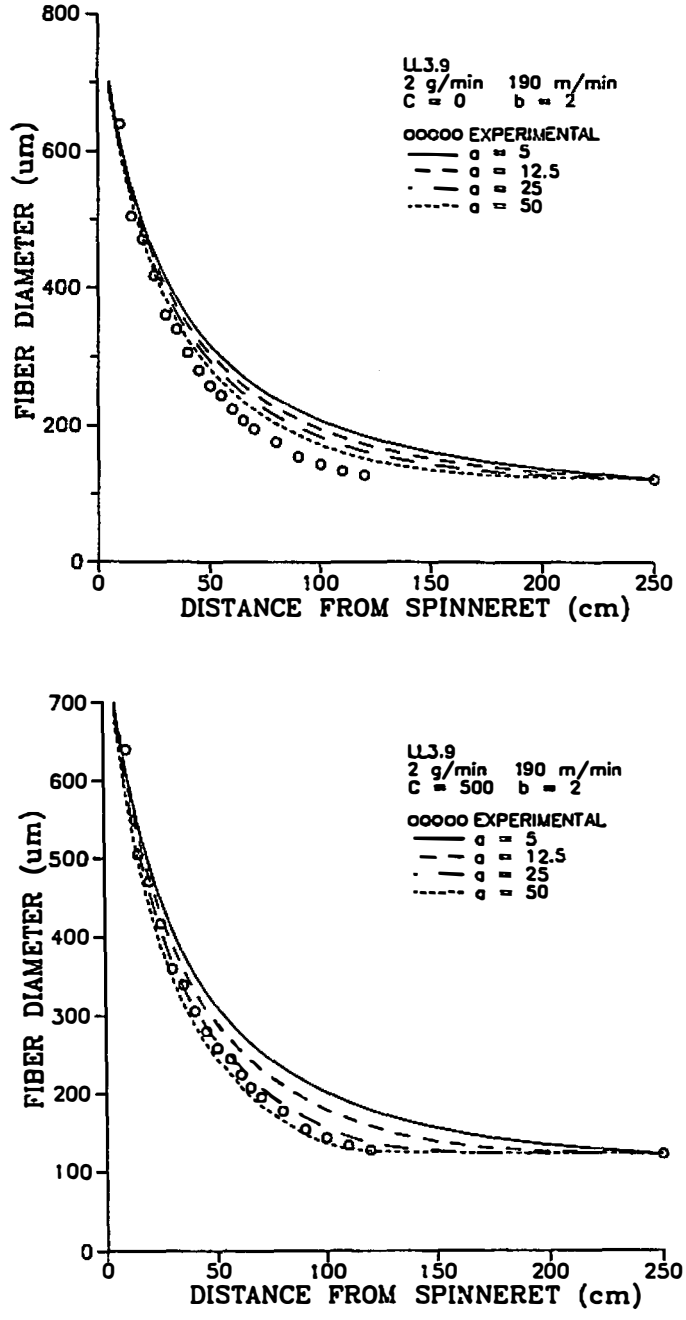

Figure 56. Comparison of predicted diameter profiles for LL3.9 with C = 0 and 500.

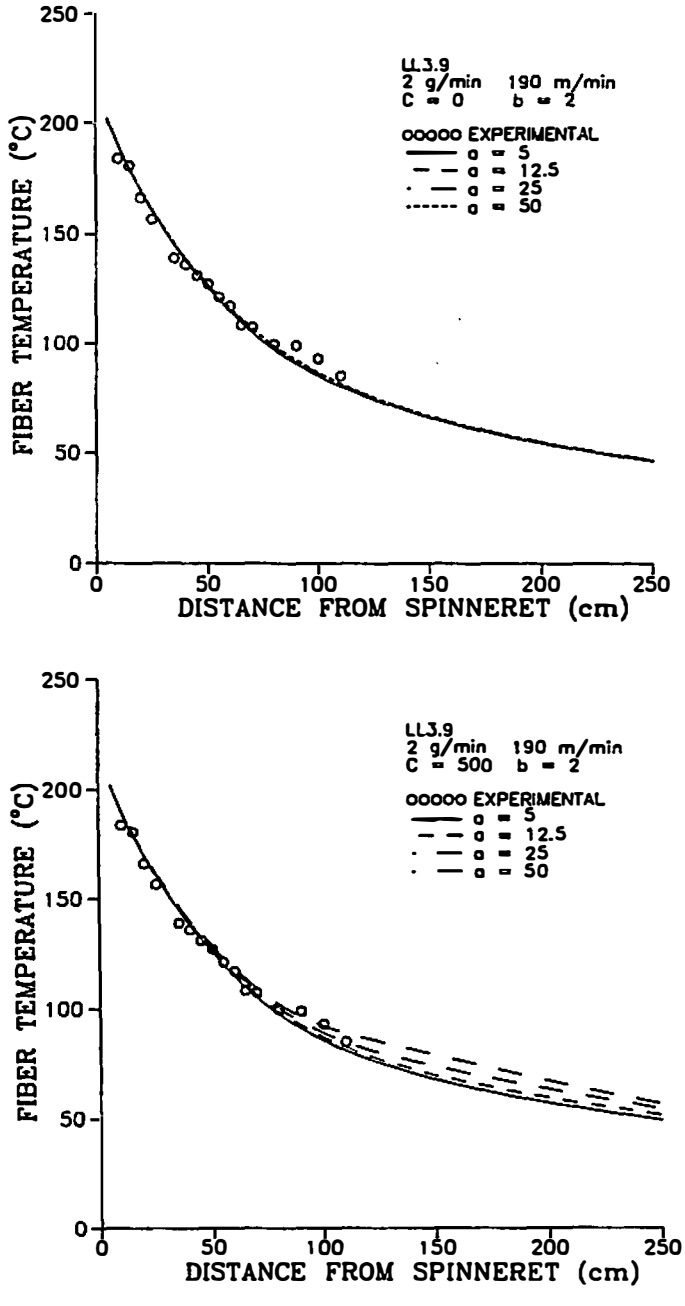

Figure 57. Comparison of predicted temperature profiles for LL3.9 with C = 0 and 500.

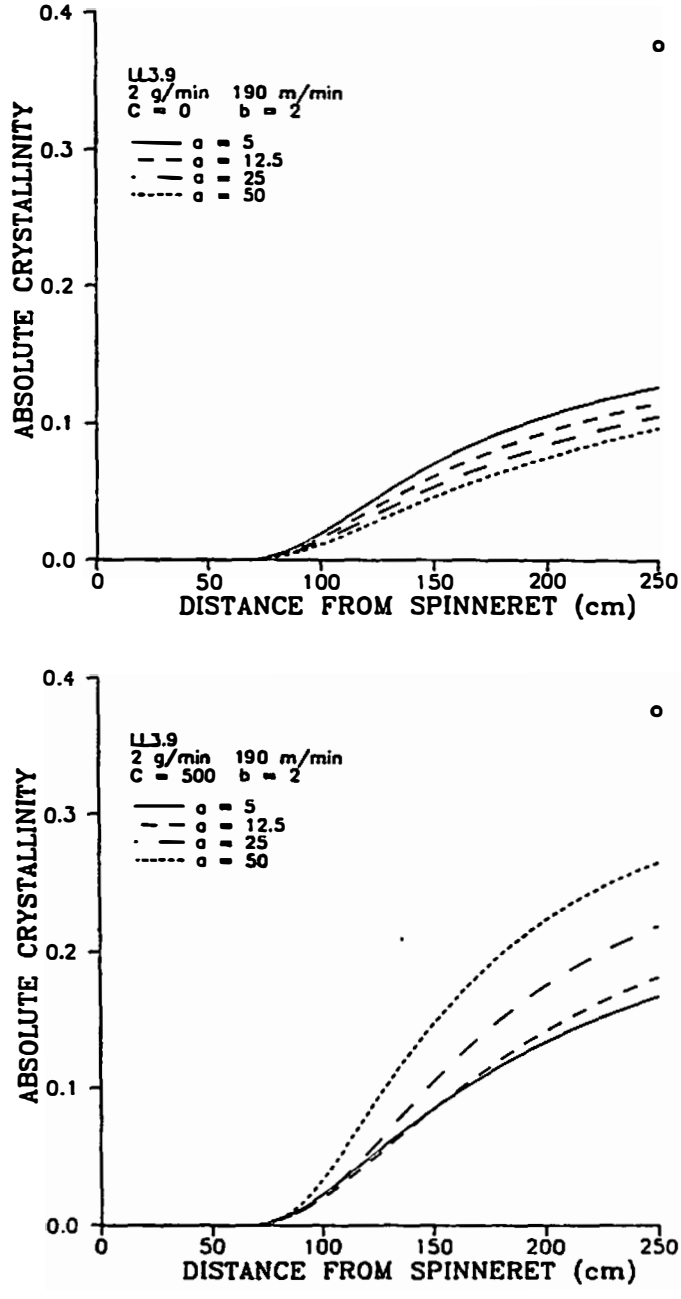

Figure 58. Comparison of predicted crystallinity profiles for LL3.9 with C = 0 and 500.

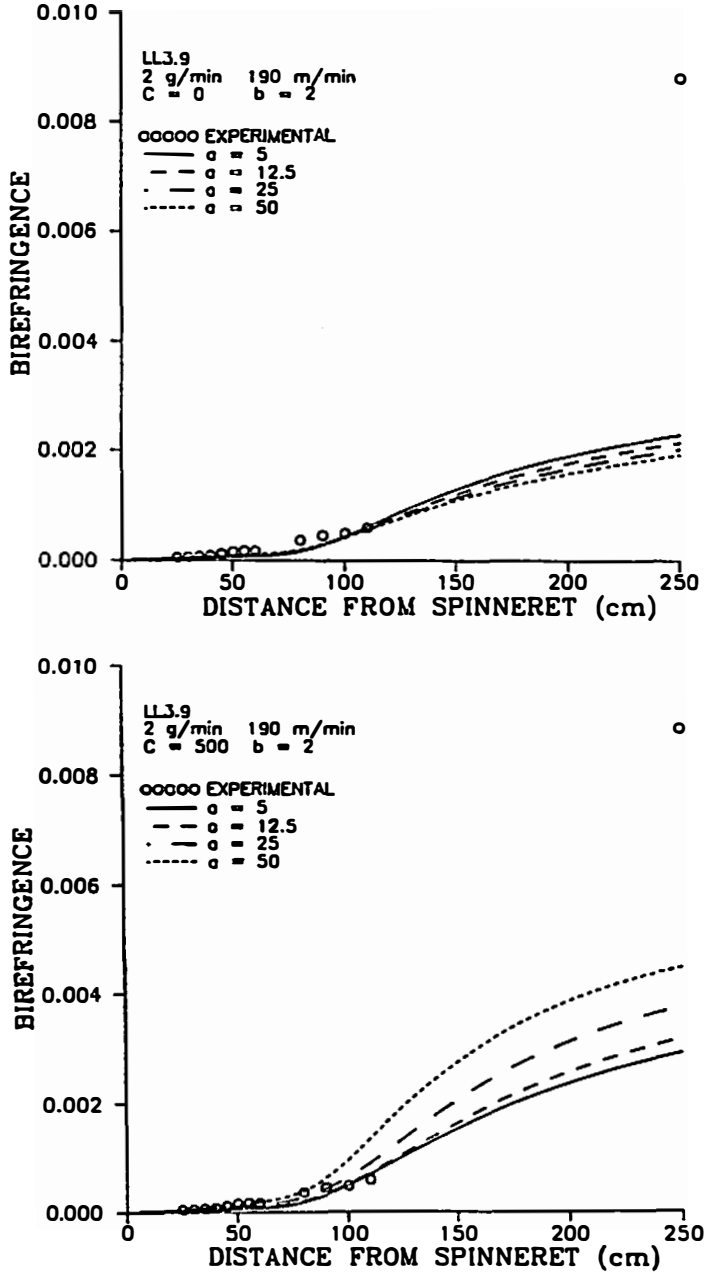

Figure 59. Comparison of predicted birefringence profiles for LL3.9 with C = 0 and 500.

The required values of $F_{rheo}(0)$ are found in Table 14. Concerning the diameter profiles, the expected increase in drawdown when $C \neq 0$ is observed. In Figure 57A, temperature profiles for $C = 0$ are displayed which show a slight difference due to cooling rate. Figure 57B shows good predictions for temperature when $C = 500$. However the birefringence and crystallization profiles do not precisely represent what was observed. Although the overall behavior is described, no consistent choice of a, b, or C was found which could successfully model the spinline.

The same features observed in modeling LL3.9 at 2.00 g/min are found at 1.25 g/min. Generally these predictions were worse than those found for the 2.00 g/min simulations. A tabulation of the required values of $F_{rheo}(0)$ are found in Table 14. Common to the simulations found in Table 14 is the value of the viscosity-crystallinity coefficient b, set to two. The effect of b on the viscosity-crystallinity enhancement term

$$\exp\left[a\left(\frac{\Theta}{\Theta_\infty}\right)^b\right]$$

is shown in Figure 60. From Figure 60 it is apparent that as b increases, the effect of crystallinity on η_{eapp} is delayed. It is tempting to think that by increasing b, the delay of η_{eapp} enhancement due to crystallinity will force the drawdown

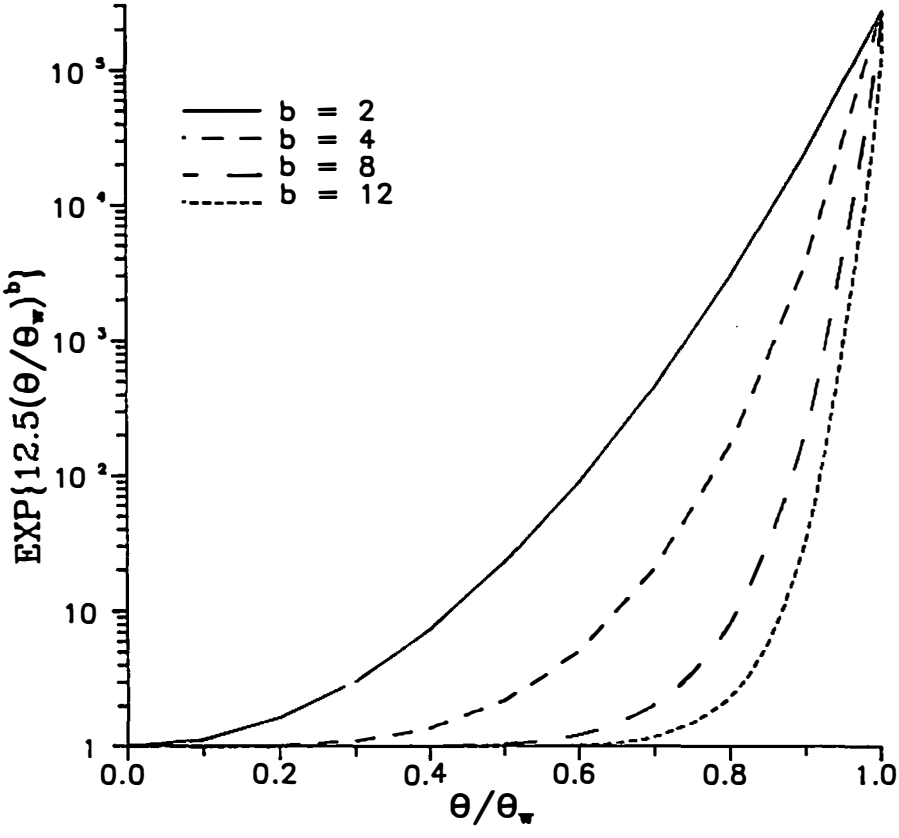

Figure 60. Evaluation of the crystallinity-viscosity enhancement function as a function of crystallinity.

profiles to match. However this is not the case. This delay of η_{eapp} enhancement due to crystallinity will retard the fiber attenuation process and the final diameter will be less than that experimentally observed. To compensate for this, the $F_{rheo}(0)$ could be decreased but then the drawdown profile in the upper part of the spinline would not match. If the value of C was increased to high enough levels to attenuate the drawdown process, the predicted birefringence profiles would deviate markedly from the experimentally observed profiles. Also the largest deviations in fiber diameter profiles is in the region where crystallinity is absent or quite small.

In order to better understand the effects of a and b on the model, the simulation was run differently. Instead of choosing a, b, and C and then adjusting $F_{rheo}(0)$ until both experimental and predicted diameters matched, the $F_{rheo}(0)$ was set such that the predicted and experimental diameters measured 60 cm from the spinneret matched. At this distance, the negligible amount of crystallinity present will eliminate the need of choosing a and b to obtain a correct diameter profile in the upper part of the spinline. Once $F_{rheo}(0)$ has been chosen, values of a and b are fixed in order to determine the value of C necessary to obtain the final diameter. This procedure was implemented and the results are described below.

Figures 61 through 64 show the predicted diameter, temperature, crystallinity, and birefringence profiles for LL3.9 at

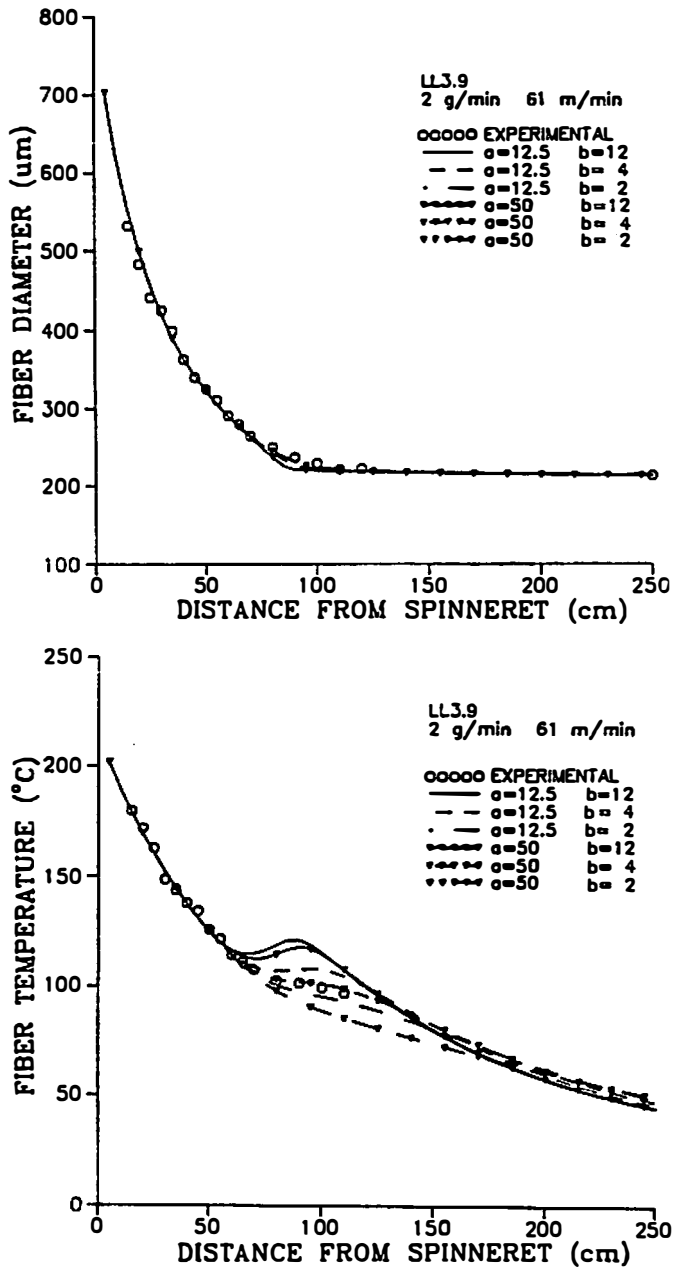

Figure 61. Predicted diameter and temperature profiles for LL3.9 at 2 g/min and 61 m/min with different values of a and b.

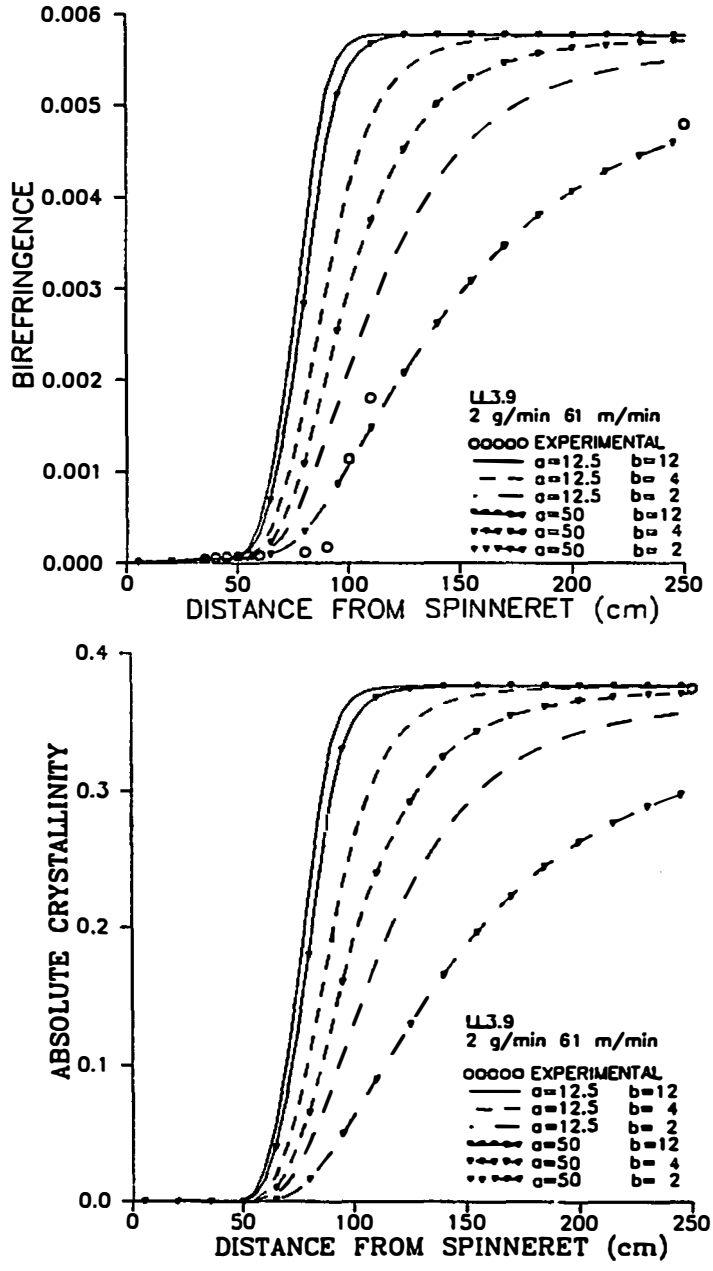

Figure 62. Predicted birefringence and crystallinity profiles for LL3.9 at 2 g/min and 61 m/min with different values of a and b.

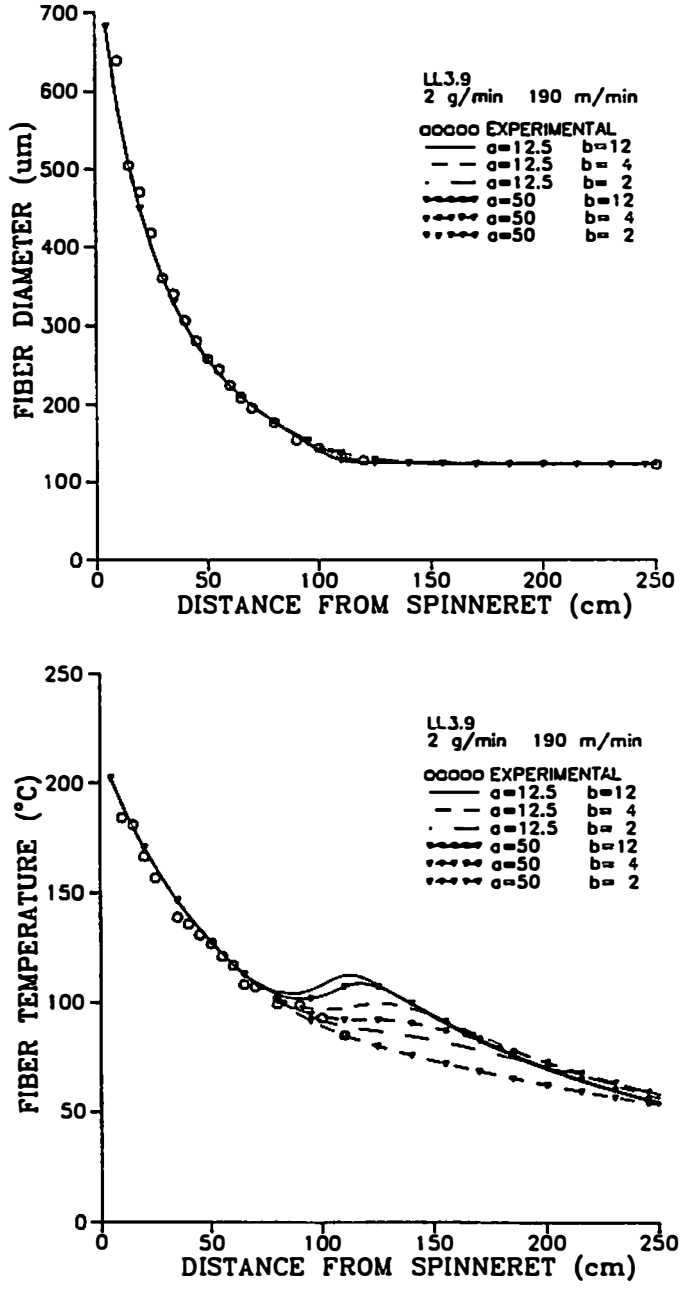

Figure 63. Predicted diameter and temperature profiles for LL3.9 at 2 g/min and 190 m/min with different values of a and b.

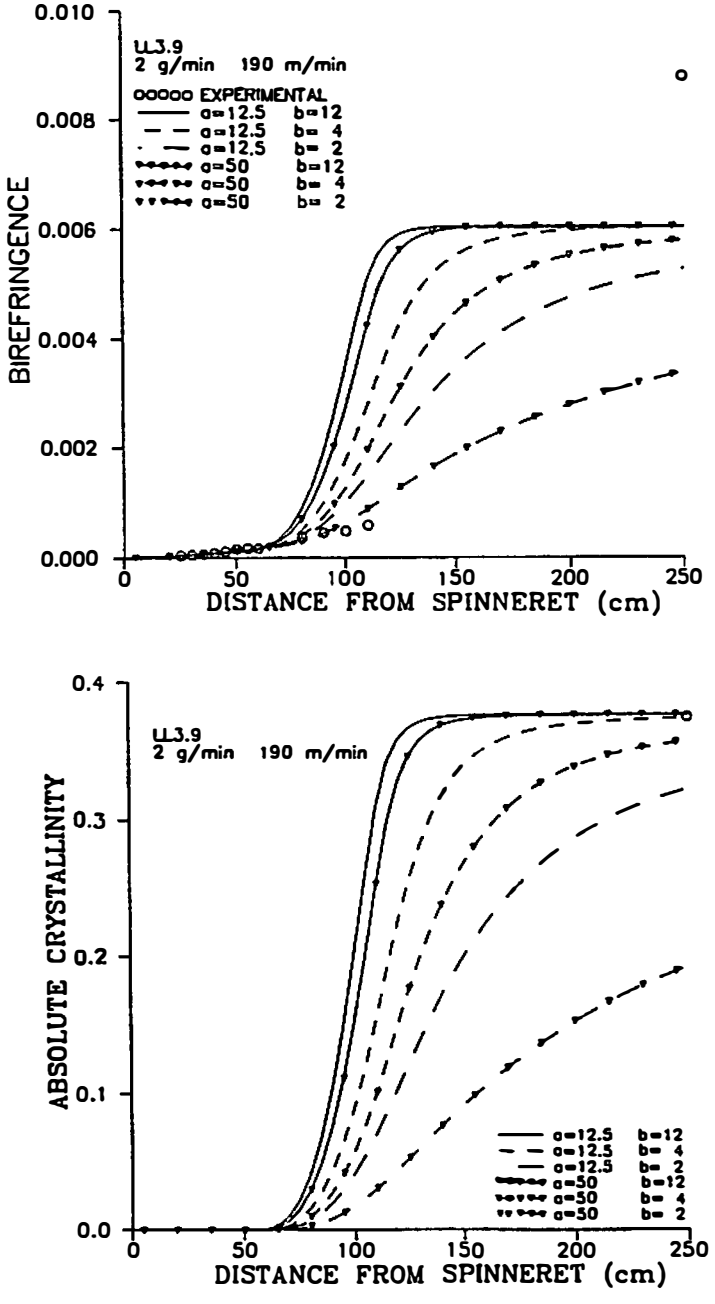

Figure 64. Predicted birefringence and crystallinity profiles for LL3.9 at 2 g/min and 190 m/min with different values of a and b.

2.00 g/min and spinning speeds of 62 and 190 m/min using different choices of a and b. Depending on these values, different C values are required. These values are found in Table 15. At a given spinning velocity, $F_{rheo}(0)$ is essentially constant because the coefficients a and b only become active when crystallinity is present. The different values of C cause the temperature profiles to very considerably in the plateau region. This feature is also reflected in the birefringence and crystallinity profiles.

The predicted diameter profiles are in excellent agreement with the experimental data. This indicates that the initial diameter drawdown profile is independent of a and b as expected. Inspection of the temperature and birefringence profiles shows that certain values of a and b do produce reasonable predictions. A choice of a = 50 and b = 4 with C < 12000 seems to produce the best predictions.
The effect of a and b on C is shown graphically in Figure 65. Large variations in C are observed. For polypropylene, Zhou [14] found C ≈ 1000. As C should be a constant for a given resin, ignorance of the true rheological behavior of these materials is a fatal problem. Assuming that a high viscosity, highly viscoelastic non-Newtonian fluid can be approximated as a Newtonian fluid is simply not adequate.

The likely causes for the differences observed in spinline modeling will now be discussed. Tension data is collected near the take-up device. For polyethylene, crystallization has already

Table 15. Required Values of C for Given Choices of a and b

Spinning Conditions	a	b		
MFR/SS		2	4	12
2.00	12.5	8760	15000	22700
62	50	4200	11300	19800
2.00	12.5	835	1400	2250
190	50	370	1050	1910
1.25	12.5	240	375	590
262	50	140	290	500

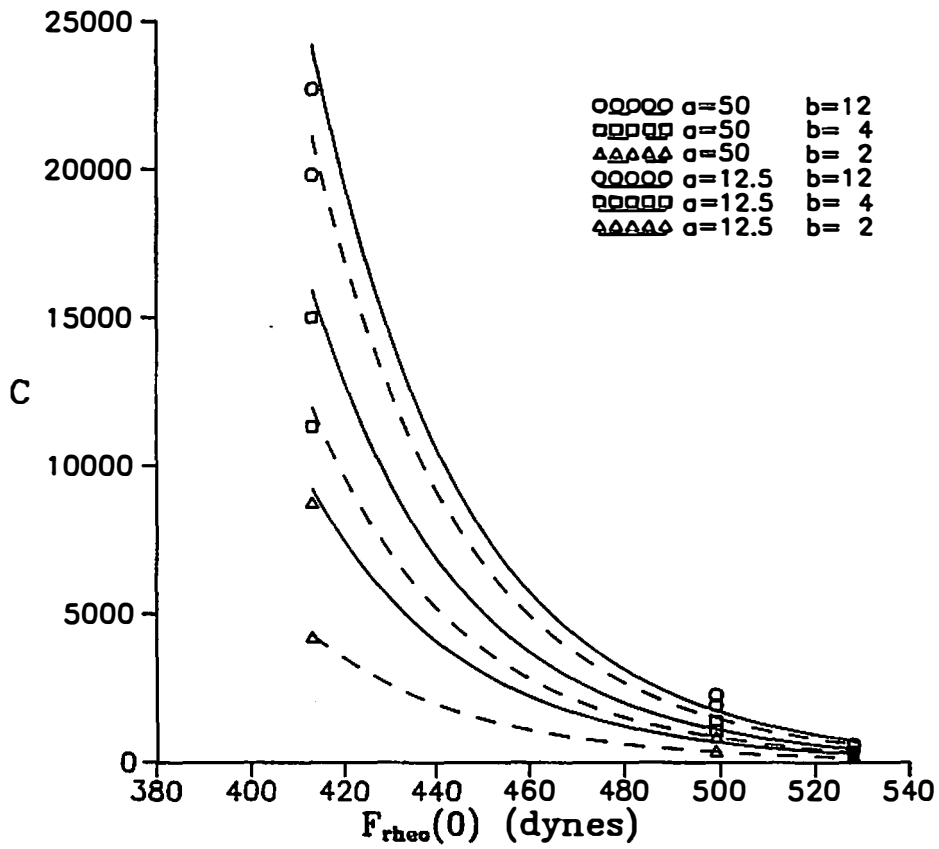

Figure 65. Crystallization-stress enhancement factor C as a function of $F_{rhco}(0)$ for different values of a and b.

begun to occur before this point is reached. When the inversion technique is used, the $F_{rheo}(0)$ is adjusted until the measured tension is predicted. Since the inversion technique assumes that no crystallinity is present, the technique will generate a prediction of η_{eapp} as a function of temperature whereas the prediction was based on both temperature and crystallinity phenomena. Therefore if the crystallinity is significant, the predictions of η_{eapp} will be too large. Also the coefficients which predict the rapid rise in η_{eapp} due to crystallization are unknown and a haphazard technique has to be employed to determine them. Lambach [8] was successful in modeling the low viscosity LL26 and LL40 resins. This suggests that error in the inversion technique is not significant when compared to the assumption that a highly viscoelastic, non-Newtonian fluid may be successfully modeled as a Newtonian fluid. Both cohesive and melt fracture was observed in these resins. These features are not found in Newtonian fluids. Incorrect predictions of the fiber stress will also cause errors in the predicted birefringence profiles. The birefringence is predicted by the following equations.

$$\frac{d\Delta n_a}{dz} = C_{op}\frac{d\sigma}{dz} \qquad (4\text{-}25)$$

$$\Delta n = (1 - \Theta)\Delta n_a + \Theta f_c \Delta_c^o \qquad (2\text{-}60)$$

A better formulation of (4-25) is given by

$$\frac{d\Delta n_a}{dz} = \frac{C_{op}E}{v}\frac{dv}{dz} - E\frac{\Delta n_a}{v\eta} \qquad (2\text{-}59)$$

This formulation includes the modulus E. Equation (2-59) should be better at predicting the development of birefringence in a highly viscoelastic fluid than equation (6-6). The amorphous orientation is given by

$$f_a = \frac{\Delta n_a}{\Delta_a^o} \qquad (2\text{-}61)$$

and f_a is the term whose square is used in calculating the enhancement of crystallization due to stress. Therefore there are many factors which prevent the successful modeling of the melt spinline for these resins and the accurate determination of the stress enhanced crystallization coefficient C.

The coefficient C may be thought of as a measure of the effectiveness of stress in enhancing crystallization. If stress plays a large part in increasing crystallization rates, the C would be large. Likewise if stress was not conducive to enhancing crystallization rates, C would be zero. The coefficient C should probably be thought of as a molecular coefficient, not a material constant. One

would expect that for linear polyethylene, the elongation and orientation of chains would occur more readily than for a branched polyethylene, resulting in enhanced crystallization rates. On the other hand, the presence of branching can lead to entanglements which will increase the F_{rheo} and hence the stress, perhaps leading to enhanced crystallization rates. As seen in Figure 36, the LL3.9 resin exhibits higher stress for any given take-up velocity.

Generally, short chain branching (SCB) distribution is thought to have negligible effect on melt rheology. LL3.9 has a much more complex SCB distribution than either LLP or LL4.3. According to its ATREF curve, the LL3.9 resin possesses chain molecules which can be dissolved at temperatures as low as 32 °C. This suggests that the branching must be quite complicated. However LLDPE's have primarily short chain branching which could not provide the needed entanglements which would produce the higher spinline forces and stress observed for this resin.

Both spinline and quiescent crystallization behavior was different for the LL3.9, LLP, and LL4.3 resins studied in this project. Their melt indices and M_w were quite close, however the densities were quite different. Density was shown to be controlled by the amount and distribution of branching. This branching should effect the stress enhanced crystallizability of a polymer just as it effects the isothermal and non-isothermal crystallization kinetics of the resins studied in this report.

Recall that the stress enhancement term present in the

crystallization kinetic equation is written as $CT^2f_a^2$ where f_a is a measure of amorphous orientation. However the same value of f_a for a branched and a linear molecule will represent different structures in the melt. A branched polymer does not lose its side chains simply because orientation exists. Therefore it is proposed that C be represented as

$$C = C_{lin}[1 - f(\xi)] \qquad (4\text{-}31)$$

where C_{lin} represents the stress enhanced crystallization factor for a linear polymer and $f(\xi)$ represents a function dependent on some measure of branching ξ. If $f(\xi)$ is constructed such that $f(\xi) = 0$ for a perfectly linear molecule and $f(\xi) \approx 1$ for a highly branched molecule, then the term $[1 - f(\xi)]$ serves as a "branching efficiency factor," i.e. for a perfectly linear molecule, $f(\xi) = 0$ and equation (4-31) will reduce to $C = C_{lin}$. However as C cannot be determined, C_{lin} and $f(\xi)$ most certainly cannot be determined with the current melt spinning model.

CHAPTER 5

CONCLUSIONS AND RECOMMENDATIONS

Isothermal crystallization experiments demonstrated that isothermal crystallization rates were strongly influenced by the degree of branching present. Resins with extensive short chain branching possessed lower crystallization rates than did resins with low levels of branching. The crystallization behavior was modeled using Avrami's equation. The predicted isotherms were in good agreement with the experimental results except at the later stages of crystallization where secondary crystallization effects were prominent. Six of these resins had isotherms which were superposable. For four of these resins, the presence of extensive branching resulted in isotherms which were not superposable. The spherulites which developed during isothermal crystallization were typically small and poorly developed due to copolymer effects. The crystallization rate was successfully modeled as a function of temperature using an equation based on growth rate theory.

Non-isothermal crystallization experiments also showed that the crystallization rate was strongly influenced by the degree of branching present. Samples with extensive branching required more supercooling before crystallization could occur. Non-

isothermal crystallization behavior was modeled using Nakamura's model. Reasonably good agreement between predicted and experimental curves was obtained for six of these resins. Nakamura's model assumes that crystallization coefficients are obtained from superposable isotherms. Four of these resins did not exhibit superposable isotherms and the model predictions did not match the experimental results. Non-linear regression was used on non-isothermal experimental data to obtain crystallization coefficients which could predict the non-isothermal crystallization behavior. This demonstrated that Nakamura's model can provide a reasonable description of non-isothermal crystallization behavior when the proper choice of fitting coefficients are provided. It cannot however predict the crystallization behavior in the later stages of crystallization.

Melt spinning of LLDPE's could be accomplished only over a narrow range of spinning speeds due to cohesive fracture. Melt spinning experiments demonstrated that significant differences in spinline behavior between the resins were present even though the melt indices were similar. The lowest density resin (LL3.9) exhibited a higher diameter and lower temperature than the other resins in the lower regions of the spinline. On-line tension measurements showed that the LL3.9 resin had a greater terminal tension than the other resins. The as-spun crystallinities showed no change with changing spinning conditions.

The spinline results were analyzed by the CCT approach.

This approach illustrated that stress enhanced the crystallization rate in all cases. In some cases, an increase in spinning speed delayed the onset of crystallization. For these cases, the cooling rate in the upper part of the spinline is more significant than stress and the onset of crystallinity will be delayed. Further down the spinline, temperature gradients between the fiber and the environment are smaller. In this region, the higher stresses present are more significant than cooling rate in influencing crystallization kinetics.

Elongation viscosities and heat transfer coefficients were obtained using an inversion procedure. The elongational viscosities were different for each resin and was highest in the LL3.9 resin. The heat transfer coefficients were slightly different when compared to those reported before.

Spinline model predictions showed the general features that were observed experimentally; however, the model could not accurately predict the initial diameter drawdown profile unless it was forced to. These discrepancies were attributed to over-simplifications in the spinline model.

Although this research project has not answered all of the questions it set out to, it has highlighted the areas of research where future efforts should be directed. The isothermal experiments showed that the overall crystallization behavior was strongly influenced by branching. Resins having a broad distribution of branch lengths crystallized at a slower rate than

slightly branched resins. These resins also exhibited crystallization isotherms which had a different shape than did those from slightly branched resins. An understanding of the effect of branching and the distribution of branches on nucleation and growth mechanisms would be beneficial in interpreting the isothermal and non-isothermal crystallization results that were obtained.

Concerning the melt spinline model, the assumption of a Newtonian fluid is clearly not adequate if an accurate description of spinline dynamics and crystallization is to be obtained. The resin needs to be modeled as a viscoelastic fluid if precise results are desired. No fundamental knowledge exists as to the effect of a development of crystallinity on the elongational viscosity. This has been shown to be a serious problem which also requires attention.

REFERENCES

REFERENCES

1. Glover, H.R., in "Modern Plastics Encylopedia," R.J. Martino, Ed.,McGraw-Hill, New York (1986-1987).

2. Johle, R.J., in "Modern Plastics Encylopedia," R.J. Martino, Ed., McGraw-Hill, New York (1986-1987).

3. Bai, C.C., Ph.D. Dissertation, University of Tennessee-Knoxville, 1984.

4. Bheda, J.H., Ph.D. Dissertation, University of Tennessee-Knoxville, 1987.

5. Chen, S., Yu, W., and J.E. Spruiell, J. Appl. Polym. Sci., **34**, 1477 (1987).

6. Dees, J.R., Ph.D. Dissertation, University of Tennessee-Knoxville, 1974.

7. Dees, J.R. and J.E. Spruiell, J. Appl. Polym. Sci., **18**, 1053 (1974).

8. Lambach, J.L., M.S. Thesis, University of Tennessee-Knoxville 1988.

9. Li, X., M.S. Thesis, University of Tennessee-Knoxville, 1987.

10. Lu, F. and J.E. Spruiell, J. Appl. Polym. Sci., **34**, 1541 (1987).

11. Spruiell, J.E. and J.L. White, in "Fiber and Yarn Processing," J.L. White, Ed., Appl. Polym. Symp.. **27**, 121 (1975).

12. Spruiell, J.E. and J.L. White, Polym. Eng. Sci., **15**, 660 (1975).

13. White, J.L. and J.F. Roman, J. Appl. Polym. Sci., **20**, 1005 (1976).

14. Zhou, J., M.S. Thesis, University of Tennessee-Knoxville, 1988.

15. Zieminski, K.F., Ph.D. Dissertation, University of Tennessee-Knoxville, 1986.

16. Choi, K.J., Spruiell, J.E., and J.L. White, J. Poly. Sci., Polym. Phys., **20**, 27 (1982).

17. Shimomura, Y., Spruiell, J.E., and J.L. White, J. Appl. Polym. Sci., **27**, 2663 (1982).

18. Shimomura, Y., Spruiell, J.E., and J.L. White, Polym. Eng. Rev., **2**, 418 (1983).

19. Ashizawa, H., Spruiell, J.E., and J.L. White, Polym. Eng. Sci., **24**, 1035 .(1984).

20. Bheda, J.H. and J.E. Sprueill, Polym. Eng. Sci., **26**, 736 (1986).

21. "Encyclopedia of Chemical Technology, 3rd Edition," Kirk and Ottmer, Eds., **16** 385-401, Wiley, New York (1981).

22. Frenkel, J., J. Physics, **1**, 315, (1939).

23. Turnbull, D. and J.E. Fisher, J. Chem Physics, **17**, 71 (1949).

24. Sharples, A., "Introduction to Polymer Crystallization", St. Martin's Press, New York (1966).

25. Hoffman, J.D. and J.I. Lauritzen, J. Res. Natl. Bur. Stds., **65A**, 297 (1961).

26. Price, F.P., in "Nucleation," Zettlemayer, Ed., Marcel and Dekker, New Yo-k (1969).

27. Mandelkern, L., Quinn, F.A., and P.J. Flory, J. Appl. Phys., **25**, 830 (1954).

28. Cormia, R.L., Price, F.P. and D. Turnbull, J. Chem Phys., **20**, 411 (1952).

29. Turnbull, D., J. Chem. Phys., **20**, 411 (1952).

30. Hoffman, J.D. and J.J. Weeks, J. Chem. Phys., **37**, 1721 (1962).

31. Williams, M.L., Landel, R.F., and J.D. Ferry, J. Amer. Chem. Soc., **77**, 3701 (1955).

32. Bassett, D.C., "Principles of Polymer Morphology," Cambridge University Press, Oxford (1981).

33. Hoffman, J.D., Frolen, L.J., Ross, G.S., and J.L. Lauritzen Jr., J. Res. Natl. Bur. Stand., Sect. A, **79**, 671 (1975).

34. Jackson, J.F. and L. Mandelkern, "Analytical Calorimetry," **1**, Johnson, J.F. and R.S. Porter, Eds., Plenum Press, New York (1968).

35. Voight-Martin, I.G., Mandelkern, L., and E.W. Fischer, J. Polym. Sci., Polym. Phys., **19**, 1769 (1981).

36. Hillig, W.B., Acta. Metall., **14**, 1868 (1966).

37. Mandlekern, L., Glotin, M., and R.A. Benson, Macromolecules, **14**, 22 (1981).

38. Avrami, M., J. Chem. Phys., **7**, 1103 (1939).

39. Avrami, M., J. Chem. Phys., 8, 212 (1940).

40. Avrami, M., J. Chem. Phys., 9, 177 (1941).

41. Mandelkern, L., "Crystallization of Polymers," McGraw-Hill, New York (1964).

42. Schultz, J.M., "Polymer Material Science," Prentice-Hall, New York (1974).

43. Banks, W., Hay, J.N., and A. Sharples, J. Polym. Sci., A2, 4059 (1969).

44. Takayanagi, M., Mem. Fac. Eng. Kyushu. Univ., **16**, 112, (1957).

45. Banks, W., Gordon, M., Roe, R.J. and A. Sharples, Polymer, **4**, 61 (1963).

46. Hillier, I.H., J. Polym. Sci., Pt. A, **3**, 3067 (1965).

47. Velisaris, C. and J. Seferis, Polym. Eng. Sci., **26**, 1574 (1986).

48. Price, F.P., J. Polym. Sci., Pt. A, **3**, 3079 (1965).

49. Ozawa, T., Polymer, **12**, 150 (1971).

50. Evans, U.R., Trans. Faraday Soc., **41**, 365 (1945).

51. Eder, M. and A. Wlochowicz, Polymer, **24**, 1593 (1983).

52. Nakamura, N., Katayama, K., and T. Amano, J. Appl. Polym. Sci., **17**, 1031 (1973).

53. Nakamura, N., Watanabe, T., Katayama, K. and T.Amano, J. Appl. Polym. Sci., **18**, 615 (1974).

54. Ziabicki, A., Appl. Polymer Symp., **6**, 1 (1967).

55. Ziabicki, A., "Fundamentals of Fiber Formation," Wiley, London (1976).

56. Cebe, P., Polym. Eng. Sci., **28**, 1192 (1988).

57. Hoffman, J.D., Davis, G.T., and J.I. Lauritzen, in "Treatise On Solid State Chemistry: Crystalline and Non-crystalline Solids," J.B. Hannay, Ed., **3**, Chap. 7, Plenum, New York (1976).

58. Archambault, P. and R.E. Prud'homme, J. Polym. Sci., Polym. Phys., **18**, 35 (1980).

59. Lambert, W.S., M.S. Thesis, University of Tennessee-Knoxville 1988.

60. Hammami, A., Unpublished work, University of Tennessee-Knoxville (1989).

61. Flory, P.J., J. Chem. Phys., **15**, 397 (1947).

62. Krigbaum, W.R. and R.J. Roe, J. Polym. Sci., Pt. A2, **2**, 4391 (1964).

63. Kobayashi, K. and T. Nagasawa, J. Macromol. Sci., **B4**, 331 (1970).

64. Ziabicki, A., Polimery, **18**, 615 (1973).

65. Ziabicki, A., Coll. Polym. Sci., **252**, 207 (1974).

66. Katayama, K. and M. Yoon, in "High Speed Fiber Spinning," A. Ziabicki and H. Kawai, Eds., Wiley Interscience, New York (1985).

67. Mandelkern, L., J. Phys. Chem., **75**, 3920 (1971).

68. Kawai,T. Iguchi, M. and H. Tonami, Kollid Z., **221**, 28 (1967).

69. Katayama, K., Amano, T., and N. Nakamura, Kollid Z., **226**, 125 (1968).

70. White, J.L., Polym. Eng. Rev., **1**, 297 (1981).

71. Bird, R.B., Stewart, W.E., and E.N. Lightfoot, "Transport Phenomena," John Wiley and Sons, New York (1960).

72. Hamana, I.M., Matsui, M., and S. Kato, Meilland Textil, **50**, 382 (1969).

73. Andrews, E.H., in "Fiber Structure," J.W.S. Hearle and R.H. Peters, Eds., Butterworth and the Textile Institute, Manchester, London (1962).

74. Gould, J. and F.S. Smith, J. Text. Inst., **1**, 38 (1980).

75. Sano, Y. and K. Orii, Sen. I Gakkaishi, **24**, 212 (1968).

76. Kase, S. and T. Matsuo, J. Polym. Sci., **A3**, 2541 (1965).

77. Ziabicki, A. and K. Kedzierska, Chemie Stosowana, **3**, 151 (1960).

78. Wilhelm, V.G., Kolloid Z. Z. Polym., **208**, 97 (1966).

79. Shimizu, J., Watanabe, A., and K. Toriumi, Sen. I Gakkaishi, **30**, 35 (1974).

80. Alexander, L.E., "X-ray Diffraction Methods in Polymer Science," Kreiger, Malabar, Florida (1979).

81. Stein, R.S., in "Newer Methods of Polymer Characterization," B. Ke, Ed., Interscience, New York (1964).

82. Stein, R.S. and F.H. Norris, J. Polym. Sci., **21**, 381 (1956).

83. Ishizuka, O. and K. Koyama, in "High Speed Fiber Spinning," A. Ziabicki and H. Kawai, Eds., Wiley Interscience, New York (1985).

84. Acierno, D., Dalton, J.N., Rodriguez, J.M., and J.L. White, J. Appl.Polym. Sci.,**15**, 2395 (1971).

85. Chen, I.J., Hagler, G.E., Abbott, L.E., Bogue, D.C. and J.L. White, Trans. Soc. Rheo., **16**, 473 (1972).

86. Spearhot, J.A. and A.B. Metzner, Trans. Soc. Rheo., **16**, 495 (1972).

87. Kase, S. and T. Matsuo, J. Polym. Sci., **11**, 251 (1967).

88. Gagon, D.K. and M.N. Denn, Polym. Eng. Sci., **21**, 844 (1981).

89. Yasuda, H., Sugiyama, H., and H. Yanagawa, Sen. I Gakkaishi, **35**, 370 (1979).

90. Sakiadis, B.C., Amer. Inst. Chem. Eng. J., **7**, 476 (1961).

91. George, H.H., and M.H.G. Deeg, Paper presented at the Second Annual Meeting of the Polymer Processing Society, Montreal, Canada, 1986.

92. Hajji, N., Unpublished work, University of Tennessee-Knoxville (1989).

93. Wust, C., Ph.D. Dissertation, University of Tennessee-Knoxville, 1982.

94. Mandlekern, L., NTIS Technical Report, AFML-TR-70-196, October 1970.

95. Flory, P.J., J. Chem Phys., **17**, 223 (1949).

96. Flory, P.J., Trans Faraday Soc., **51**, 848 (1965).

97. Baker, C.H., and L. Mandelkern, Polymer, **7**, 7 (1966).

98. Alamo, R., Domszy, R. and L. Mandelkern, J. Phys Chem., **88**, 6587 (1984).

99. Richardson, M.J., Flory, P.J. and J.B. Jackson, Polymer, **4**, 221 (1963).

100. Polietilen Srednego Davleniya (Medium-Pressure Polyethylene), S.V. Shchvtskii , ed., Izdael'stvo "Khimiya" (1965).

101. Sirota, A.G., Ryabikov, E.P., Gol'denberg, A.L., Il'chenko, P.A., and L.F. Chopko, Plast. Massy., **11**, 5 (1965).

102. Gol'denberg, A.L., Zapletryak, V.M., and P.A. Il'chenko, in "Spektroskopiya Polimerov," Kiev, Izdatel'stvo "Naukova Dumka" (1967).

103. Lauritzen, J.L. Jr., and J.D. Hoffman, J. Res. Natl. Bur. Std. **64A**, 73 (1960).

104. Dietz, W., Colloid Polym. Sci., **259**, 413 (1981).

105. Hillier, I.H., J. Polym. Sci., Pt. A, **3**, 3067 (1965).

106. Price, F.P., J. Polym. Sci., Pt. A, **3**, 3079 (1965).

107. Banks, W., Hay, J.N., Sharples, A. and G. Thomson, Polymer, **5**, 163 (1964).

108. Banks, W. and A. Sharples, J. Polym.Sci., Pt. A2, **2**, 4059 (1964).

109. Banks, W., Gordon, M., and A. Sharples, J. Polym.Sci., Pt. A2, **4**, 4059 (1964).

110. Banks, W. and A. Sharples, Makromol. Chem., **59**, 233 (1963).

111. Geil, P.H., "Polymer Single Crystals," Wiley-Interscience, New York (1963).

112. Smith, P. and St. John-Manley, R., Macromolcules, **12**, 483 (1979).

113. Mandelkern, L., J. Mat. Sci.,B, **6**, 615 (1968).

114. Hawkins, S.W., and H. Smith, J. Polym. Sci., **28**, 341 (1958).

115. Constantinides, A., "Applied Numerical Methods With Personal Computers," McGraw-Hill, New York (1987).

116. Tordella, J.D., Rheol. Acta, **1**, 216 (1958).

117. Bagley, E.B., Trans. Soc. Rheol., **5**, 355 (1961).

118. Han, C.D., and R.R. Lamonte, Polym. Eng. Sci., **11**, 385 (1971).

119. Han, C.D., and R.R. Lamonte, Polym. Eng. Sci., **12**, 77 (1972).

120. Mandelkern, L., Rubber Chem. Technol., **32** (1959).

121. Westover, R.F., in "Processing of Thermoplastic Materials," E.C. Bernhardt, ed., Kreiger, New York, (1974).

122. Buckley, C.P., and N.G. Crum, J. Mat. Sci., **8**, 1123 (1973).

123. Kikutani, T., Ph.D. Dissertation, Tokyo University of Technology, 1982.

124. Griskey, R.G. and G.N. Foster III, S.P.E. Ann. Tech. Conf., **26**, 546 (1968).

125. Wunderlich, B. and M. Dole, J. Polym. Sci., **24**, 201 (1957).

126. Katayama, K., Amano, T., and N. Nakamura, Appl. Polym. Symp., **20**, 237 (1973).

127. Gent, A.N., Trans. Faraday Soc., **5O**, 521 (1954).

128. Kim, H.G. and L. Mandelkern, J. Polym. Sci., A2, **6**, 181 (1968).

129 Kawai, T., Iguchi, M., and H. Tonami, Kolloid Z. Z., **221**, 28 (1968).

APPENDICES

APPENDIX A

ATREF CURVES

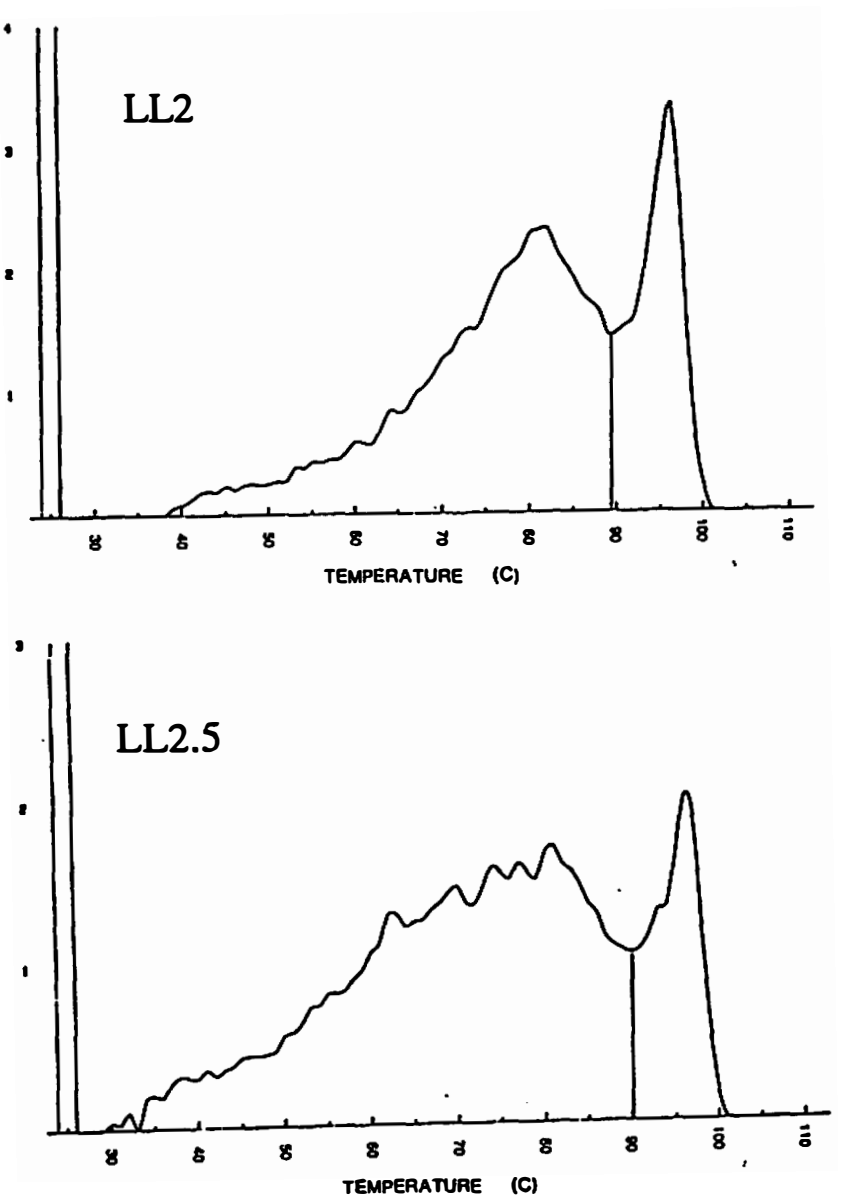

Figure A.1 LL2 and LL2.5 ATREF curves.

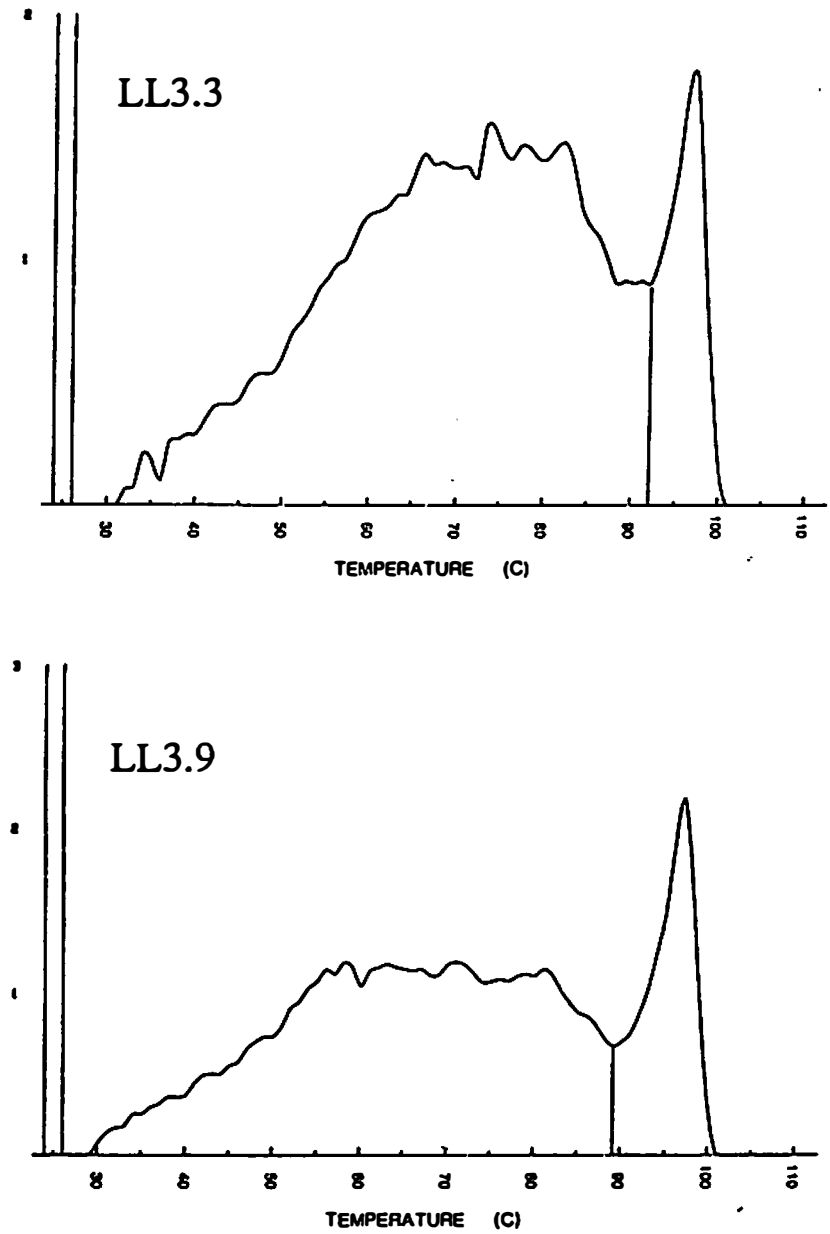

Figure A.2 LL3.3 and LL3.9 ATREF curves.

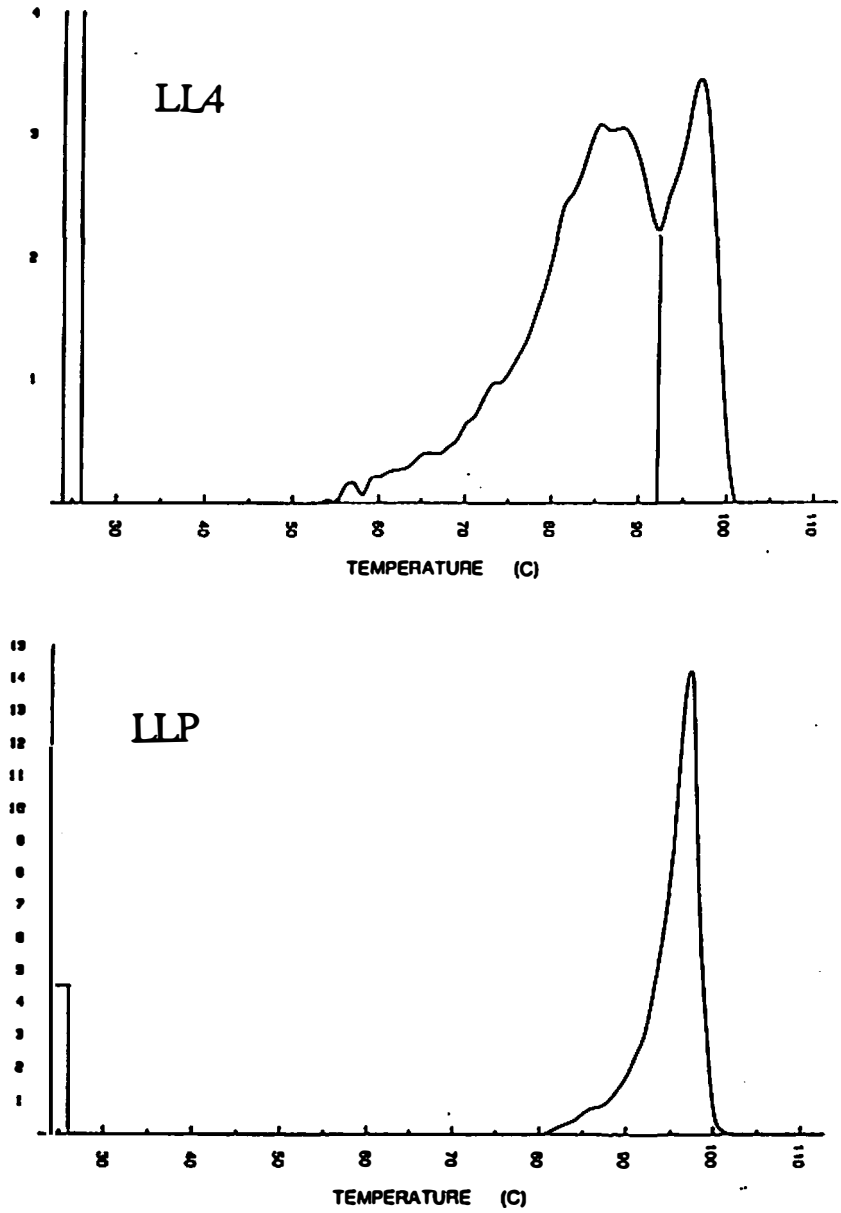

Figure A.3 LL4 and LLP ATREF curves.

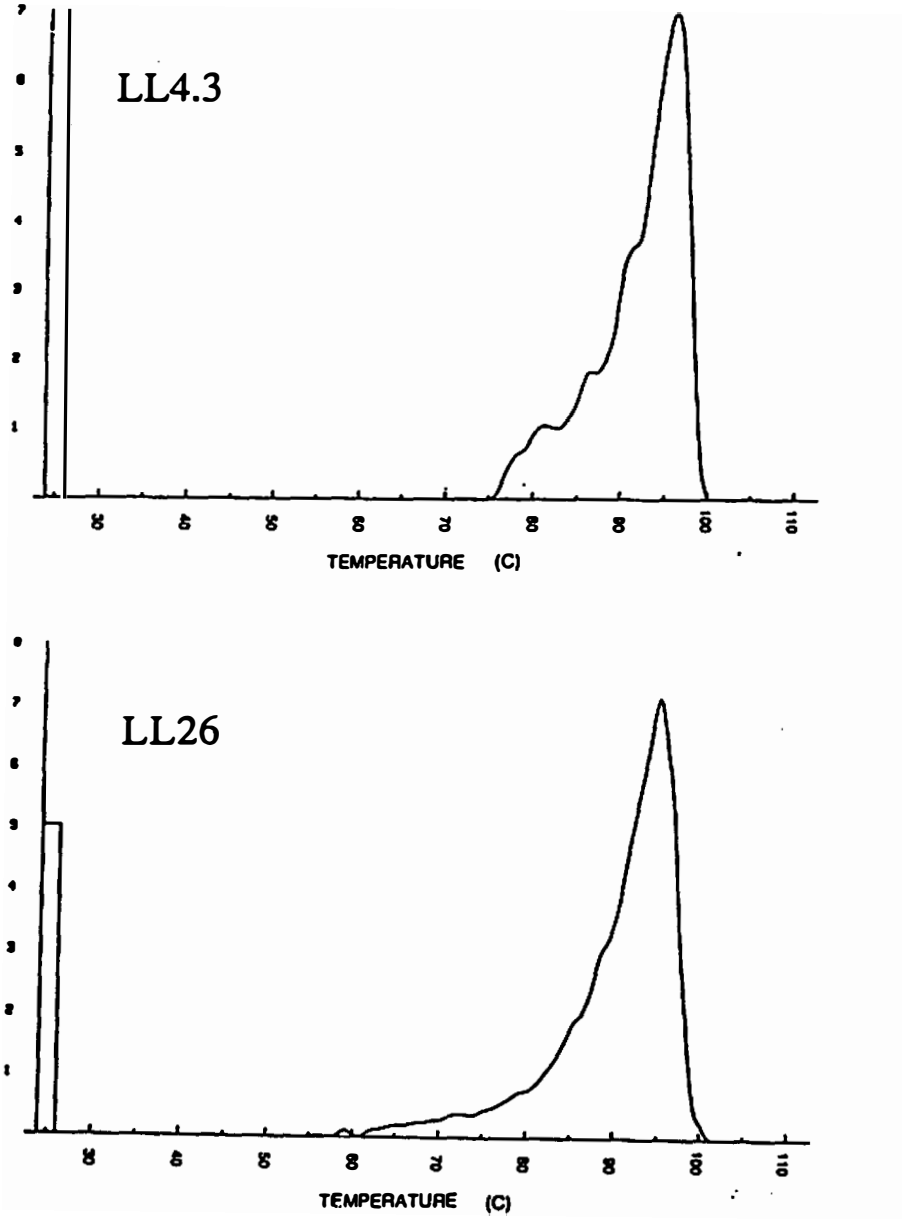

Figure A.4 LL4.3 and LL26 ATREF curves.

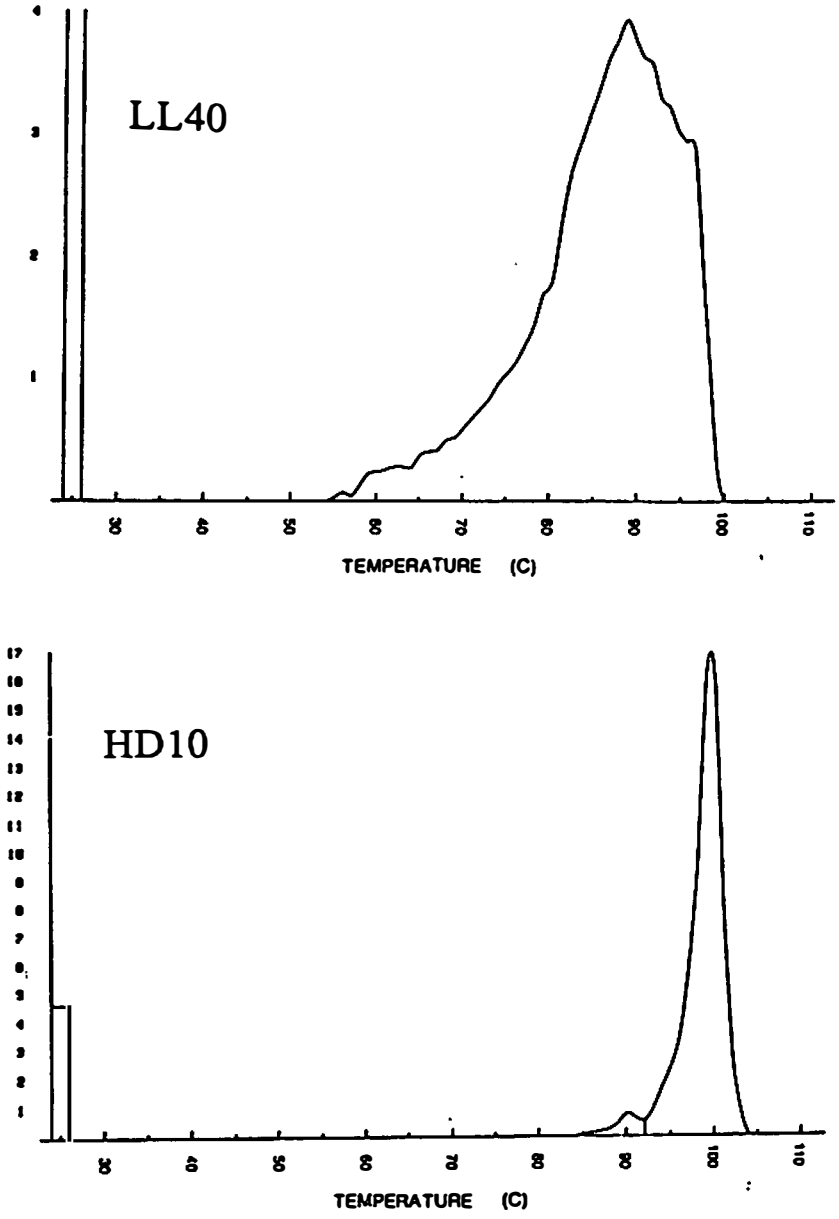

Figure A.5 LL40 and HD10 ATREF curves.

APPENDIX B

CRYSTALLIZATION ISOTHERMS AND MODEL PREDICTIONS

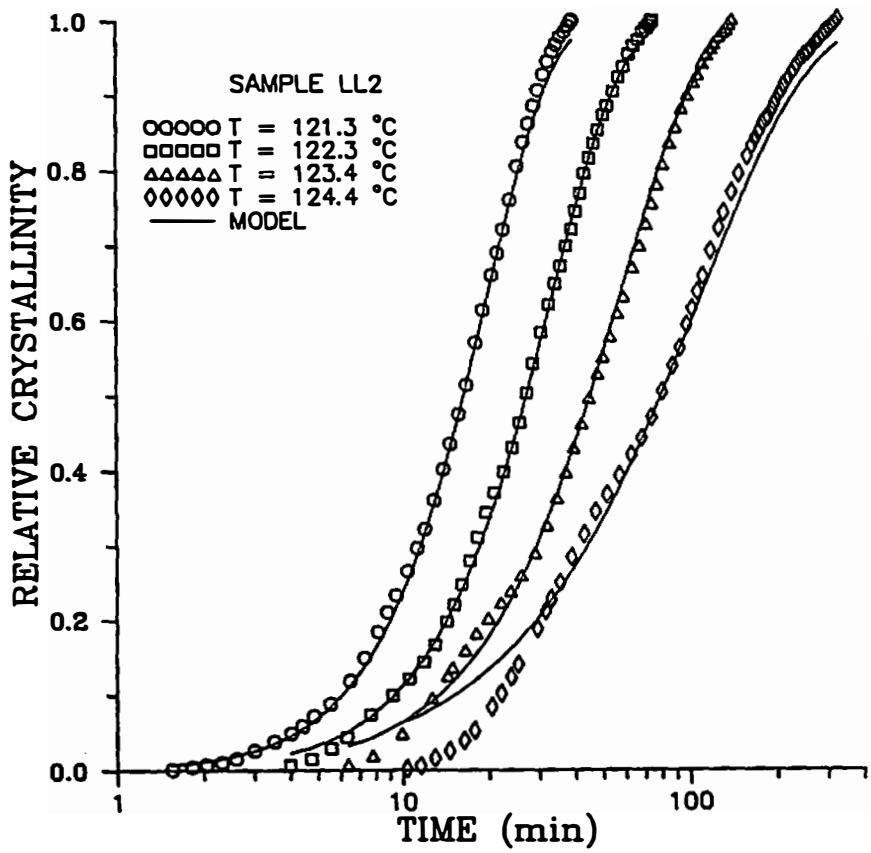

Figure A.6 LL2 crystallization isotherms and model predictions.

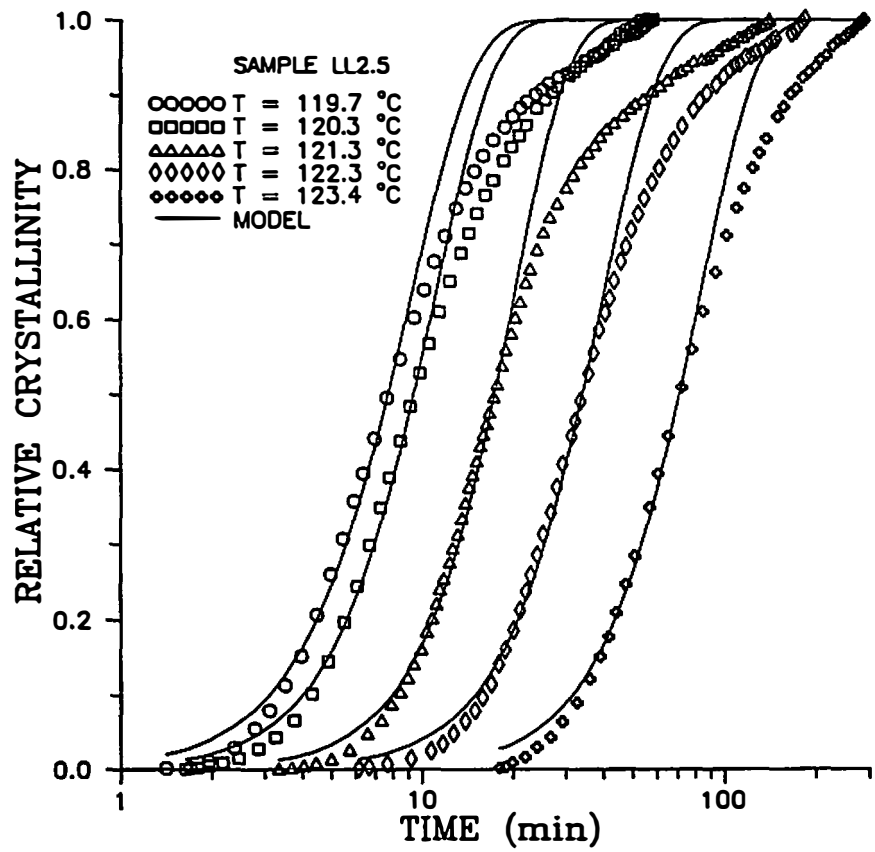

Figure A.7 LL2.5 crystallization isotherms and model predictions.

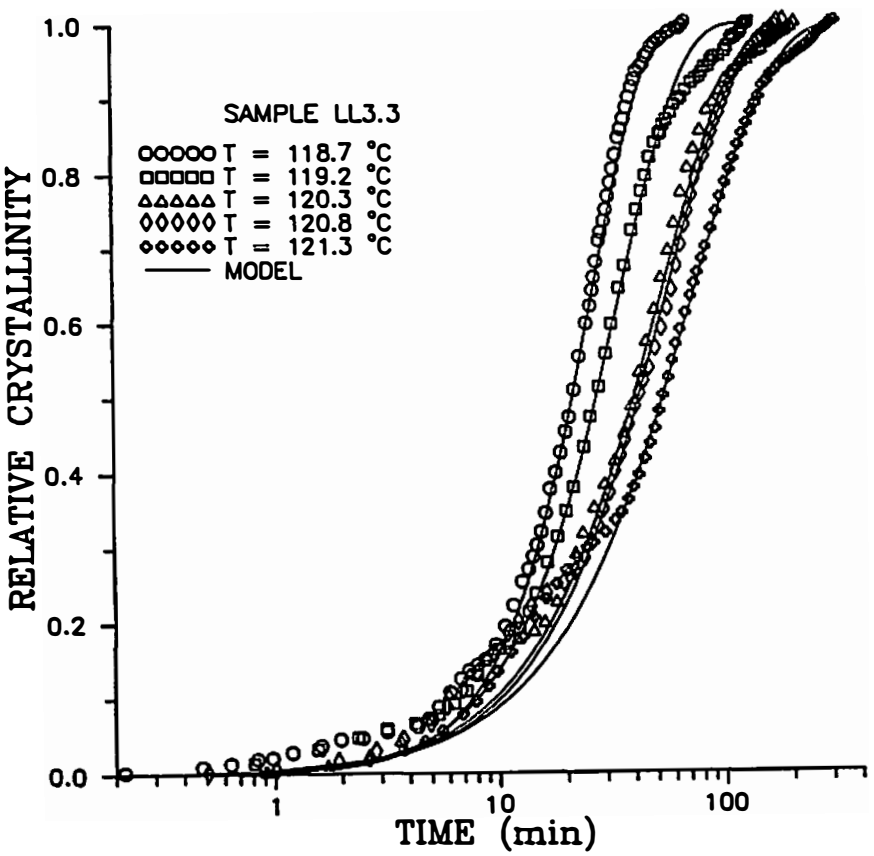

Figure A.8 LL3.3 crystallization isotherms and model predictions.

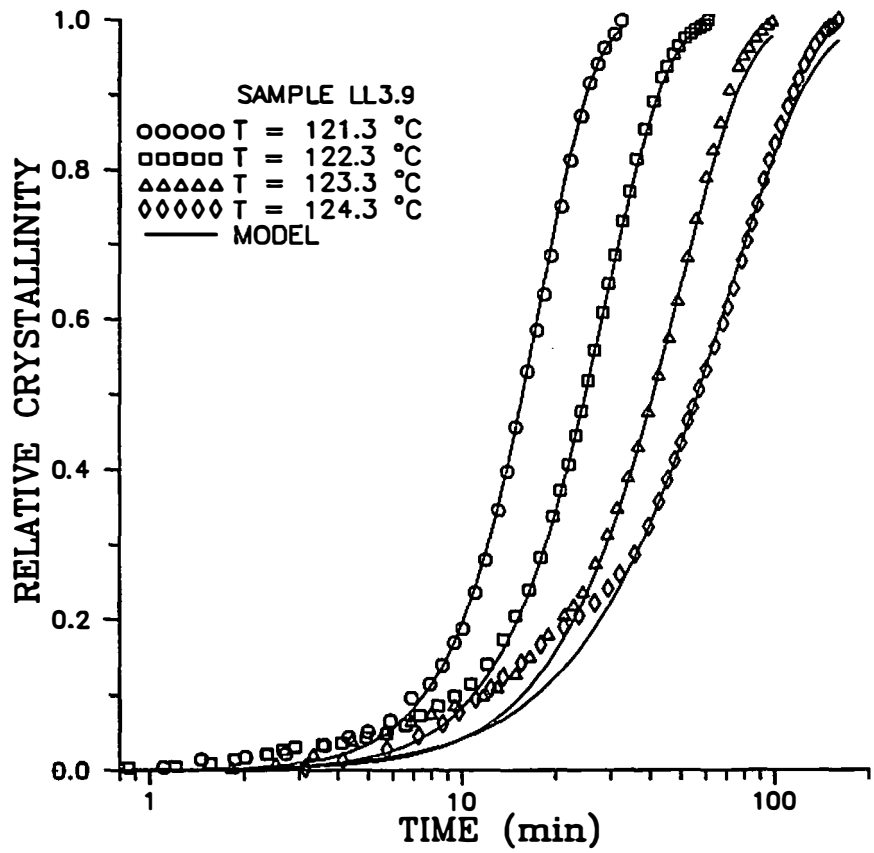

Figure A.9 LL3.9 crystallization isotherms and model predictions.

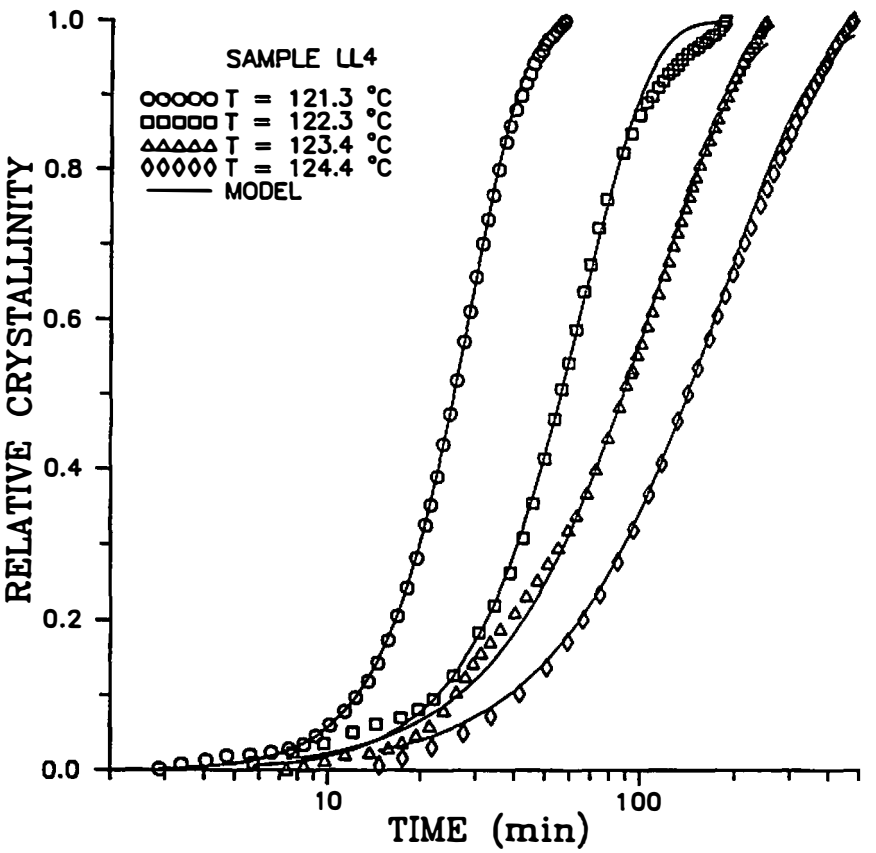

Figure A.10 LL4 crystallization isotherms and model predictions.

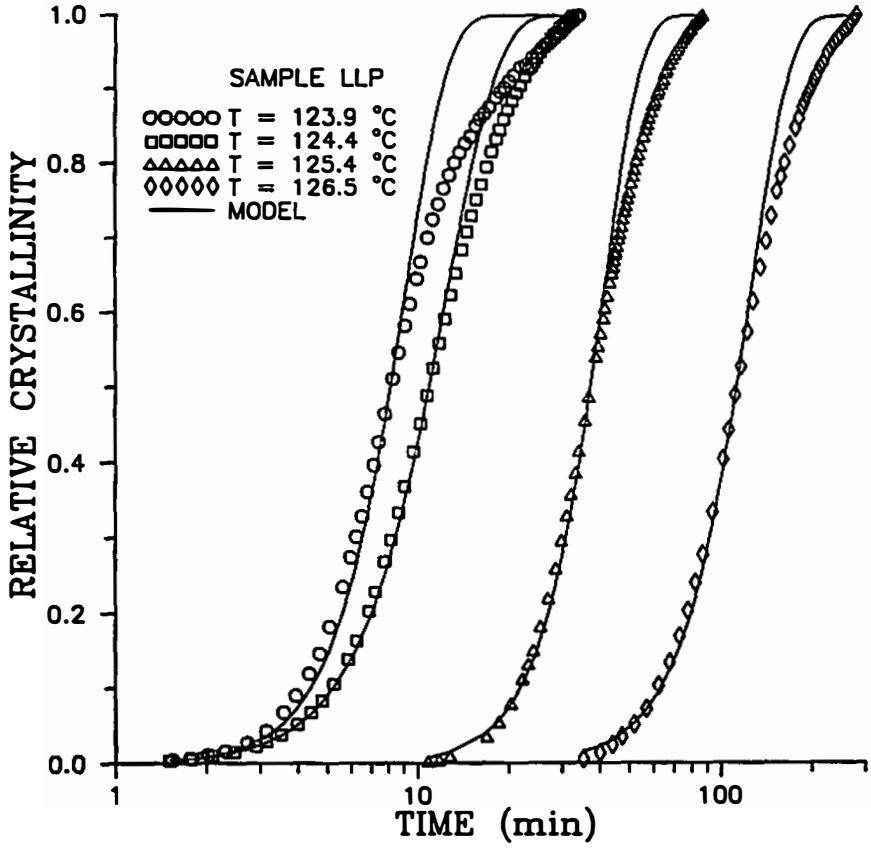

Figure A.11 LLP crystallization isotherms and model predictions.

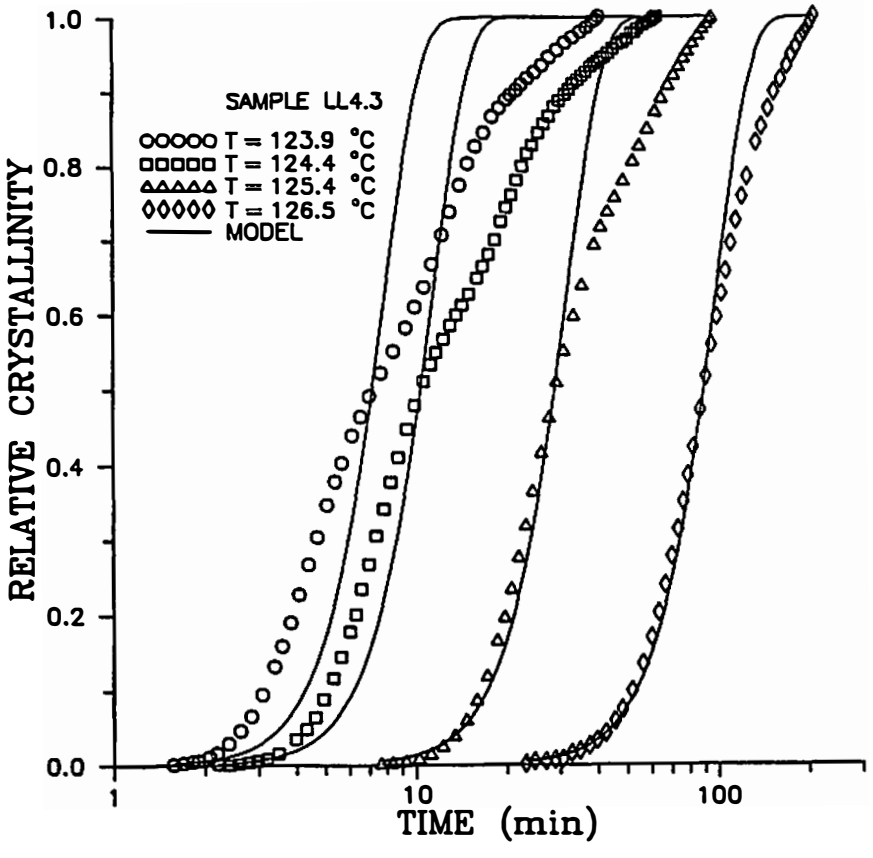

Figure A.12 LL4.3 crystallization isotherms and model predictions.

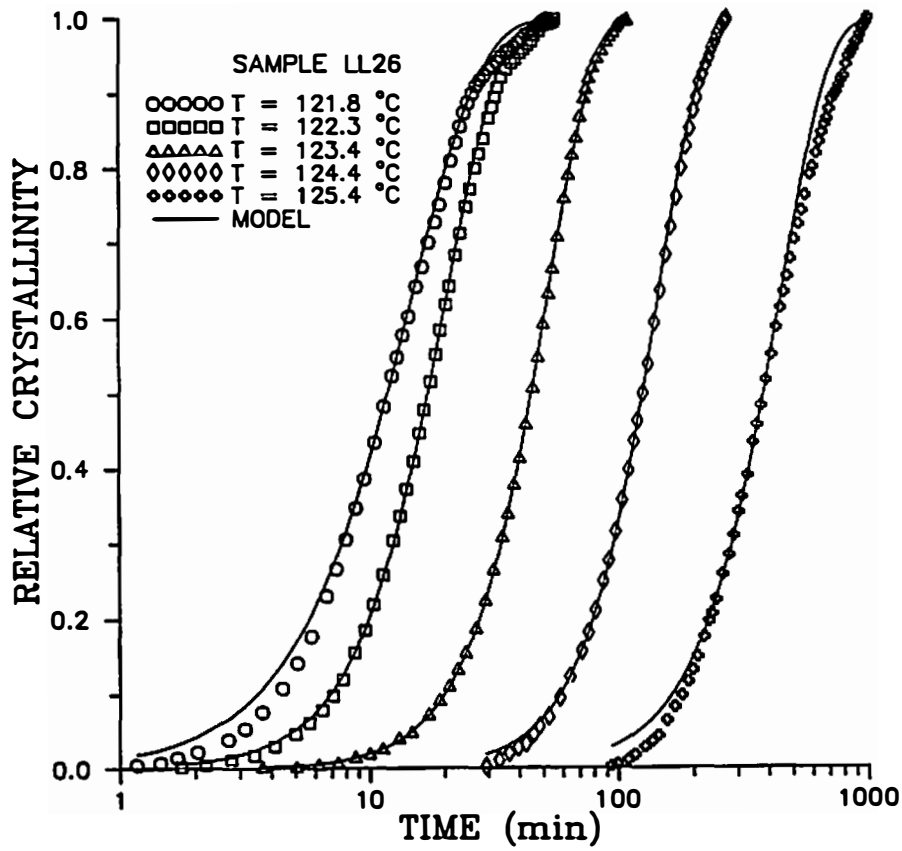

Figure A.13 LL26 crystallization isotherms and model predictions.

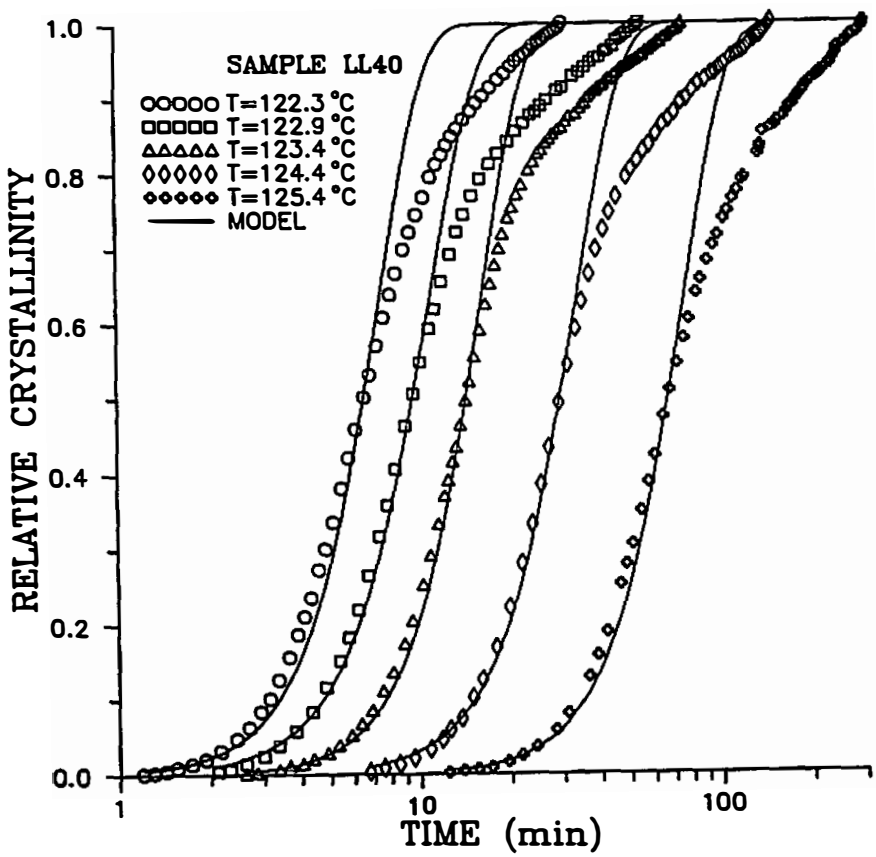

Figure A.14 LL40 crystallization isotherms and model predictions.

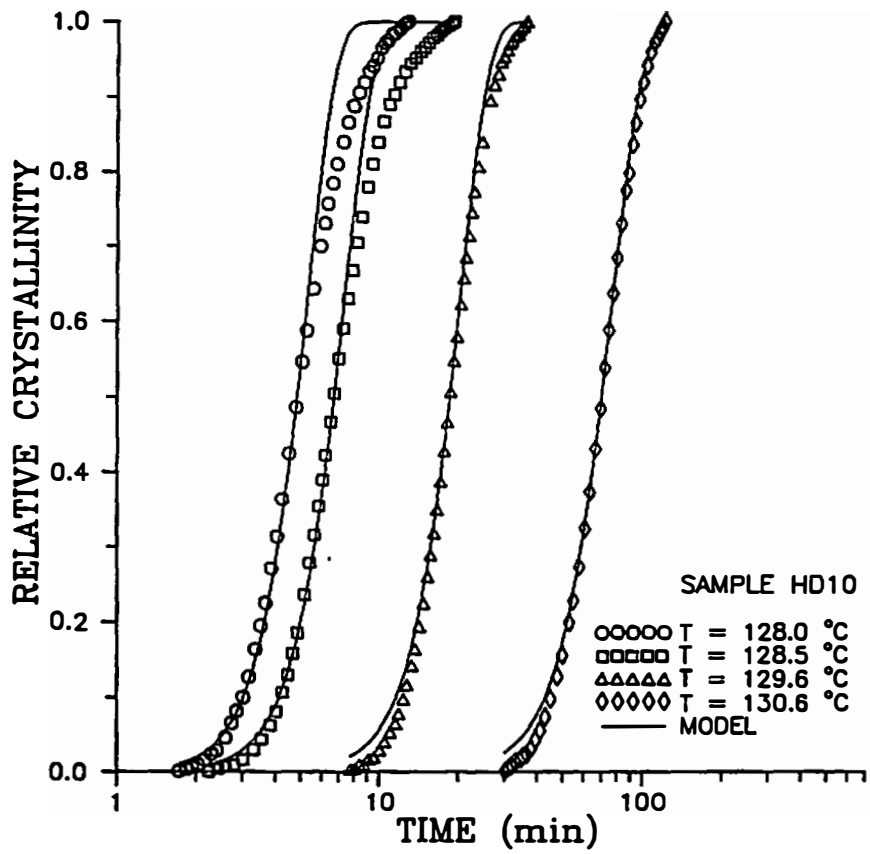

Figure A.15 HD10 crystallization isotherms and model predictions.

APPENDIX C

NON-ISOTHERMAL CRYSTALLIZATION CURVES AND PREDICTIONS

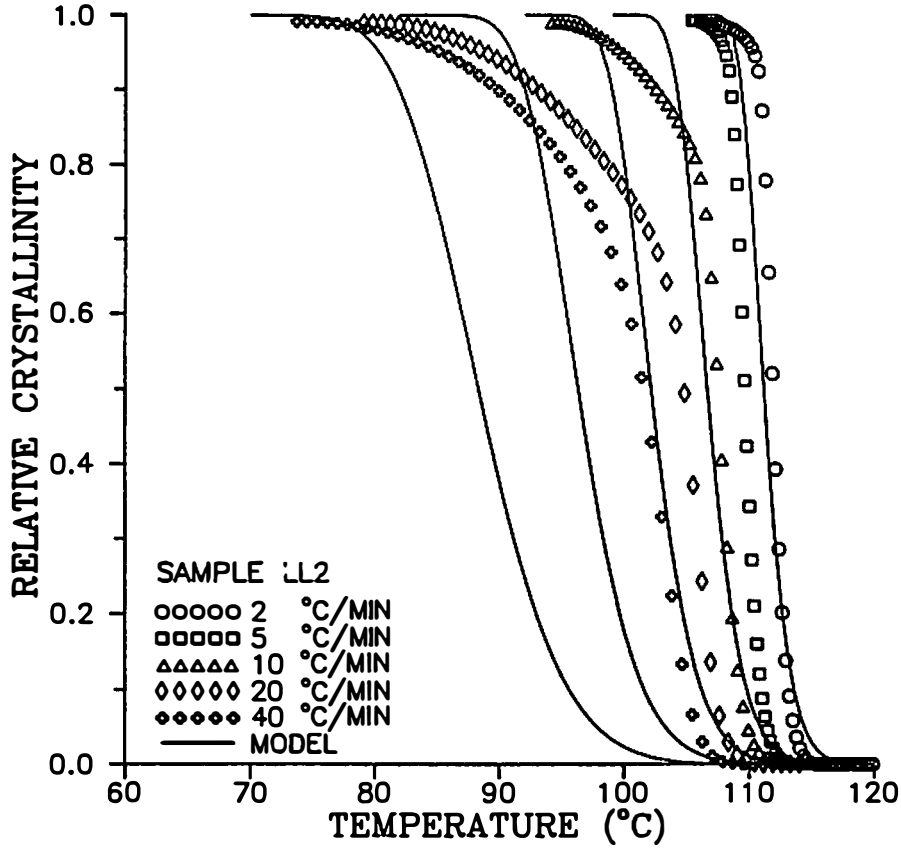

Figure A-16 LL2 non-isothermal crystallization curves and model predictions.

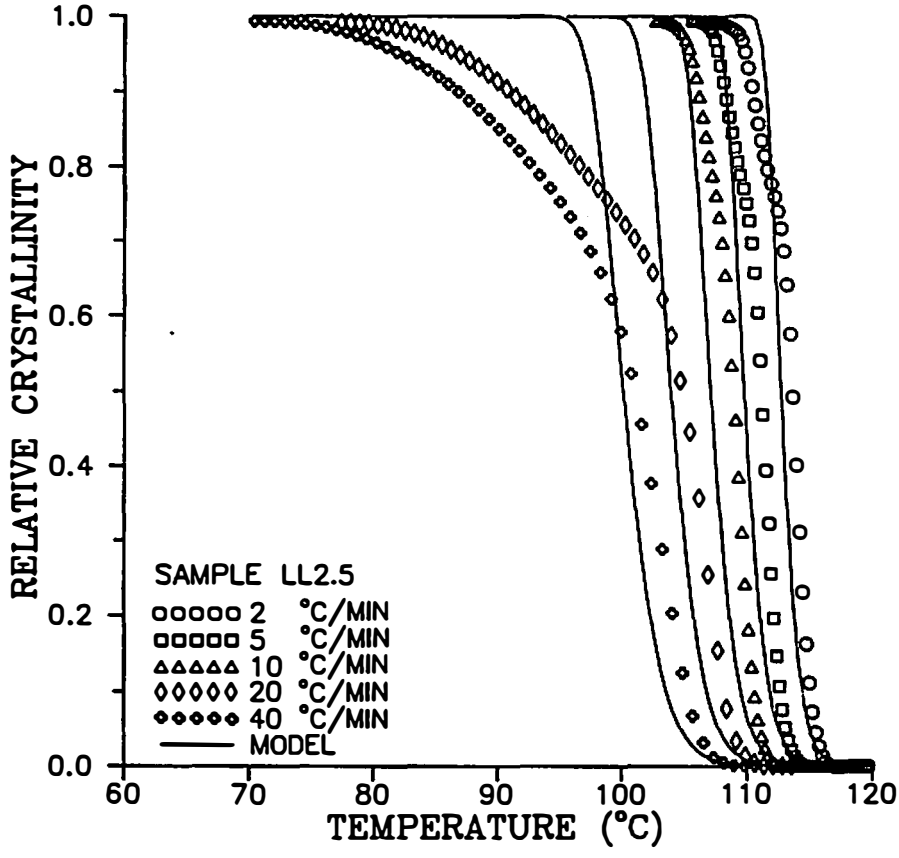

Figure A.17 LL2.5 non-isothermal crystallization curves and model predictions.

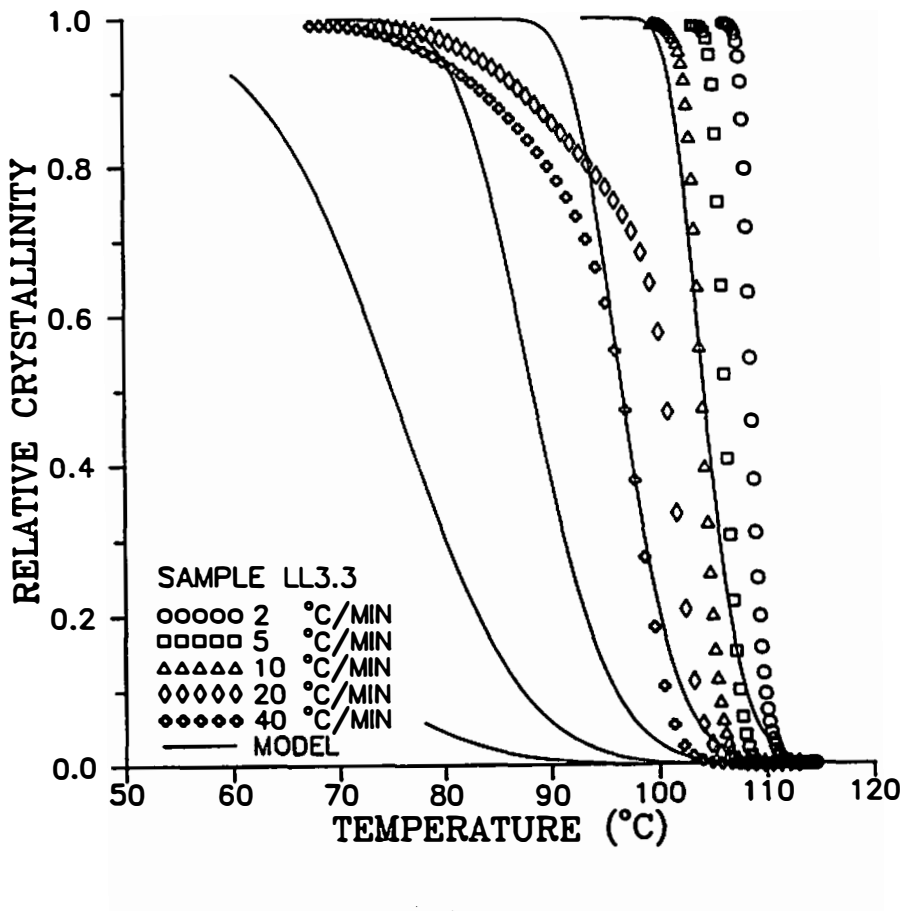

Figure A.18 LL3.3 non-isothermal crystallization curves and model predictions.

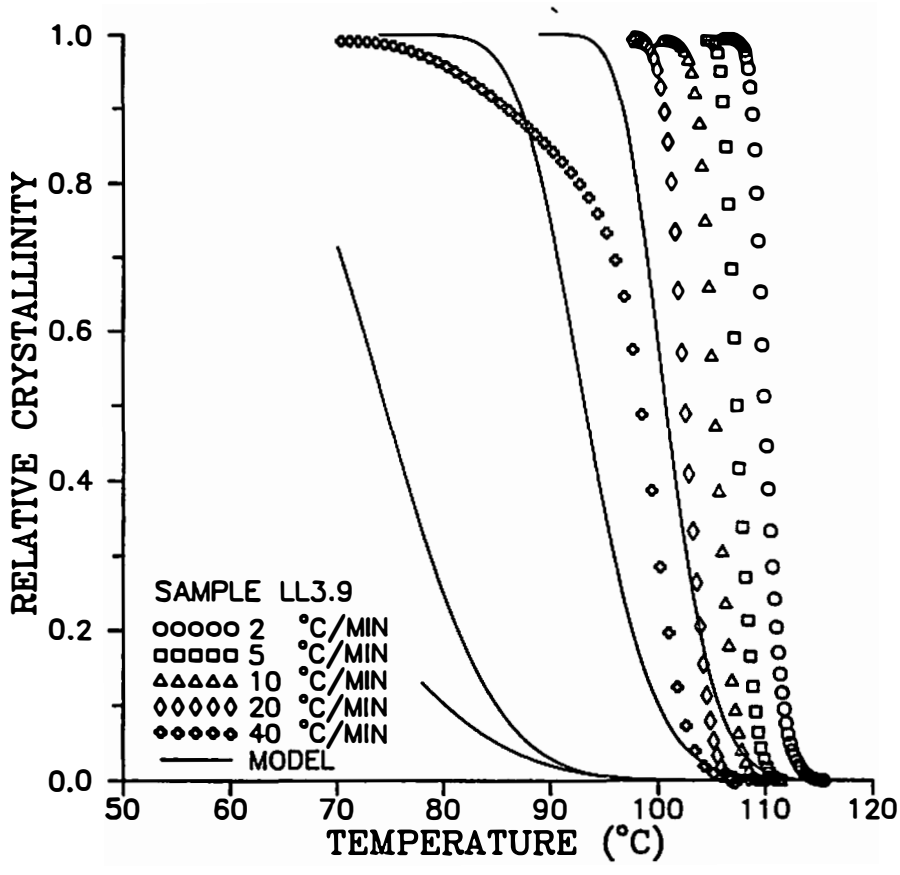

Figure A.19 LL3.9 non-isothermal crystallization curves and model predictions.

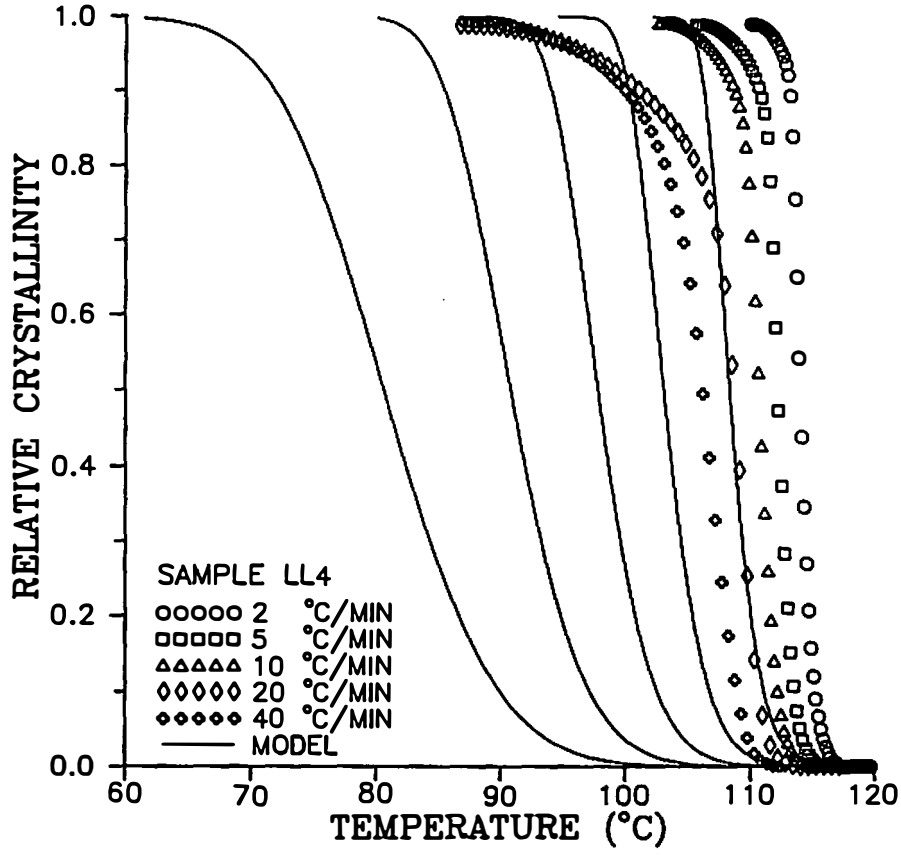

Figure A.20 LL4 non-isothermal crystallization curves and model predictions.

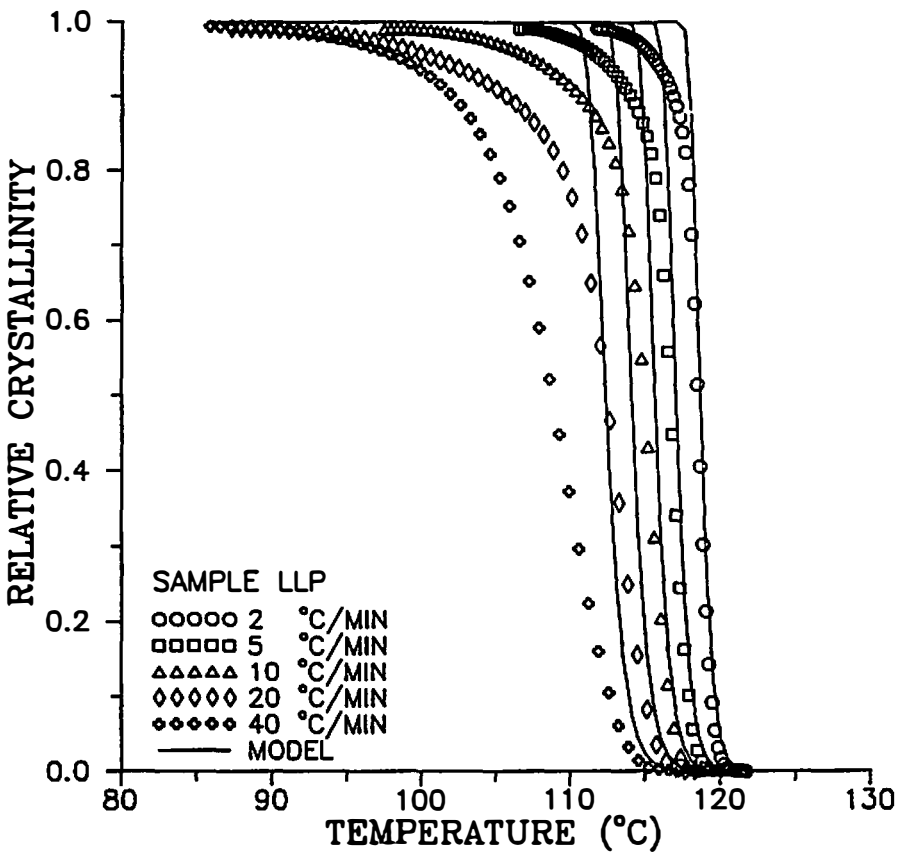

Figure A.21 LLP non-isothermal crystallization curves and model predictions.

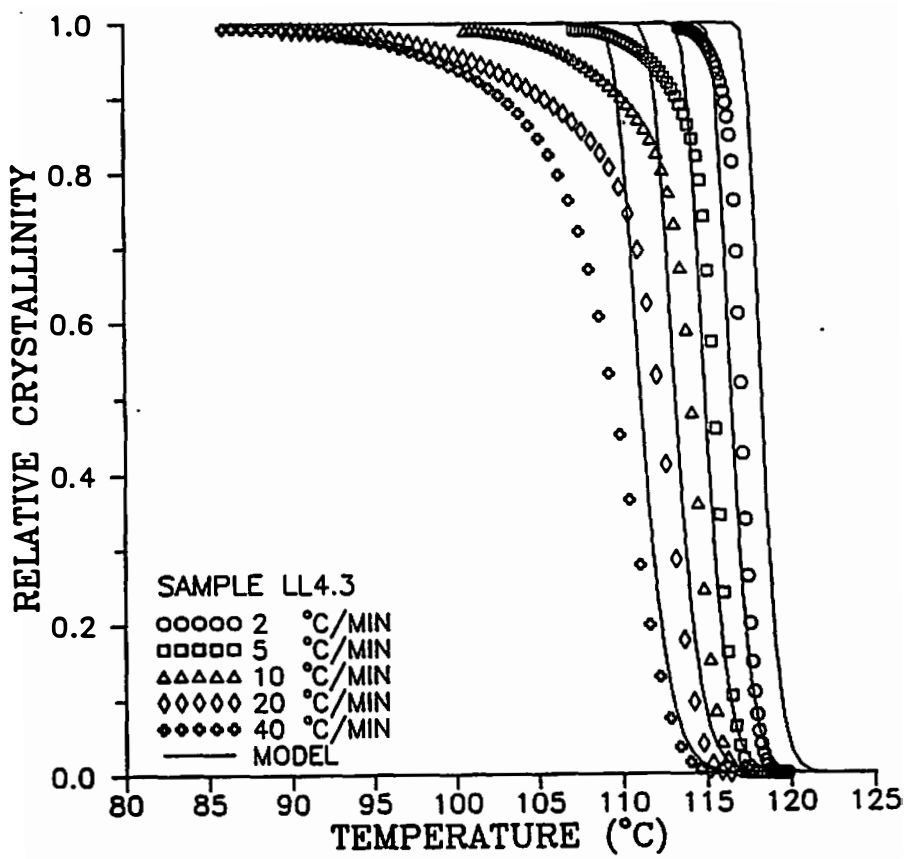

Figure A.22 LL4.3 non-isothermal crystallization curves and model predictions.

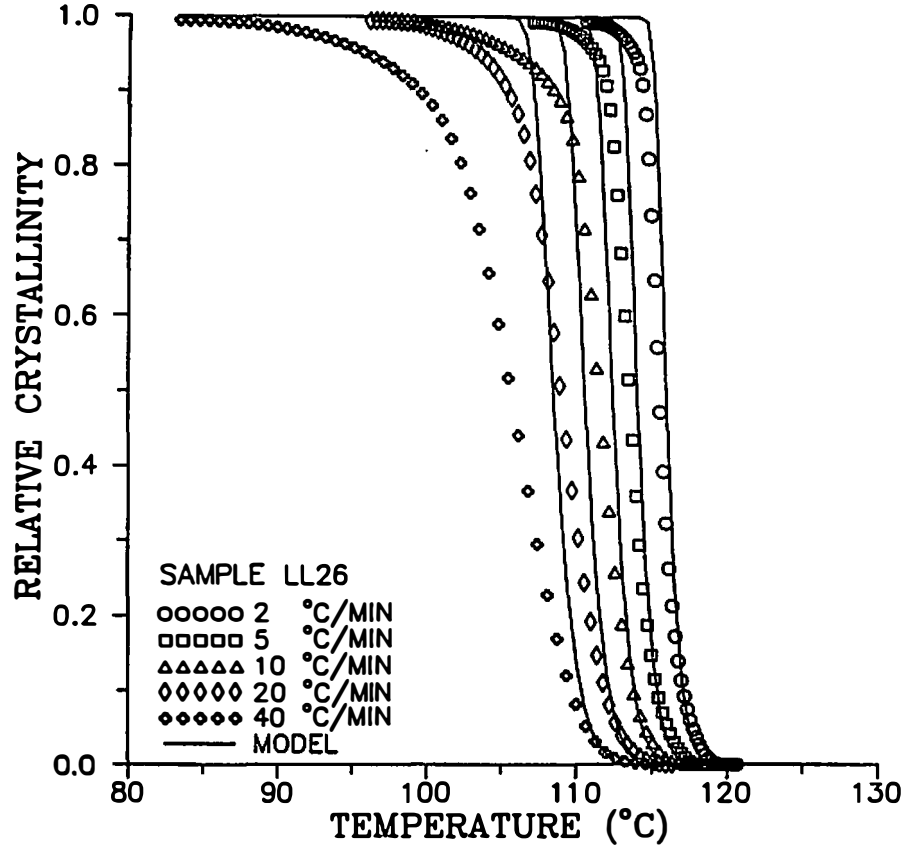

Figure A.23 LL26 non-isothermal crystallization curves and model predictions.

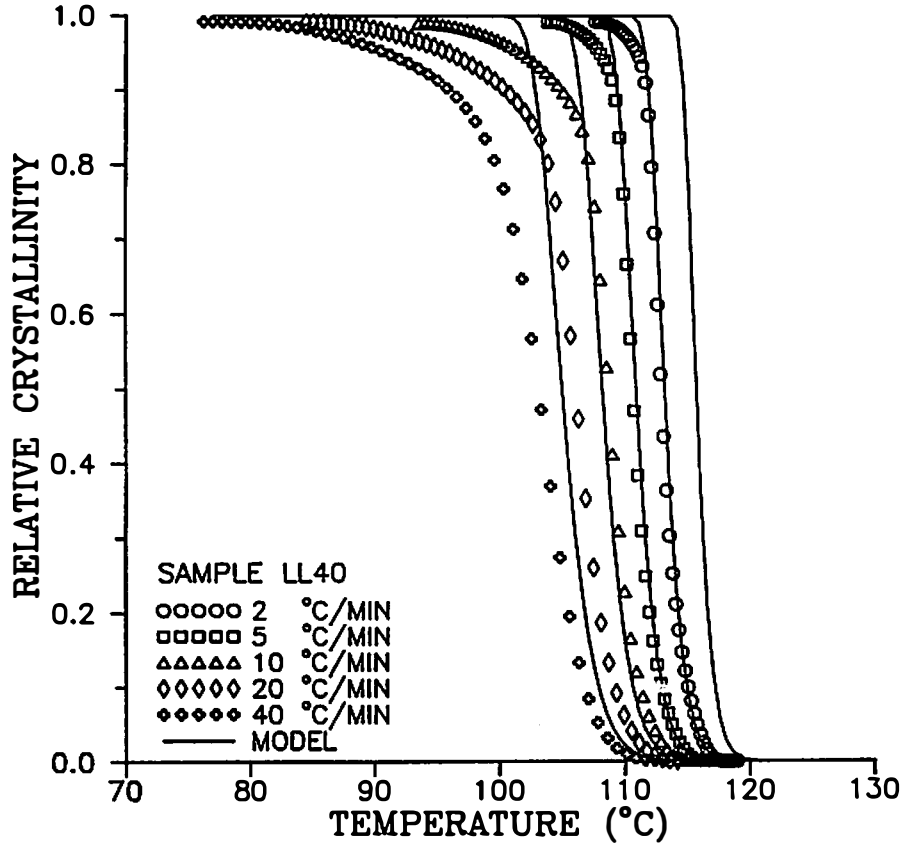

Figure A.24 LL40 non-isothermal crystallization curves and model predictions.

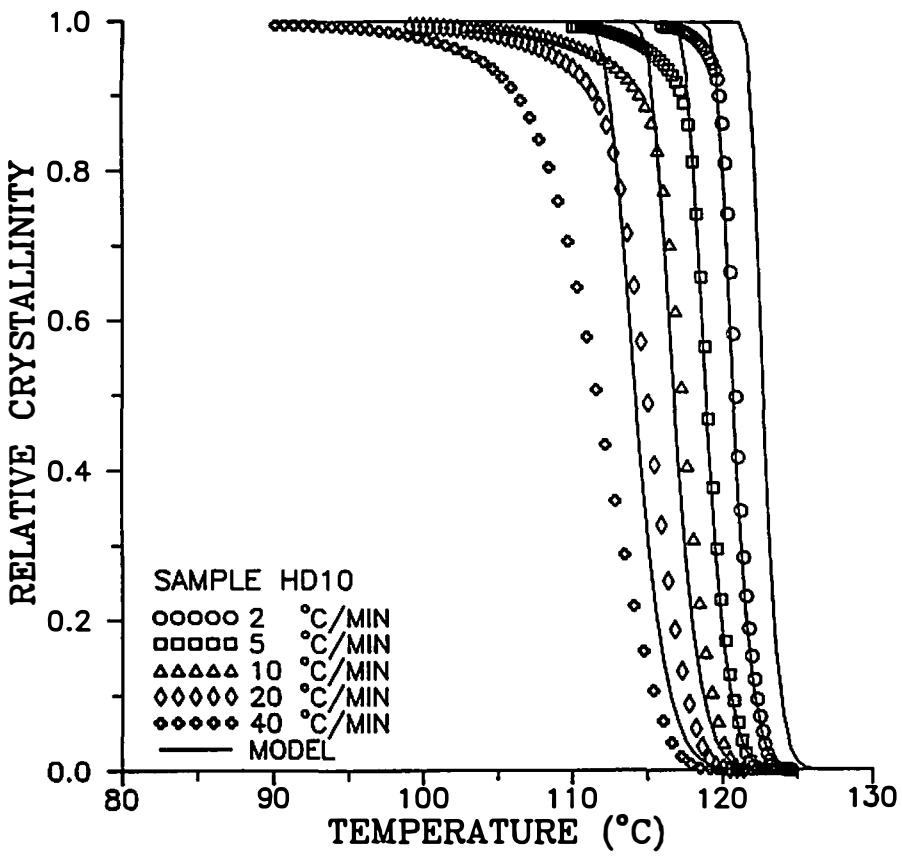

Figure A.25 HD10 non-isothermal crystallization curves and model predictions.

APPENDIX D

NON-ISOTHERMAL CRYSTALLIZATION NON-LINEAR REGRESSION PREDICTIONS

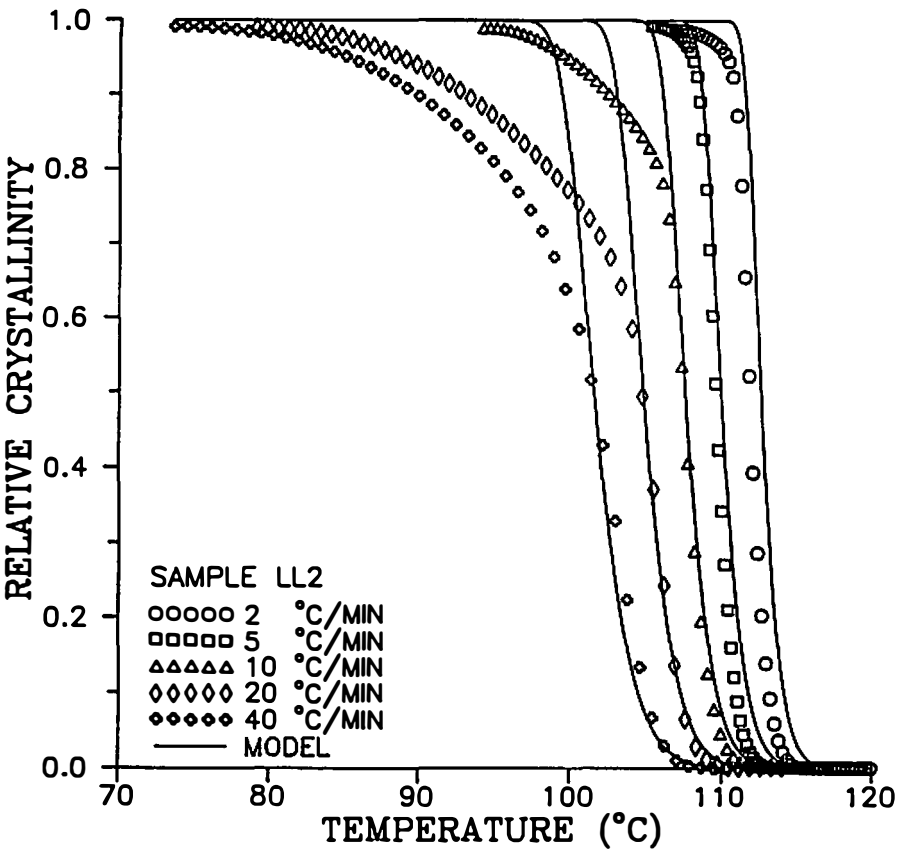

Figure A.26 LL2 non-isothermal crystallization curves and non-linear regression predictions.

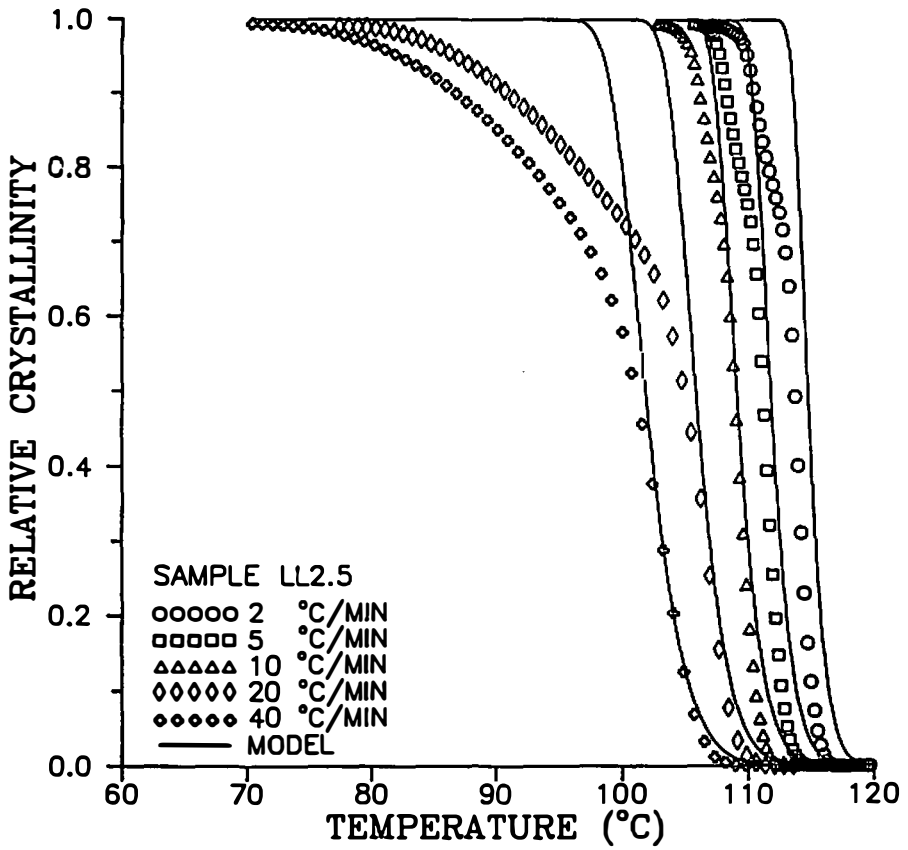

Figure A.27 LL2.5 non-isothermal crystallization curves and non-linear regression predictions.

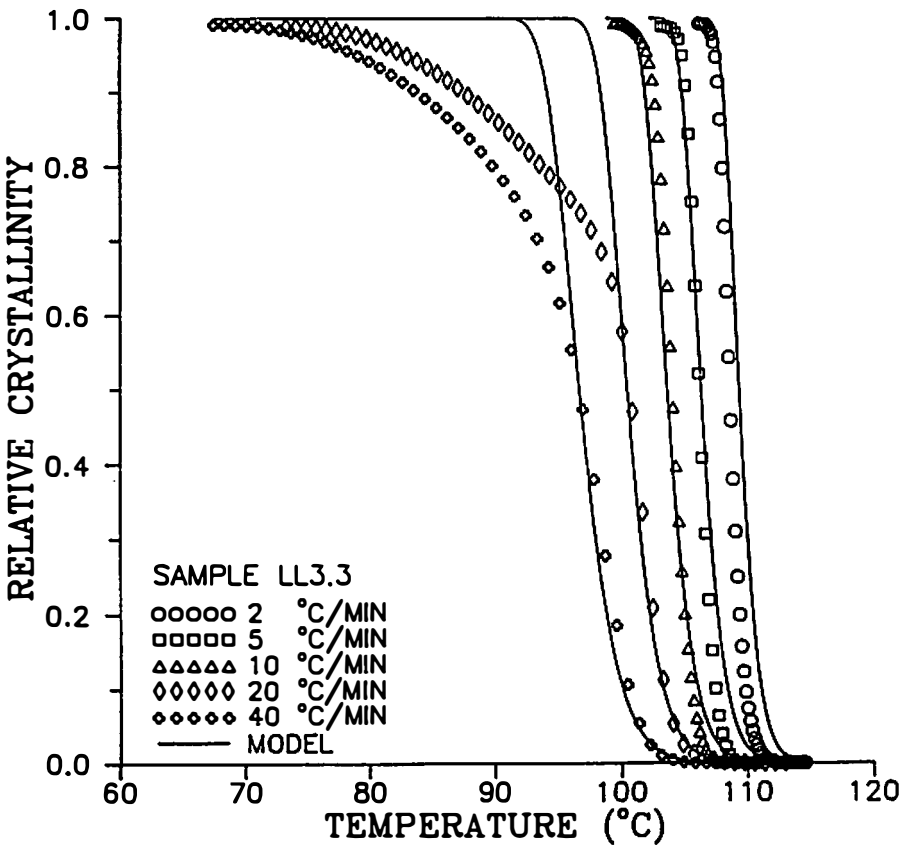

Figure A.28 LL3.3 non-isothermal crystallization curves and non-linear regression predictions.

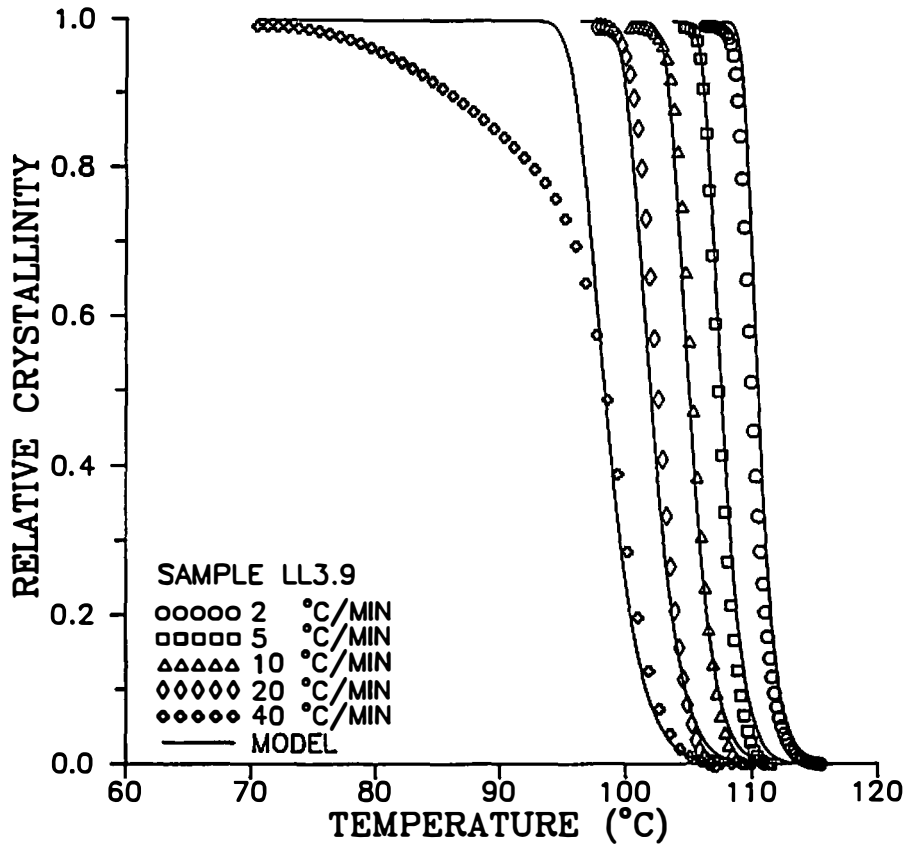

Figure A.29 LL3.9 non-isothermal crystallization curves and non-linear regression predictions.

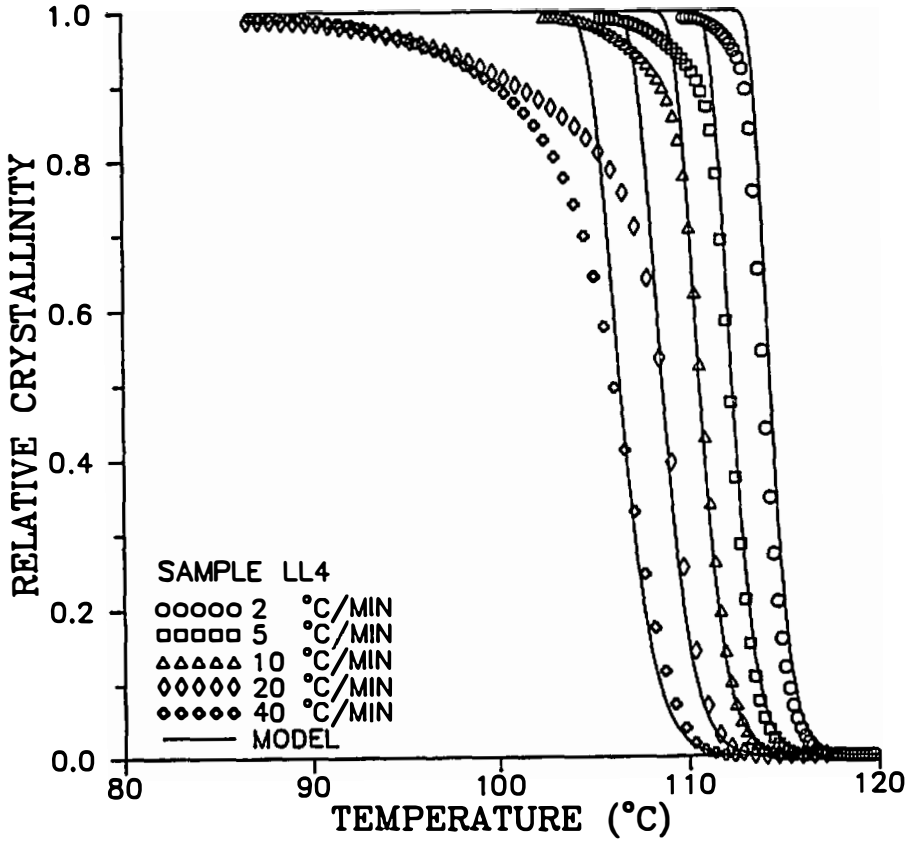

Figure A.30 LL4 non-isothermal crystallization curves and non-linear regression predictions.

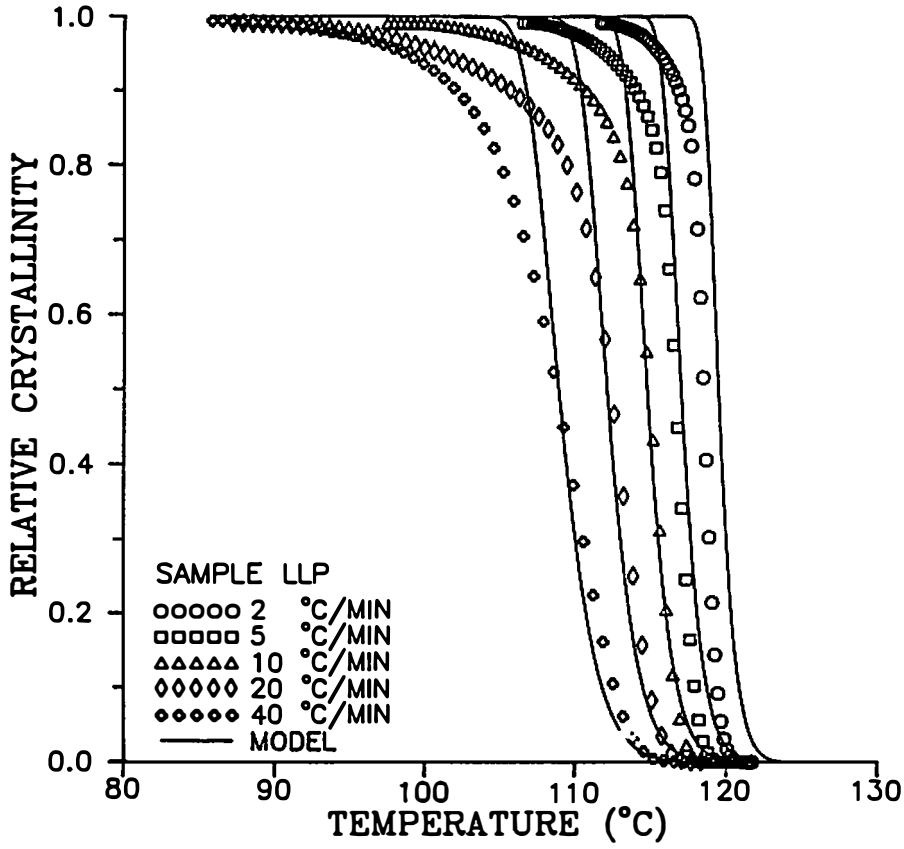

Figure A.31 LLP non-isothermal crystallization curves and non-linear regression predictions.

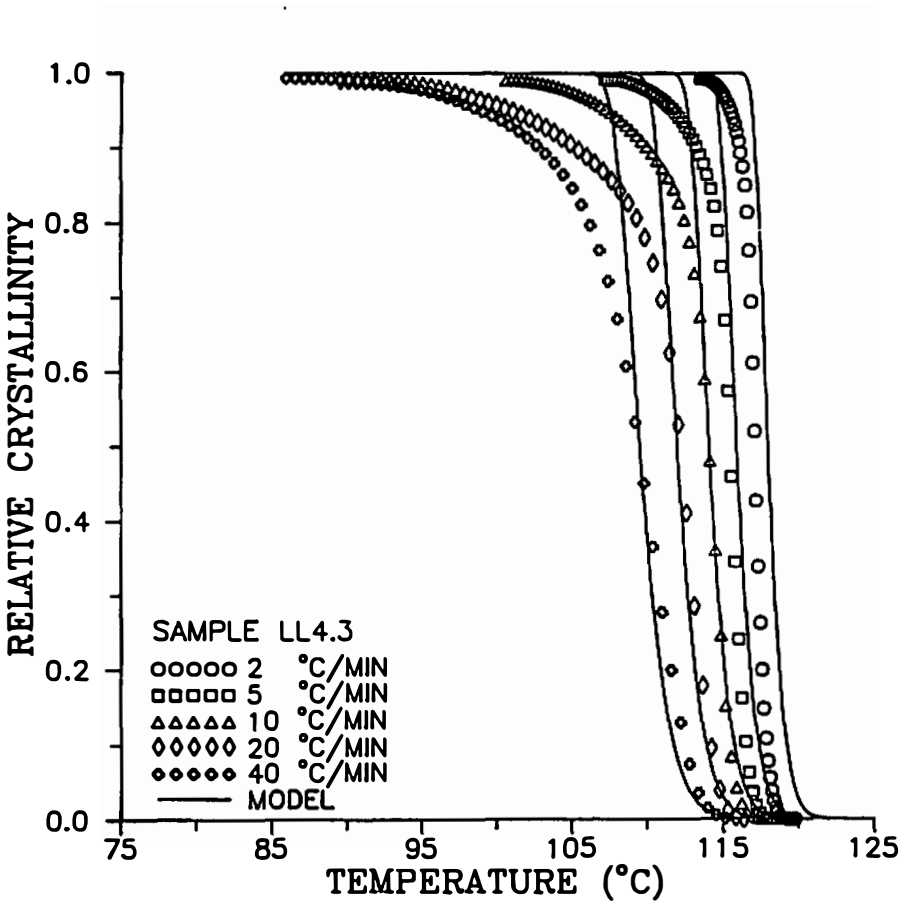

Figure A.32 LL4.3 non-isothermal crystallization curves and non-linear regression predictions.

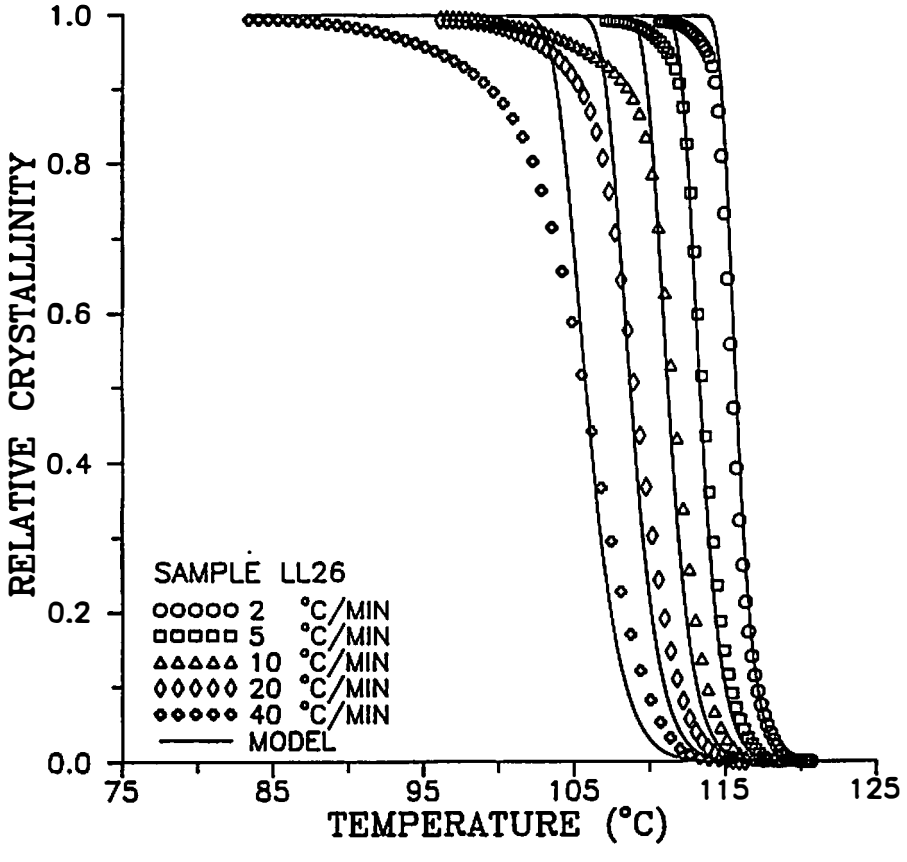

Figure A.33 LL26 non-isothermal crystallization curves and non-linear regression predictions.

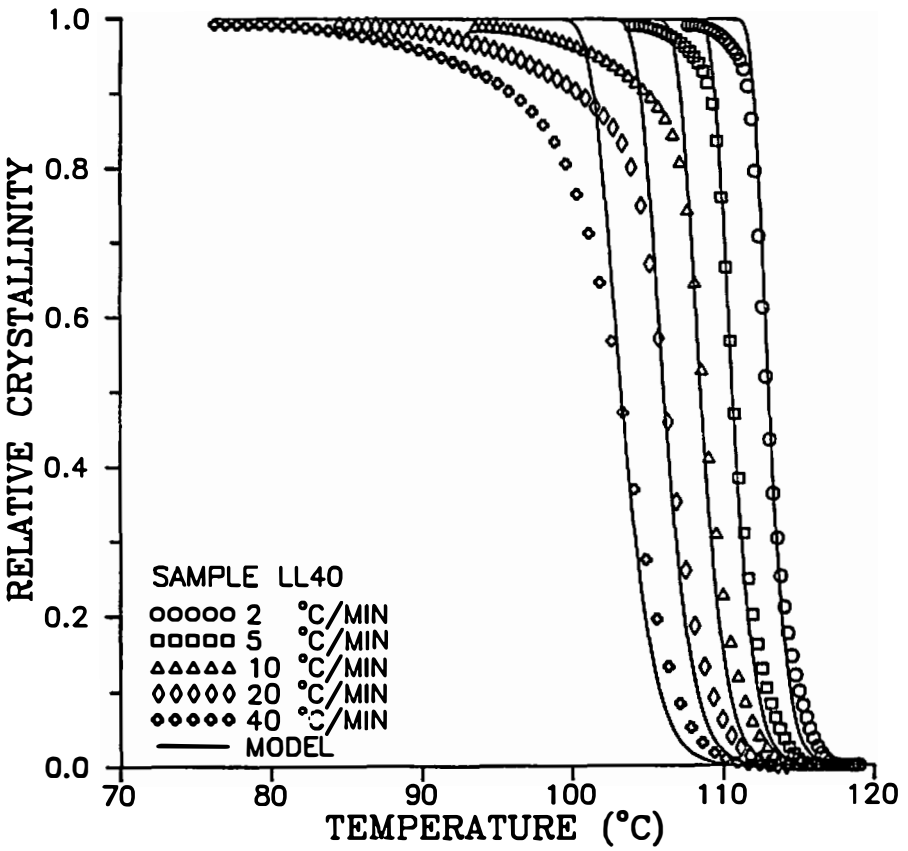

Figure A.34 LL40 non-isothermal crystallization curves and non-linear regression predictions.

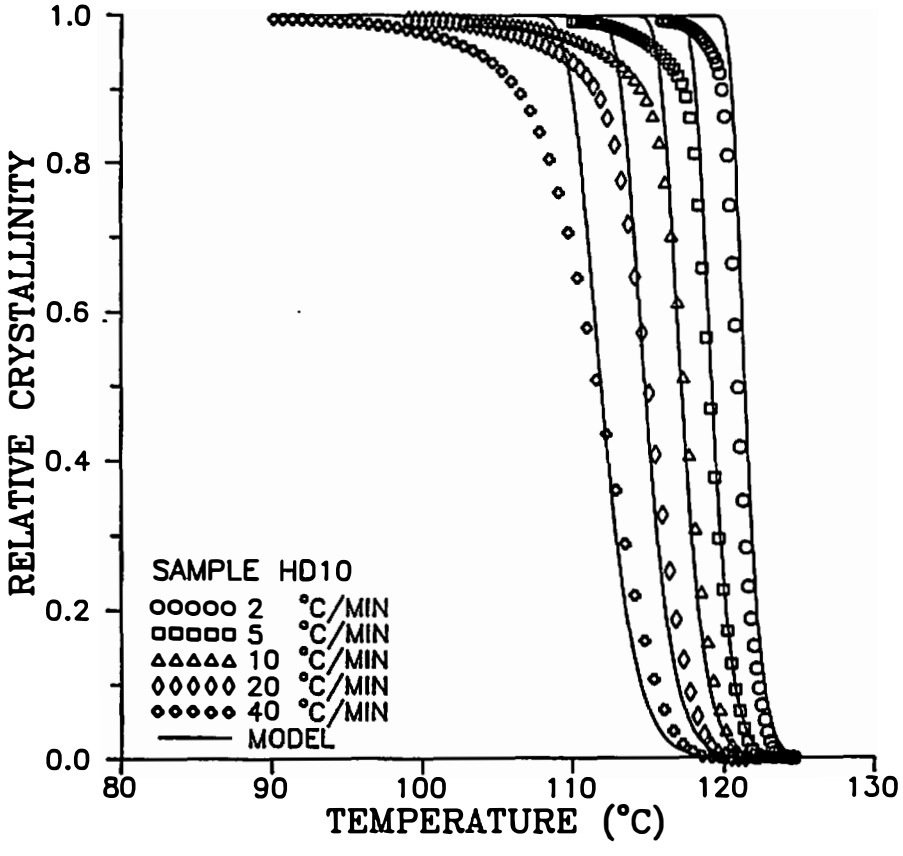

Figure A.35 HD10 non-isothermal crystallization curves and non-linear regression predictions.

APPENDIX E

EXPERIMENTAL SPINLINE DATA

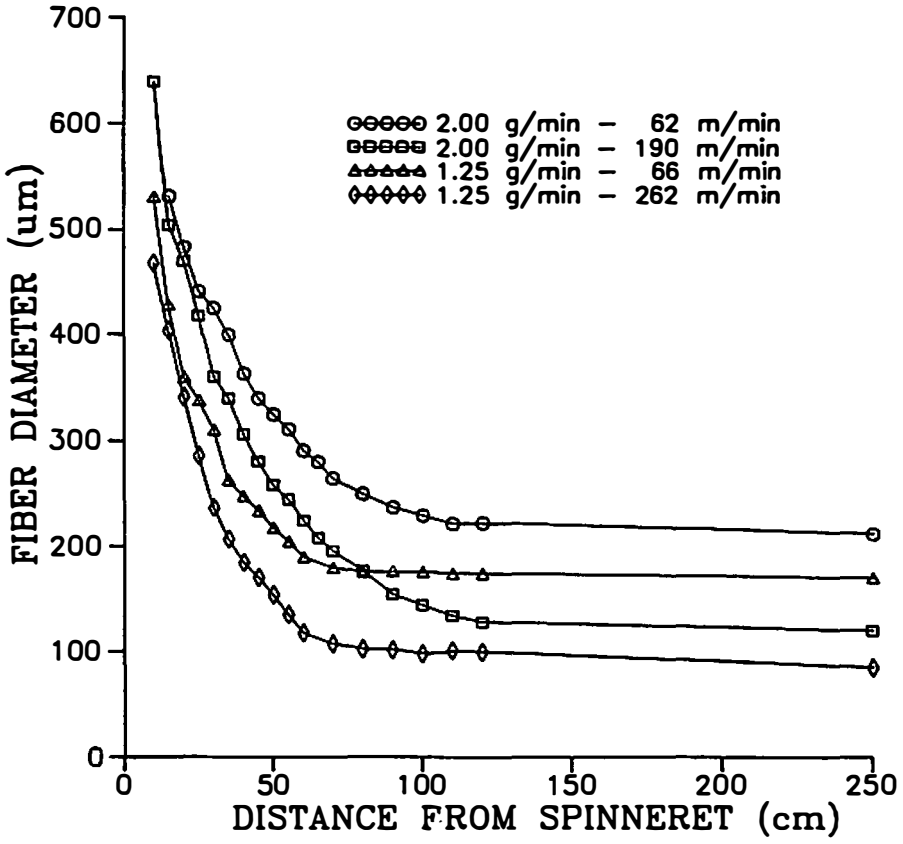

Figure A.36 LL3.9 diameter drawdown profiles.

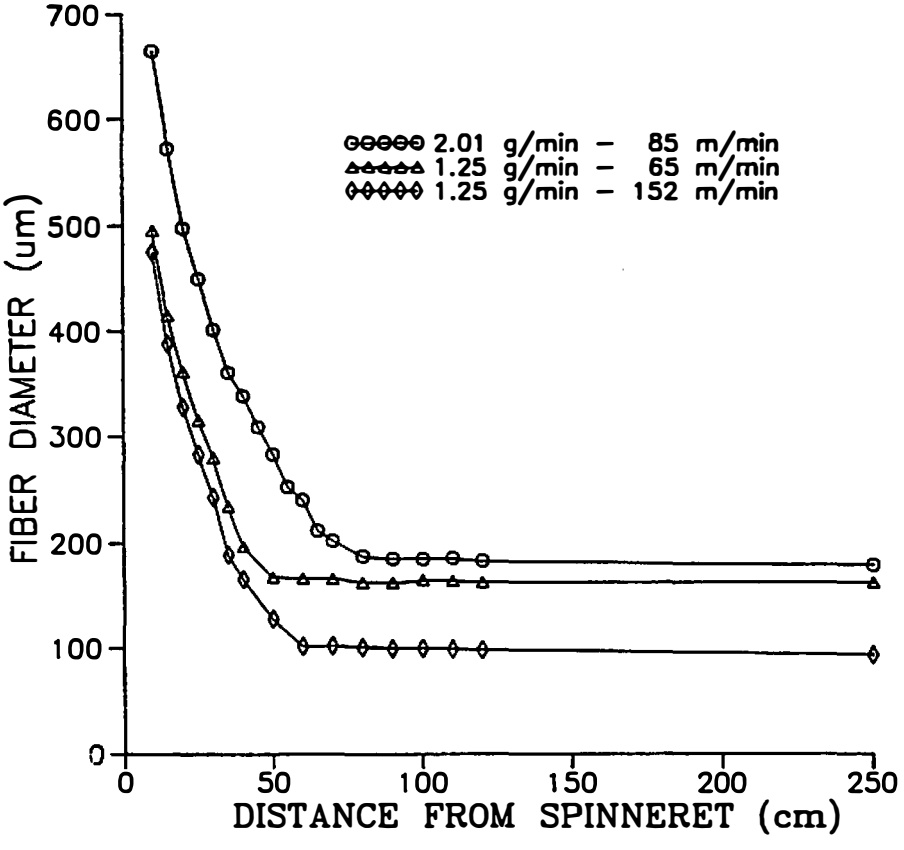

Figure A.37 LLP diameter drawdown profiles.

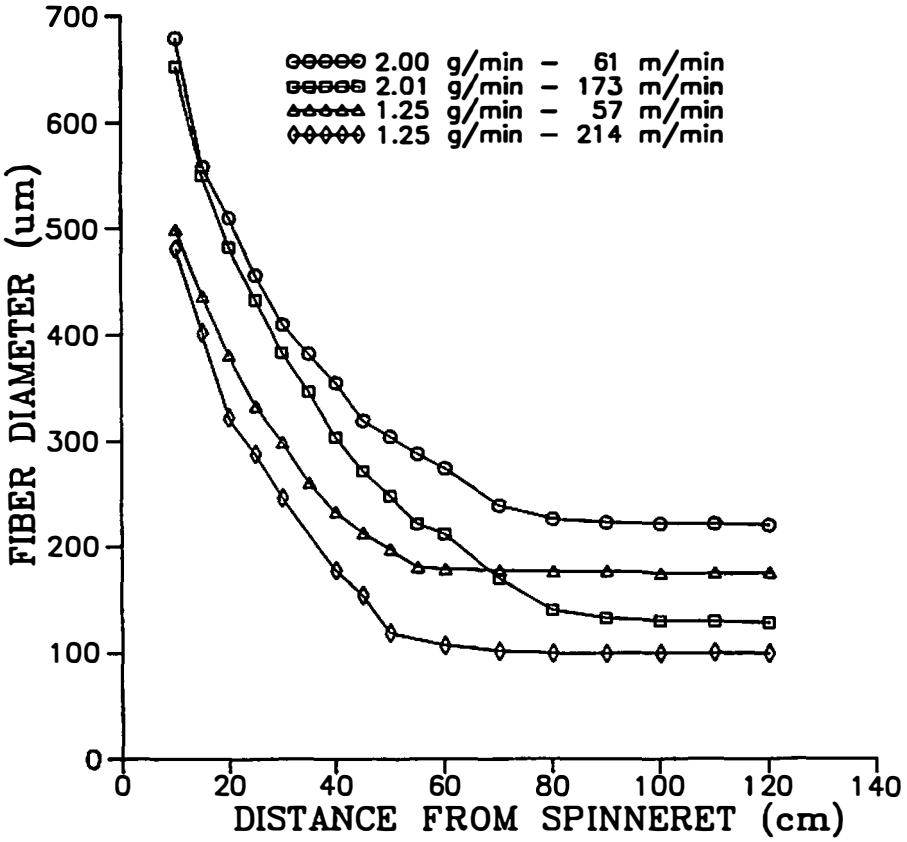

Figure A.38 LL4.3 diameter drawdown profiles.

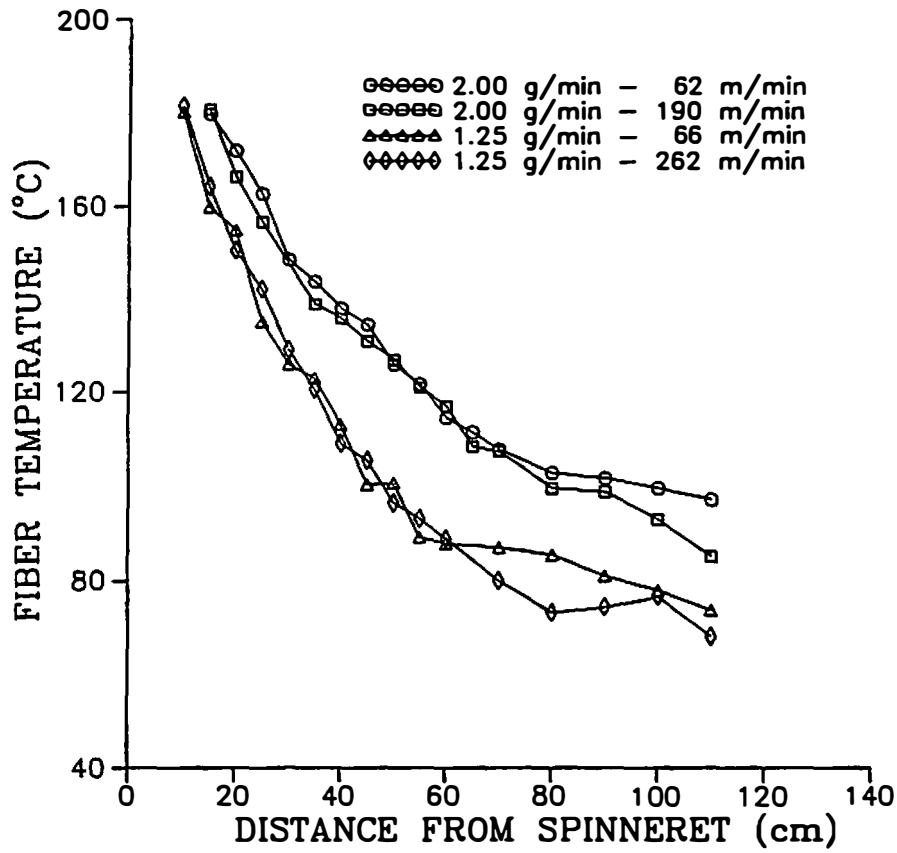

Figure A.39 LL3.9 on-line temperature profiles.

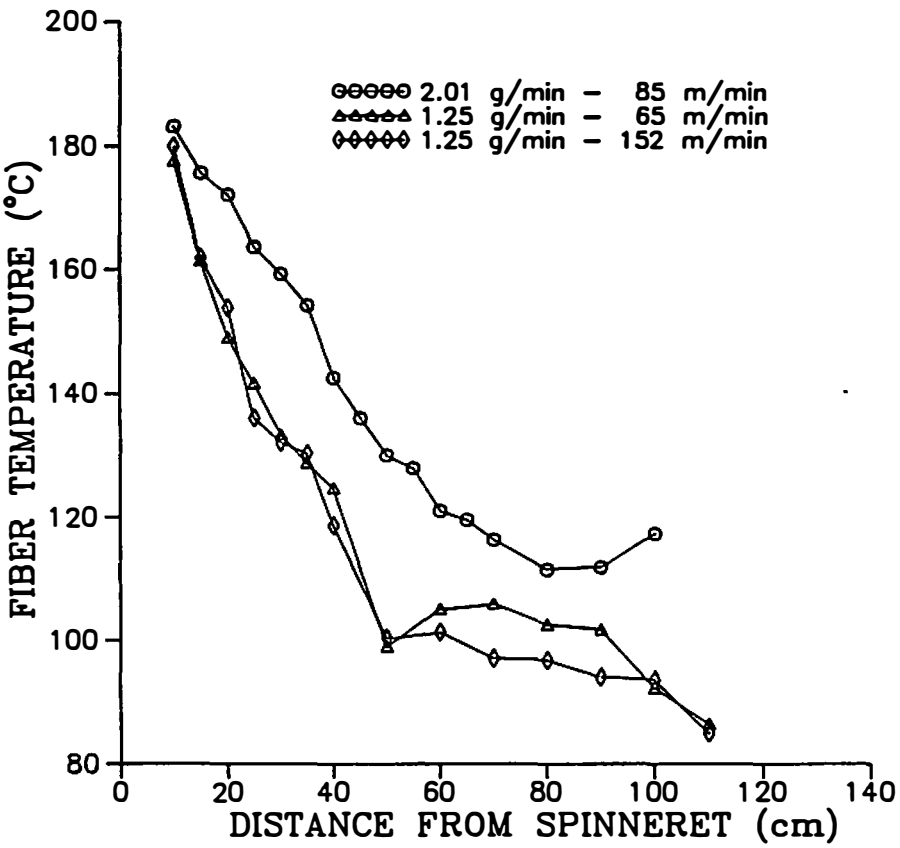

Figure A.40 LLP on-line temperature profiles.

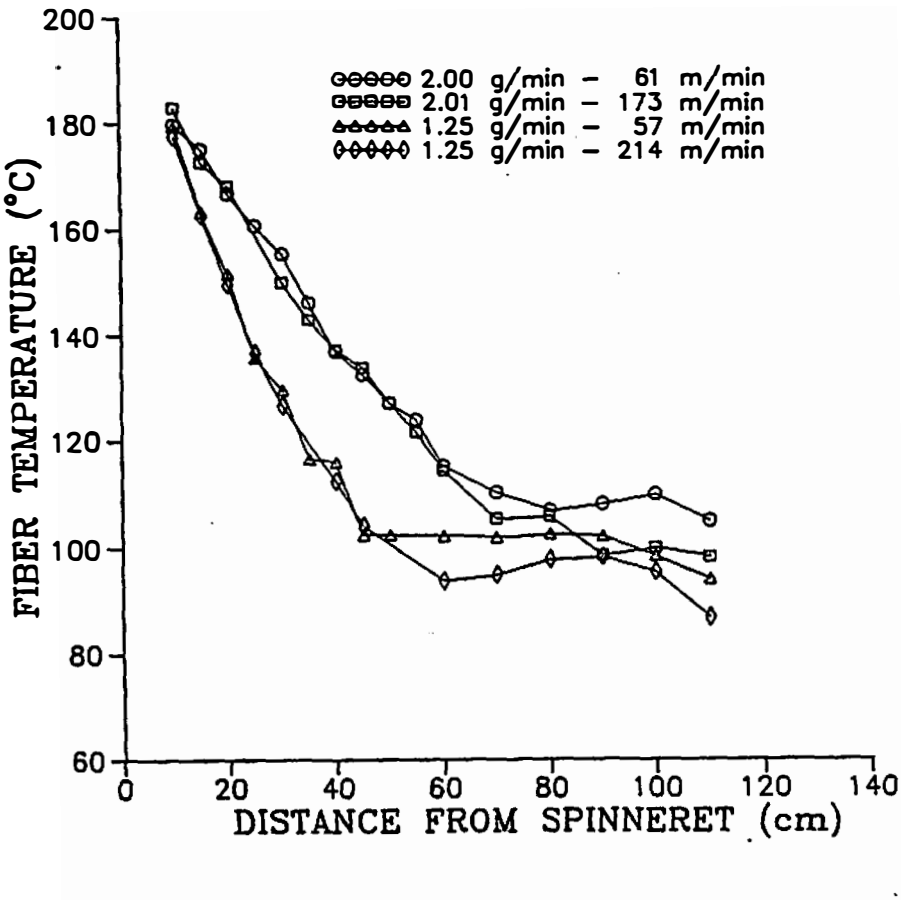

Figure A.41 LL4.3 on-line temperature profiles.

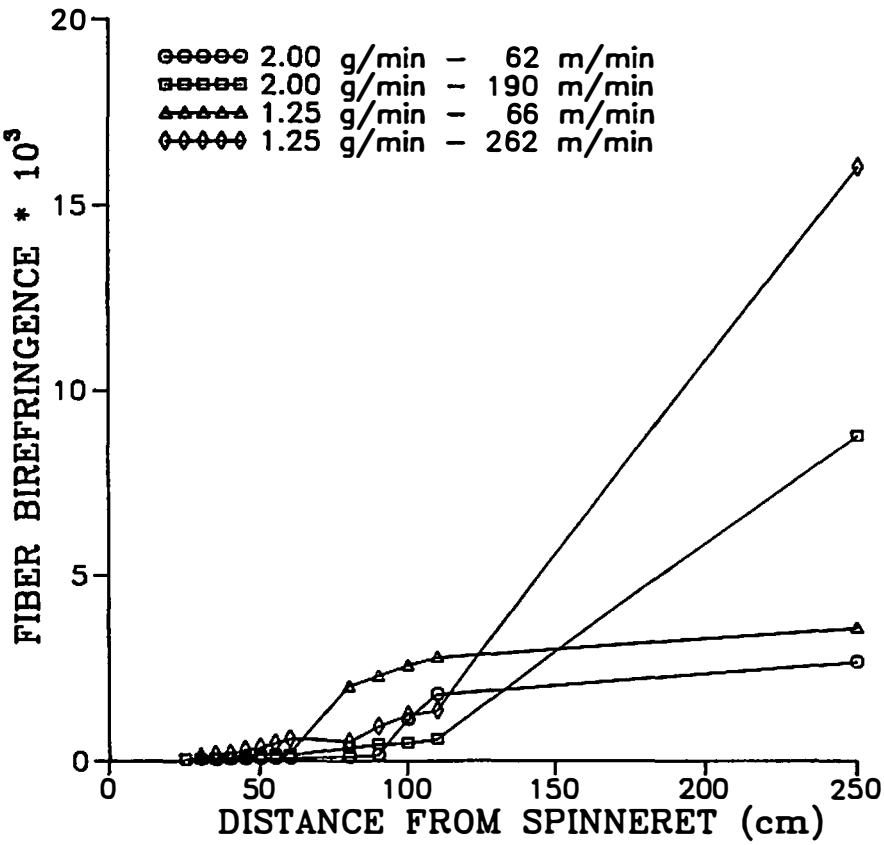

Figure A.42 LL3.9 on-line birefringence profiles.

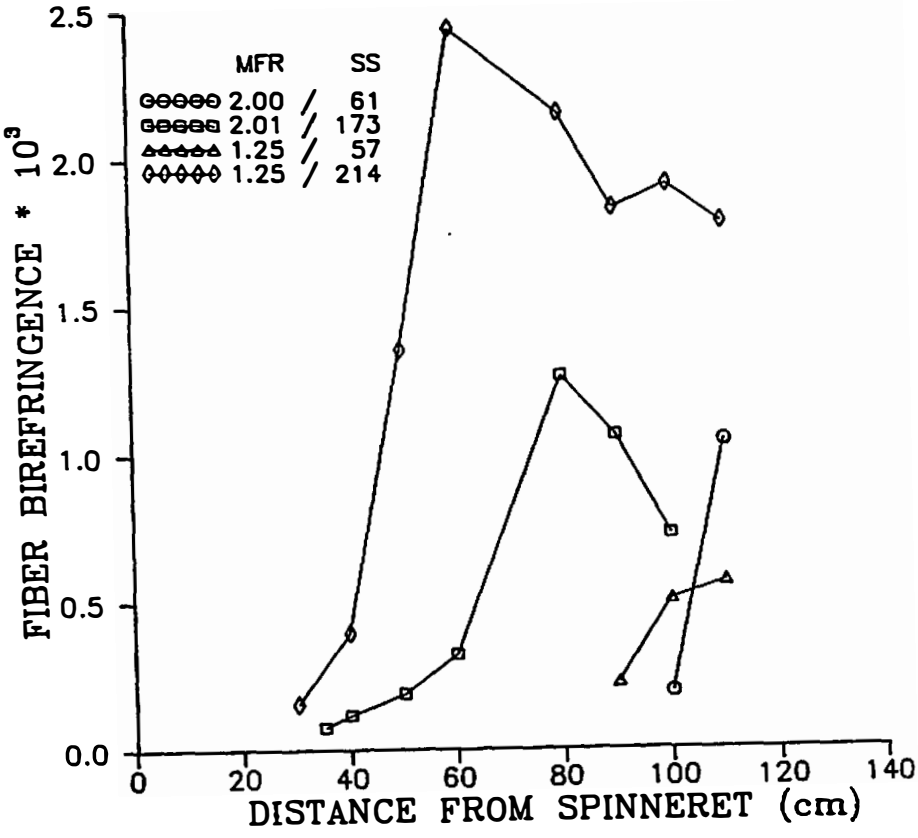

Figure A.43 LL4.3 on-line birefringence profiles.

VITA

Lawrence S. Hood was born in Knoxville, Tennessee on May 17, 1964. He entered the University of Tennessee-Knoxville in September of 1982. As an undergraduate, he participated in the Cooperative Education Program and worked at Hoechst-Celanese in Greer, South Carolina. He received a Bachelor of Science in Chemical Engineering with a Minor in Mathematics in June of 1987.

Soon afterwards, he enrolled in the Department of Material Science to study Polymer Engineering. He will receive his Master of Science in Polymer Engineering in May 1990.

Upon completion of his degree requirements, he will accept employment with Dow Chemical Company as a Research and Development Engineer at their Eastern Division Technical Center in Granville, Ohio.